PLOS BIOLOGY

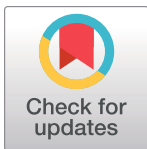# NCoR1 controls *Mycobacterium tuberculosis* growth in myeloid cells by regulating the AMPK-mTOR-TFEB axis

Viplov Kumar Biswas[1,2☯], Kaushik Sen[1,3☯], Abdul Ahad[1☯], Arup Ghosh[1,2], Surbhi Verma[4], Rashmirekha Pati[1], Subhasish Prusty[1,3], Sourya Prakash Nayak[1], Sreeparna Podder[1,2], Dhiraj Kumar[4], Bhawna Gupta[2]*, Sunil Kumar Raghav[1,2]*

1 Immuno-genomics & Systems Biology Laboratory, Institute of Life Sciences (ILS), Bhubaneswar, India, 2 School of Biotechnology, Kalinga Institute of Industrial Technology (KIIT), Bhubaneswar, India, 3 Regional Centre for Biotechnology, Faridabad, India, 4 Molecular Medicine: Cellular Immunology, International Centre for Genetic Engineering and Biotechnology (ICGEB), New Delhi, India

☯ These authors contributed equally to this work.
* bhawna.gupta@kiitbiotech.ac.in (BG); sunilraghav@ils.res.in, raghuvanshi2010@yahoo.co.in (SKR)

Abstract

Mycobacterium tuberculosis (*Mtb*) defends host-mediated killing by repressing the autophagolysosome machinery. For the first time, we report NCoR1 co-repressor as a crucial host factor, controlling *Mtb* growth in myeloid cells by regulating both autophagosome maturation and lysosome biogenesis. We found that the dynamic expression of NCoR1 is compromised in human peripheral blood mononuclear cells (PBMCs) during active *Mtb* infection, which is rescued upon prolonged anti-mycobacterial therapy. In addition, a loss of function in myeloid-specific NCoR1 considerably exacerbates the growth of *M. tuberculosis* in vitro in THP1 differentiated macrophages, ex vivo in bone marrow-derived macrophages (BMDMs), and in vivo in NCoR1[MyeKO] mice. We showed that NCoR1 depletion controls the AMPK-mTOR-TFEB signalling axis by fine-tuning cellular adenosine triphosphate (ATP) homeostasis, which in turn changes the expression of proteins involved in autophagy and lysosomal biogenesis. Moreover, we also showed that the treatment of NCoR1 depleted cells by Rapamycin, Antimycin-A, or Metformin rescued the TFEB activity and LC3 levels, resulting in enhanced *Mtb* clearance. Similarly, expressing NCoR1 exogenously rescued the AMPK-mTOR-TFEB signalling axis and *Mtb* killing. Overall, our data revealed a central role of NCoR1 in *Mtb* pathogenesis in myeloid cells.

Introduction

Macrophages and dendritic cells (DCs) are the most important cells in the myeloid lineage. They have amazing phagocytic abilities that allow them to eliminate intracellular pathogens like *Mycobacterium tuberculosis* (*Mtb*) from the host [1–3]. Among them, macrophages are central for both the host and the *Mtb* pathogen, as they provide the first line of defence and also a favourable niche for the *Mtb* survival, respectively [2,4]. These immune cells possess

different pathogen recognition receptors (PRRs) to detect pathogens, including *Mtb* and orchestrate diverse innate immune defence strategies such as phagocytosis, autophagy, and inflammasome activation [5]. However, *Mtb* hijacks host defence machinery by arresting phagosome maturation and rendering the local environment suitable for survival advantage [6,7]. The virulence of *Mtb* contributes to impairing the fusion of the auto-phagosome to the lysosome, i.e., autophagy flux, in order to evade the host antimicrobial mechanism [8,9]. However, the precise process by which *Mtb* inhibits particular stages of the autophagy pathway is not well understood. To establish a successful invasion, *Mtb* dismantles macrophage functionality, weakening the effectiveness of lysosomal trafficking for its own survival advantages [10]. Alveolar macrophages have been shown to be replication permissive for *Mtb*, which migrates to the interstitium to infect additional phagocytic myeloid cells in IL1β-dependent manner, suggesting a tug of war between *Mtb* and the host immune system [11]. It is still a crucial question to address how *Mtb* triggers cellular death to get dispersed in new phagocytic cells by augmenting inflammation. The transcription factor EB (TFEB) is a well-known master regulator that drives the expression of genes involved in autophagy [12]. Nutrient deprivation (starvation) studies demonstrated that de-phosphorylation of TFEB and its subsequent nuclear translocation are important for optimum autophagy induction and to retrieve energy levels by adenosine triphosphate (ATP) synthesis from internal metabolic sources [13,14]. Eukaryotic cells evolved to rewire intracellular metabolic cues to connect with molecular sensors, facilitating autophagy induction or inhibition for homeostasis maintenance. Among them, AMP-activated protein kinase (AMPK) is known as a key cellular energy sensor that undergoes phosphorylation to become activated in low energy states (low ATP levels) [15,16]. Activated AMPK then directly or indirectly suppresses mTOR activity, which is generally present on the lysosomal compartment to trap TFEB [16]. The mTOR inhibition through AMPK in a low cellular energy state leads to de-phosphorylation of TFEB and subsequent nuclear translocation to activate genes for optimum autophagy induction and lysosome biosynthesis, hence fuelling up cellular energy levels [17]. Moreover, pharmacological inhibition of AMPK and mTOR has been used to prove their key roles in autophagy flux [18,19]. There is strong evidence that *Mtb* suppresses the autophagy in cells through down-regulation of TFEB activity via the AMPK-mTOR pathway, indicating the hidden molecular network that facilitates cross-talk of these pathways under *Mtb* pathogenesis [20–23]. Hence, it is highly anticipated to identify the host factors (transcriptional modulators) that regulate autophagy flux during *Mtb* infection, which could be further harnessed to develop novel paradigms to control *Mtb* infection. Among such, nuclear receptor corepressor, NCoR1, is well known to act with multi-protein complex partners to exert repression of a wide variety of genes involved in various biological processes [24–26]. Recently, it has been shown that NCoR1 gets accumulated in autophagy-deficient mice leading to suppression of LXRα-dependent genes regulating the fatty acid synthesis and lipid droplet formation, suggesting the tight connection between NCoR1 and autophagy function [27]. NCoR1 has also been shown as a key transcriptional checkpoint for the maintenance of energy metabolism in cells, and depletion of NCoR1 leads to an increase in oxidative metabolism and ATP levels [28–30]. *Mtb* has been identified to target key metabolites to perturb intracellular energy levels to escape from host autophagic machinery [31]. Energy fluctuation caused by cellular stress directly impacts the autophagy machinery through AMPK pathway, suggesting a possible role of NCoR1 in controlling *Mtb* infection.

The primary objective of the present study is to determine NCoR1's contribution to *Mtb* pathogenesis. We observed that NCoR1 expression is elevated in myeloid cells early in *Mtb* infection, and its loss of function impairs the auto-phagolysosome process via the AMPK-mTOR-TFEB axis, promoting its survival. Our findings unequivocally demonstrated that NCoR1 plays a crucial protective role in regulating *Mtb* clearance from host cells.

Results

NCoR1 expression is increased upon *Mycobacterium* infection in myeloid cells

Initially, we assessed the whole blood gene expression profile of patients with culture positive tuberculosis (TB) infection against healthy controls curated from the NCBI GEO database. When we compared individuals with active tuberculosis to healthy controls, we found that the expression of the *NCOR1* transcript was significantly lower in the active TB cases (**Fig 1A**) [32,33]. The same expression profile was observed in a separate RNA-seq dataset where the gene expression profile of TB-infected patients was captured during the course of antituberculosis treatment. We observed a decreased *NCOR1* transcript expression upon active TB infection and 6 months of treatment in treated subjects as compared to controls, whereas after 12 months of anti-mycobacterial therapy, the *NCOR1* expression is restored near to control levels (**Fig 1B**) [34]. These data suggested a clinical significance of NCoR1 levels in *Mtb* infection. Then, we looked into the kinetics of *NCOR1* expression in H37Rv-infected human monocytic THP-1 differentiated macrophages (mo-MΦ) using RT-qPCR. We observed dynamic changes in the *NCOR1* transcript levels, where its expression was found to be significantly increased during early time points till 24 h and then it went down at 48 h post infection (**Fig 1C**) [35]. It has been reported that the expression of early host response genes during *Mtb* infection is a crucial event to decide the fate of the disease outcome [33,36]. *Mtb* takes over the cellular regulatory circuit at later stages to subvert host defence machinery for its survival advantage [7,37,38]. To substantiate our observations further, we infected human peripheral blood mononuclear cells (PBMCs) with H37Rv to analyse NCoR1 protein levels by immunofluorescence (**Fig 1D and 1E**). The expression of *NCOR1* in PBMCs was also confirmed at the transcript levels (**S1A Fig**). We further assessed the NCoR1 protein levels in *Mtb*-infected mo-MΦ using western blotting and found its peak expression at 12 h post infection, which goes down at later time points (**Fig 1F**). Next, we asked whether this dynamic expression of NCoR1 is limited to mo-MΦ or whether it behaves similarly in other phagocytic myeloid cell types as well, like DCs. We employed a murine-derived type 1 conventional dendritic cell line (Mutu-cDC1 line), which was characterised in detail in previous reports [39–41]. We checked the NCoR1 expression in *Mtb* and *M. smegmatis*-infected cDC1 line [40,42]. Though cDC1 showed early induction of NCoR1 at 6 h in western blot analysis post infection, the trend was similar to the results observed in macrophages (**Fig 1G**). In addition, *Ncor1* expression also showed a similar increased pattern at the transcript level as well as in *M. smegmatis*-infected cDC1 line (**S1B Fig**). Overall, these results depicted that NCoR1 expression was significantly increased during the early course of H37Rv infection, which goes down after 24 h, hinting towards an important role in host responses against *Mtb* infection.

NCoR1 depletion enhanced *Mycobacterium* burden in myeloid cells

To decipher the role of NCoR1 in *Mtb* infection, we developed a stable *NCoR1* gene knockdown (KD) THP1 mo-MΦ line using lentivirus-mediated shRNA transduction. To assess the efficiency of shRNA-mediated NCoR1 depletion, we performed kinetics of NCoR1 expression in H37Rv-infected control and NCoR1 KD mo-MΦ. We found a significant depletion of NCoR1 at transcript as well as protein levels at all time points (**Figs 2A, 2B, and S2A**). To assess the impact of NCoR1 depletion on *Mtb* load, we infected the control and NCoR1 KD mo-MΦ by pathogenic strain of *Mycobacterium tuberculosis*, i.e., H37Rv and nonpathogenic laboratory strain *M. smegmatis* to quantify the bacterial load using CFU assay at 24 h post infection. We found that NCoR1 KD mo-MΦ harbours more H37Rv or *M. smegmatis* burden
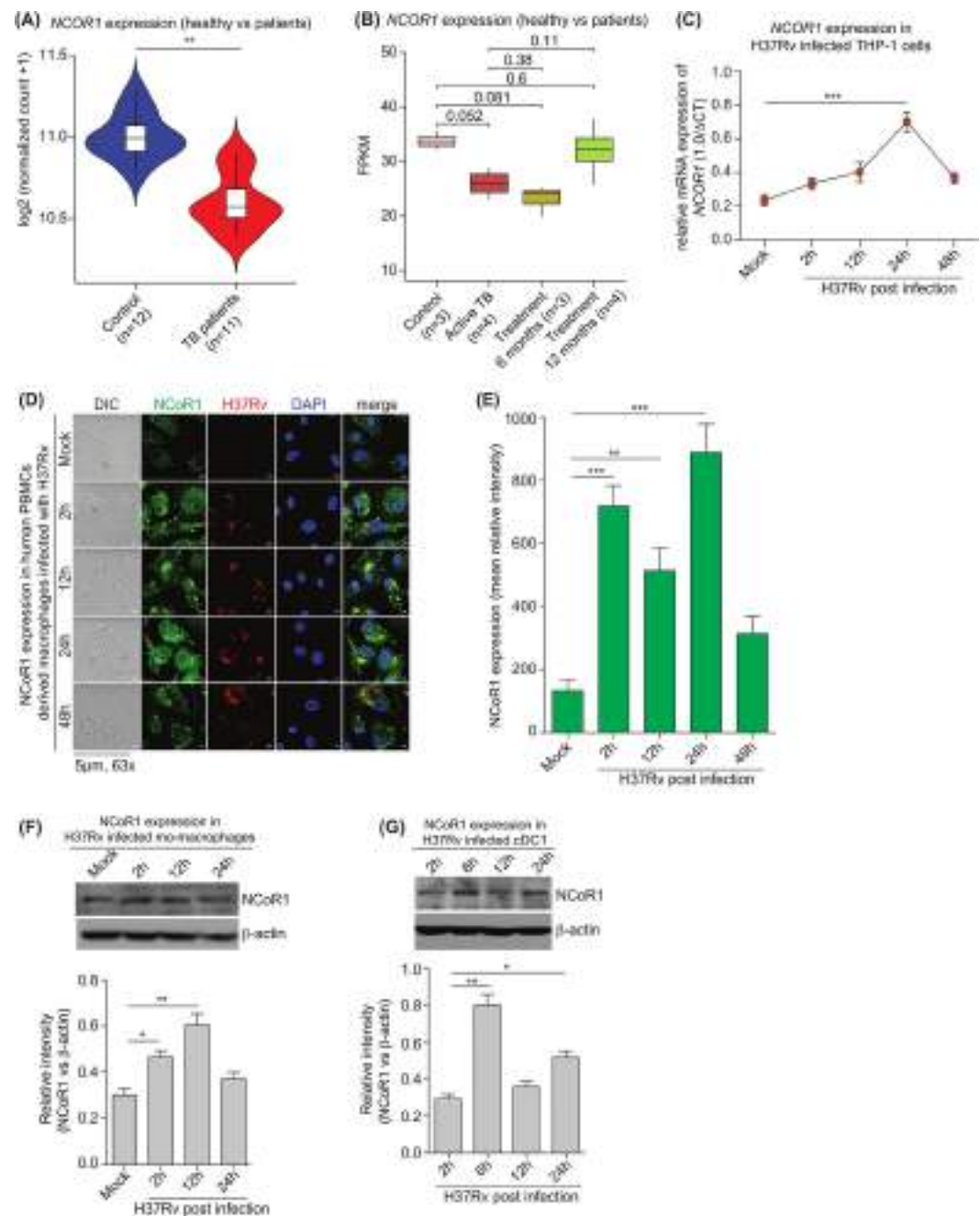
Fig 1. NCoR1 expression is increased upon *Mycobacterium* infection in myeloid cells. (A) Violin plot depicting the normalised read counts of *NCOR1* in publicly available transcriptome data of PBMCs from active TB patients and healthy control. Healthy control $n = 12$, active TB patients $n = 11$. (B) Box plot demonstrating the normalised FPKM (Fragment counts / kb / million reads) of *NCOR1* from publicly available transcriptome data of PBMCs from healthy control and active TB patients along with active patients undergoing anti-TB treatment regimen for 6 and 12 months. Healthy control $n = 3$, active patients $n = 4$, active patients with 6 months treatment $n = 3$, active patients with 12 months treatment $n = 4$. (C) RT-qPCR line graph depicting the *NCOR1* transcription kinetics (2 h, 6 h, 24 h, and 48 h) in H37Rv-infected human monocytic THP-1 differentiated macrophages ($n = 3$). (D, E) Confocal microscopy images and bar plots quantification showing the NCoR1 expression in human PBMCs-derived macrophages infected with H37RV at different time points ($n = 4$ human subjects). (F) Western blot image with densitometric analysis (bar plots) of bands depicting the NCoR1 protein expression upon H37Rv infection in human monocytic THP-1 differentiated macrophages at different time points. For normalisation, β-actin was used as housekeeping control ($n = 3$). (G) Western blot image and its densitometric analysis (bar plots) of bands demonstrating the NCoR1 protein levels in H37Rv-infected mouse cDC1 at different time points ($n = 3$). $^*p < 0.05$, $^*p < 0.01$, and $^{***}p < 0.001$ were considered significant. Data analysis was performed, (A) Wald test, (B) Wilcoxon rank

as compared to control cells (**Figs 2C and S2B**). In addition, we confirmed these results by flow cytometry using mCherry-tagged H37Rv or *M. smegmatis*, where we observed similar and significantly increased percent infection along with their respective mean fluorescence intensity (MFI) shifts for H37Rv or *M. smegmatis* in NCoR1 KD mo-MΦ (**Figs 2D, 2E, and S2C–S2F**). Further, to overcome the off-target effects, NCoR1 transcript levels were also checked with a different shRNA (**S2G Fig**). Similar results were confirmed using shRNA3-mediated NCoR1 KD mo-MΦ as well (**S2H, S2K and S2L Figs**). We also quantified phagocytosis rate kinetics to observe infection difference at early time points between control and NCoR1 KD cells using yellow-green latex beads and *M. smegmatis* infection at 10 min, 30 min, and 60 min time points using flow cytometry and CFU assay [43]. We did not observe any phagocytosis difference at any of the early time points, suggesting the role of NCoR1 in controlling *Mtb* survival independent of phagocytosis rate (**Figs 2F–2H, S2I and S2J**). Next, we asked whether similar phenomena were preserved in primary cells as well. We generated myeloid specific (macrophages and DCs) conditional NCoR1 knockout (NCoR1^MyeKO) mice by breeding homozygous NCoR1^fl/fl-CD11c-Cre C57BL/6 mice with LysM-Cre FvB mice. After more than 10 generations of crosses, the genotyped homozygous double (macrophage and DC) NCoR1 KO mice and matched control littermates were used for experiments (**S2M Fig**) [40]. To exclude bias and confirm deletion of NCoR1 in myeloid cells with respect to other cell types, we sorted CD11c^+ and CD11c^- populations and found *Ncor1* transcript levels to be ablated in the CD11c^+ fraction (**S2N Fig**) [40,44]. We analysed the expression of NCoR1 in BMDMs from NCoR1^MyeKO mice, where we found significant depletion of NCoR1 at both the protein and transcript levels (**Fig 2I–2K**). Next, we investigated the levels of *Mtb* infection in BMDMs and peritoneal macrophages and found similar increased susceptibility in our CFU assays for NCoR1 KO mice (**Fig 2L and 2M**). To further substantiate our observations in DCs, we infected previously characterised stable control and NCoR1 KD cDC1 line [40]. NCoR1 depletion at the protein level was confirmed upon H37Rv infection (**Fig 2N and 2O**). These cells also depicted similar increased susceptibility to H37Rv and *M. smegmatis* infection in CFU assays (**Figs 2P, S2O and S2P**). The MFI also depicted a significantly increased shift for H37Rv infection in NCoR1 KD cDC1 as compared to controls (**Fig 2Q and 2R**). Overall, our results clearly demonstrated that NCoR1 depletion plays an essential role in myeloid cells (macrophages as well as DCs) to augment *Mtb* infection.

NCoR1^MyeKO mice depicted enhanced *Mycobacterium* infection in vivo

To establish the physiological impact of NCoR1 in *Mtb* pathogenicity and virulence in vivo, we infected control NCoR1^fl/fl and NCoR1^MyeKO mice with 10^5 H37Rv (GFP-tagged) (**S3A Fig**) [45]. The body weights of infected mice were measured at regular intervals, and we found that NCoR1^MyeKO animals started to show a significant reduction in body weight from day 7 post infection as compared to floxed control mice, which was further reduced (day 17 to day 21) in subsequent days (**Fig 3A**). In addition, we observed profoundly enhanced splenomegaly in NCoR1^MyeKO animals at day 21 post infection (**S3B Fig**). Next, we estimated the bacterial load in the lungs and spleen of infected mice. NCoR1^MyeKO mice showed increased bacterial load at day 7 which was further increased at day 21 post infection (**Fig 3B and 3C**). We also examined the myeloid cell frequencies in lung and spleen using specific markers and gating strategies (**S3C and S3E Fig**) [46]. We found increased frequencies and cell numbers of neutrophils,
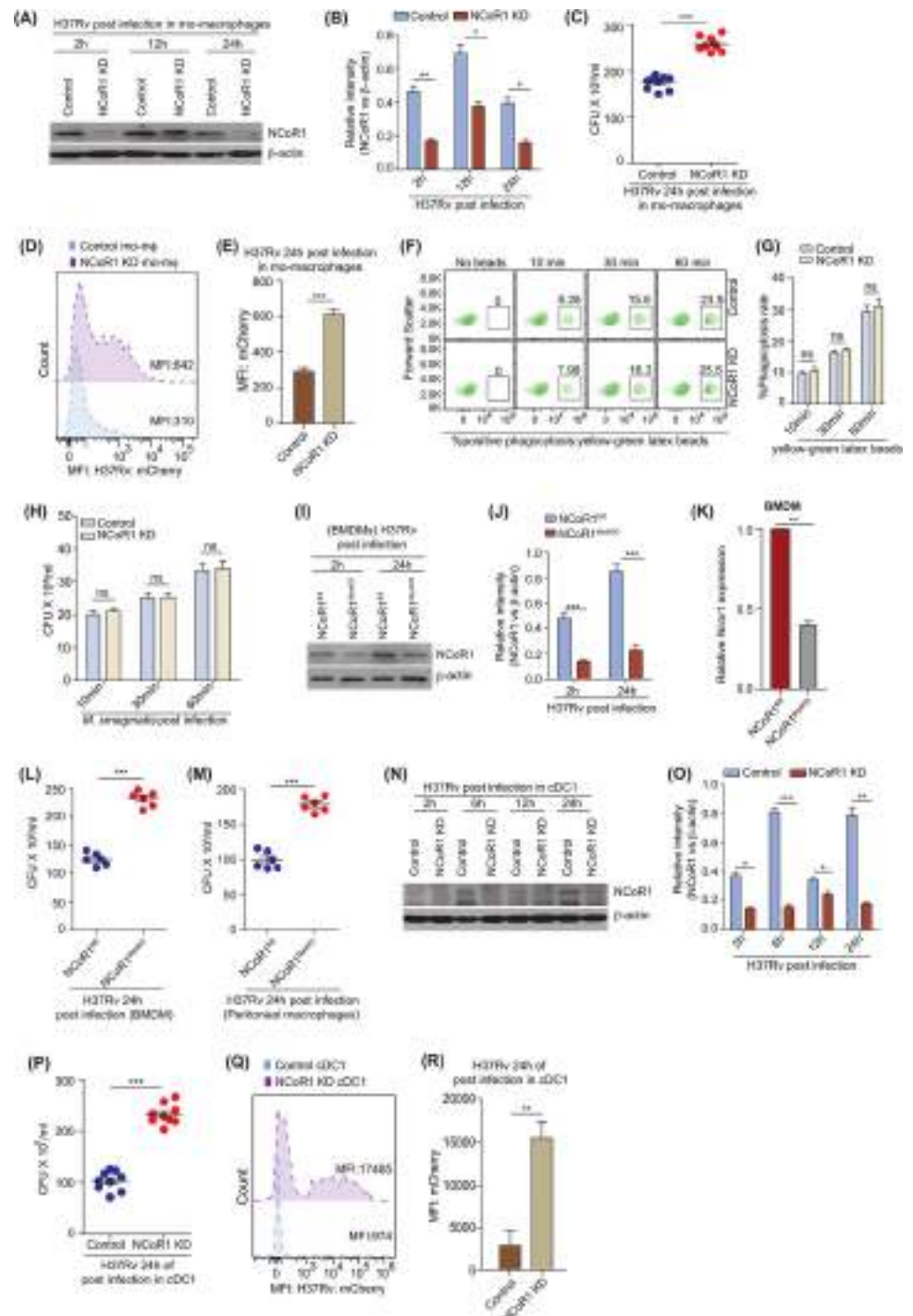
Fig 2. NCoR1 depletion enhanced *Mycobacterium* burden in myeloid cells. (A) Western blot image showing the NCoR1 protein levels at 2 h, 12 h, and 24 h in H37Rv-infected control and NCoR1 depleted human monocytic THP-1 differentiated macrophages. For normalisation, β-actin was used as housekeeping control (*n* = 3). (B) Bar plot demonstrating the quantification of NCoR1 protein levels at 2 h, 12 h, and 24 h of H37Rv-infected control and NCoR1 KD human monocytic THP-1 differentiated macrophages. Densitometric analysis is performed using 3 independent biological replicates (*n* = 3). (C) Scatter plot showing the bacterial load in H37Rv-infected control and NCoR1 KD human monocytic THP-1 differentiated macrophages by CFU assay 24 h post infection (*n* = 9). (D) Representative flow cytometry histogram plots showing the MFI shift of H37Rv-mCherry–infected control and NCoR1 KD human monocytic THP-1 differentiated macrophages at 24 h post infection (*n* = 3). (E) Bar plot demonstrating the quantification of MFI shifts from 3 biological replicates of H37Rv-mCherry–infected control and NCoR1 KD human

monocytic THP-1 differentiated macrophages at 24 h post infection (*n* = 3). (F, G) Flow cytometry contour plot and bar plot showing the phagocytosis rate of yellow-green latex beads in control and NCoR1 KD human monocytic THP-1 differentiated macrophages at 10 min, 30 min, and 60 min post latex bead incubation (*n* = 3). (H) Bar plot showing the quantification of phagocytosis rate estimated by CFU assay of *M. smegmatis* in control and NCoR1 KD human monocytic THP-1 differentiated macrophages at 10 min, 30 min, and 60 min post infection (*n* = 3). (I, J) Western blot image with densitometric analysis of bands depicting the NCoR1 protein levels at 2 h and 24 h of H37Rv-infected BMDMs generated from NCoR1$^{fl/fl}$ and NCoR1^{MyeKO} mice. For normalisation, β-actin was used as housekeeping control. Three independent biological replicates were used to estimate the protein levels (*n* = 4 mice). (K) Bar plot demonstrating the NCoR1 transcript levels in BMDMs generated from NCoR1$^{fl/fl}$ and NCoR1^{MyeKO} mice post 24 h of H37Rv infection. Three independent biological replicates were used to estimate the transcript levels (*n* = 4 mice). (L) Scatter plot showing the bacterial load in H37Rv-mCherry–infected BMDMs generated from NCoR1$^{fl/fl}$ and NCoR1^{MyeKO} mice (*n* = 6 mice). (M) Scatter plot depicting the bacterial load in H37Rv-mCherry–infected peritoneal macrophages from NCoR1$^{fl/fl}$ and NCoR1^{MyeKO} mice (*n* = 6 mice). (N, O) Western blot image showing the NCoR1 protein level kinetics with quantification (bar plot) in control and NCoR1 KD cDC1 (conventional type I dendritic cells) upon H37Rv infection. For normalisation, β-actin was used as housekeeping control (*n* = 3). (P) Scatter plot showing the H37Rv bacterial load in control and NCoR1 KD cDC1 at 24 h time point as estimated by CFU assay (*n* = 9). (Q) Histogram from FACS analysis showing the MFI shifts of H37Rv-mCherry–infected control and NCoR1 KD cDC1 at 24 h post infection (*n* = 3). (R) Bar plot demonstrating the quantification of MFI shifts from 3 independent biological replicates of H37Rv-mCherry–infected control and NCoR1 KD cDC1 at 24 h post infection (*n* = 3). *p < 0.05, *p < 0.01, and ***p < 0.001 using paired and unpaired two-tailed Student's *t* test. Where n represents independent biological replicates. The data underlying this figure are available in S4 Table and S1 Data. Western blot raw images can be found in S1 Raw Image. BMDM, bone marrow-derived macrophage; KD, knockdown; MFI, mean fluorescence intensity.

https://doi.org/10.1371/journal.pbio.3002231.g002

dendritic cells, and eosinophils with decreased levels of alveolar and infiltrating macrophages at day 21 post infection per lung of NCoR1^{MyeKO} as compared to control (**Figs 3D and S3D**). Whereas, in spleen, we did not observe a significant difference in DCs but a significantly increased frequency of macrophages, monocytes, and neutrophils were observed in NCoR1-^{MyeKO} (**Fig 3E**). The cell numbers of the above myeloid cell types also showed similar trends in the spleen (**S3F Fig**). Next, we evaluated the *Mtb* infection in the lung myeloid cells, where we observed elevated *Mtb* infection in neutrophils, alveolar macrophages, dendritic cells, eosinophils, infiltrating macrophages, and inflammatory monocytes in the lung of NCoR1^{MyeKO} as compared to NCoR1$^{fl/fl}$ mice (**Figs 3F, 3G, and S3D**). Further, similar increased frequency and cell numbers of *Mtb*-infected dendritic cells, macrophages, monocytes, and neutrophils were obtained in the spleen of NCoR1^{MyeKO} mice (**Figs 3H, 3I, and S3F**). In addition, we also evaluated the lymphocyte compartments, where we did not observe any difference in the frequencies and cell numbers of B and T cell subtypes (**Figs 3J, S3G, and S3H**). Further, we asked whether NCoR1^{MyeKO} mice have increased inflammation culminating into higher susceptibility for *Mtb* infection. For which we performed a bio-plex assay to quantify various cytokines in the lung lysates and found NCoR1^{MyeKO} mice to have significantly high levels of inflammatory cytokines like IL-1α, IL-1β, IL-6, and IL-17A (**Fig 3K**). In addition, we examined the infiltration of cells in the lung tissue using haematoxylin and eosin (HE) staining. We found increased infiltration of cells in the *Mtb*-infected lung section of NCoR1^{MyeKO} mice as compared to control (**Fig 3L**) [47]. These results were consistent with other previous reports showing that disrupted autophagy can elevate inflammatory mediators [48,49]. These results demonstrated that NCoR1 is a crucial host factor in controlling TB disease, and its ablation exacerbates *Mtb* pathogenesis.

NCoR1 regulates autophagy induction during *Mtb* infection

Next, we intended to look into the mechanism of dysregulated host responses upon NCoR1 depletion leading to increased *Mycobacterium* pathogenesis. To gain a global insight into the mechanistic aspect, we performed RNA-seq analysis of *Mtb*-infected control and NCoR1 KD mo-MΦ at 2 h and 24 h post infection (**S1 Table**). We found a set of genes involved in the
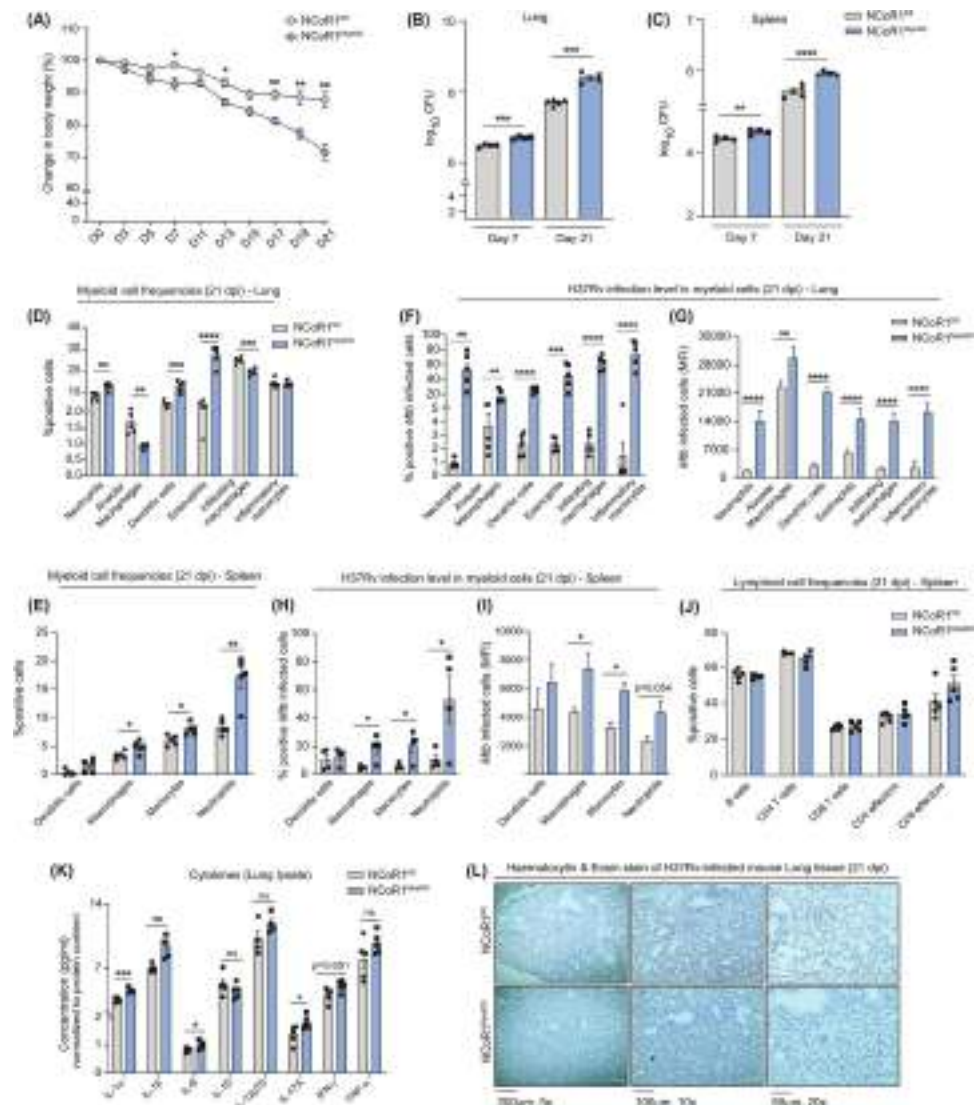
Fig 3. Myeloid specific NCoR1 deletion exacerbates *Mycobacterium* infection in mice. (A) Line graph showing the percent reduction in body weight upon H37Rv infection in NCoR1^fl/fl and NCoR1^MyeKO mice at regular intervals till day 21 post infection ($n = 5$ mice). (B, C) Bar plots showing the bacterial load in the lung tissues of H37Rv-infected NCoR1^fl/fl and NCoR1^MyeKO mice at day 7 and day 21 post infection by CFU assay in lung and spleen. Data is presented as the median $\log_{10}$CFU ($n = 4–5$). (D) Bar plots showing the percent positive myeloid cell subtypes gated on CD45 positive cells isolated from lung tissues of NCoR1^fl/fl and NCoR1^MyeKO mice on day 21 post infection. Strategy used to gate H37Rv-infected macrophages in FACS is shown in S3C Fig ($n = 5$). (E) Bar plots showing the percent positive myeloid cell subtypes gated on CD45 positive cells isolated from spleen tissues of NCoR1^fl/fl and NCoR1^MyeKO mice on day 21 post infection. Strategy used to gate H37Rv-infected macrophages in FACS is shown in S3D Fig ($n = 5$). (F) Bar plots showing the percentage of GFP-tagged H37Rv infection in neutrophils, alveolar macrophages, dendritic cells, eosinophils, infiltrating macrophages, and inflammatory monocytes, and (G) corresponding MFI shifts in the cells isolated from lung tissues of NCoR1^fl/fl and NCoR1^MyeKO mice on day 21 post infection ($n = 5$). (H) Bar plot showing the percentage of GFP-tagged H37Rv infection in dendritic cells, macrophages, monocytes, and neutrophils, and (I) corresponding MFI shifts in the cells isolated from spleen tissues of NCoR1^fl/fl and NCoR1^MyeKO mice on day 21 post infection ($n = 4$). (J) Bar plot showing the percent positive B cell and T cell subtypes gated on CD45 positive cells isolated from splenic tissues of NCoR1^fl/fl and NCoR1^MyeKO mice on day 21 post infection. Strategy used to gate H37Rv-infected macrophages in FACS is shown in S3E Fig ($n = 5$). (K) Bar plot showing the level of different inflammatory cytokines in the lung tissue lysate of NCoR1^fl/fl and NCoR1^MyeKO mice on day 21, normalised to protein content ($n = 5$). (L) Representative HE staining image showing infiltration of cells in the lung tissue of NCoR1^fl/fl and NCoR1^MyeKO mice on day 21. *$p < 0.05$, *$p < 0.01$, and ***$p < 0.001$ using an unpaired, two-tailed Student's *t* test. Where n represents the total number of used mice. The data underlying this figure are available in S1 Data. HE, haematoxylin and eosin; MFI, mean fluorescence intensity.

https://doi.org/10.1371/journal.pbio.3002231.g003

autophagy process that were significantly down, namely, ATG3, ATG5, and ATG13. Hypoxic molecule HIF-1α (stabilisation has antimicrobial activity) was also found to be decreased in the NCoR1 KD condition at 24 h post infection (**Fig 4A and 4B** **and S2 Table**). In addition, inflammatory mediators like TNFα and NFκB also showed diminished expression (**Fig 4A**). It has already been documented that autophagy plays a central role in host defence mechanisms to clear the intracellular pathogens including *Mtb* by augmenting intracellular cargos to destroy in phagolysosomes [50,51]. Moreover, NCoR1 showed a strong association with the autophagy pathway in string network analysis as well (**Fig 4C**). Mo-MΦ-mediated autophagy induces LC3 lipidation (LC3II) at an early time point upon H37Rv infection, which is an important event to control bacterial infection through an optimal level of autophagy flux [52]. Next, to confirm the same, we treated H37Rv-infected control and NCoR1 KD mo-MΦ with and without bafilomycin. We found that the LC3-II: LC3-I ratio was significantly reduced in NCoR1 KD mo-MΦ as compared to control cells confirming the observation from RNA-seq data (**Fig 4D and 4E**). We also found that LC3-II:LC3-I ratio was significantly elevated in the bafilomycin treated control mo-MΦ cells as compared to untreated cells, suggesting that autophagy flux is intact (**Fig 4D and 4E**). On the other hand, in the NCoR1 KD mo-MΦ, the LC3-II:LC3-I was reduced in untreated NCoR1 KD mo-MΦ compared to control cells, which showed slight but insignificant increase upon bafilomycin treatment (**Fig 4D and 4E**). In addition, bafilomycin treatment aggravated the NCoR1 mediated support of intracellular *Mtb* growth in our CFU and flow cytometry analysis, suggesting a role of NCoR1 in autophagy induction process (**Figs 4F and S4A–S4C**). This suggested that the overall autophagy process is abrogated in NCoR1 depleted cells. To substantiate these observations, we analysed the ATG12-ATG5 conjugate and Beclin1 proteins that are shown to be crucial for auto-phago-some formation and nucleation in active autophagy in various reports [53,54]. We found that NCoR1 KD mo-MΦ showed significantly decreased Beclin1 and ATG12-ATG5 protein levels upon H37Rv infection (**Fig 4G and 4H**). Moreover, we found similar decreased levels of autophagy proteins in BMDMs generated from NCoR1^MyeKO mice and in cDC1 (**Figs 4I, 4J, S4D and S4E**). We also asked whether NCoR1 KD mo-MΦ cells have reduced autophagy already at basal levels or is it H37Rv specific. We compared LC3 expression in H37Rv post-infected cells at 2 h to that in uninfected control, where we observed reduced LC3-II:LC3-I ratios only after infection (**S4F Fig**) [52]. Next, we wanted to investigate the entrapment of H37Rv with LC3. We observed a strong colocalization of LC3 with H37Rv in control mo-MΦ cells, whereas in NCoR1 KD mo-MΦ and BMDMs from NCoR1^MyeKO mice showed diminished colocalization of these proteins with a concomitant increase in bacterial load (**Figs 4K, 4L, S4G and S4H**). These findings suggested the dependency of myeloid cells on NCoR1 for the induction of an optimum autophagy flux upon *Mtb* infection. However, we cannot ignore the fact that disrupted lysosome mediated *Mtb* survival could also contribute in addition to inhibited autophagy in NCoR1 depleted myeloid cells as both pathways are known to be regulated by TFEB.

NCoR1 regulates mTOR-TFEB axis to control autophagy induction and lysosomal biogenesis in myeloid cells

The TFEB is a known master regulator of autophagy induction and maturation controlling genes [12,55]. We argued whether disrupted autophagy machinery in NCoR1 depleted myeloid cells is TFEB dependent or independent. Thus, we sought the expression kinetics of TFEB protein in H37Rv-infected wild-type mo-MΦ and cDC1, where we observed similar expression kinetics of TFEB as NCoR1, suggesting a possible association of NCoR1 and TFEB (**Figs 5A, S5A and S5B**). Moreover, we observed an increased expression of NCoR1 and TFEB in

Fig 4. NCoR1 regulates autophagy induction during *Mtb* infection. (A) Heat map showing the top differential expressed genes related to autophagy function in the RNA-seq data of control and NCoR1 KD human monocytic THP-1 differentiated macrophages at 2 h and 24 h post infection (*n* = 3). (B) Violin plot depicting the normalised transcript expression of ATGs in control and NCoR1 KD human monocytic THP-1 differentiated macrophages at 2 h and 24 h post infection (*n* = 3). (C) String network analysis showing the association of NCoR1 with top DEGs found in NCoR1 KD human monocytic THP-1 differentiated macrophages vs. control cells at 2 h and 24 h post infection (*n* = 3). (D, E) Representative western blot image depicting the LC3-II:LC3-I level in H37Rv-infected control and NCoR1 KD human monocytic THP-1 differentiated macrophages at 2 h and 24 h post infection, before and after treatment with bafilomycin. Corresponding densitometric analysis (bar plots) depicting the quantitation and statistics from the western blot images of 3 independent biological replicates. For normalisation, β-actin was used as

housekeeping control. LC3-II density versus LC3-I was quantified followed by normalisation with β-actin (*n* = 3). (F) Scatter plot showing the H37Rv bacterial load in control and NCoR1 KD human monocytic THP-1 differentiated macrophages by CFU assay at 24 h post infection, before and after treatment with bafilomycin (*n* = 4). (G, H) Western blot representative image depicting the protein levels of Beclin1 and ATG12-5 in H37Rv-infected control and NCoR1 KD human monocytic THP-1 differentiated macrophages at 2 h and 24 h post infection. Corresponding densitometric analysis (bar plots) showing the quantitation and statistics from the western blot images of 3 independent biological replicates. For normalisation, β-actin was used as housekeeping control (*n* = 3). (I) Western blot representative picture showing the levels of NCoR1, Atg12-Atg5, Beclin1, and LC3-II:LC3-I in H37Rv-infected BMDMs generated from NCoR1^{fl/fl} and NCoR1^{MyeKO} mice at 2 h and 24 h post infection. For normalisation, β-actin was used as housekeeping control. LC3-II density versus LC3-I was quantified followed by normalisation with β-actin (*n* = 4 mice). (J) Bar plot showing the densitometric quantification from western blot images for NCoR1, ATG12-ATG5, BECLIN1, and LC3 in H37Rv-infected BMDMs generated from NCoR1^{MyeKO} and NCoR1^{fl/fl} mice at 2 h and 24 h post infection. For normalisation, β-actin was used as housekeeping control (*n* = 4 mice). (K) Confocal microscopy showing the colocalization of H37Rv with LC3 protein in control and NCoR1 KD human monocytic THP-1 differentiated macrophages at 2 h and 24 h post infection (*n* = 3). (L) Bar plot depicting the quantification of confocal images from 3 independent biological replicates for the colocalization of H37Rv with LC3 in control and NCoR1 KD human monocytic THP-1 differentiated macrophages. Ten cells from each biological replicate were analysed for calculating the colocalization percentage (*n* = 3). *$p < 0.05$, *$p < 0.01$, and ***$p < 0.001$ using paired and unpaired two-tailed Student's *t* test. Where n represents independent biological replicates. The data underlying this figure are available in S1 Table and S1 Data. Western blot raw images can be found in S1 Raw Image. BMDM, bone marrow-derived macrophage; DEG, differentially expressed gene; KD, knockdown.

https://doi.org/10.1371/journal.pbio.3002231.g004

CD11c$^+$ and F4/80$^+$ cells of *Mtb*-infected lung tissue of mice (**S5C and S5D Fig**). Next, we investigated the levels of TFEB protein in H37Rv-infected control and NCoR1 depleted mo-MΦ and cDC1. We found that TFEB expression was reduced at an early point of infection in NCoR1-deficient conditions, indicating a crucial role of NCoR1 in TFEB functionality (**Figs 5B, 5C, S5E, and S5F**). We also observed similar reduced levels of TFEB with increased infection in NCoR1^{MyeKO} BMDMs as compared to control (**Figs 5D, S5G and S5H**). It is well reported that TFEB directly controls the expression of genes involved in autophagy and lysosomal pathways [20,56,57]. We also found reduced LAMP1 expression and its colocalization with *Mtb* in NCoR1^{MyeKO} BMDMs as compared to control NCoR1$^{fl/fl}$ BMDMs (**Figs 5D, S5I and S5J**). To ascertain the role of TFEB in compromised autophagy and lysosomal biogenesis, we overexpressed the flag-tagged TFEB in NCoR1 KD mo-MΦ followed by H37Rv infection for 24 h. We analysed the expression of LC3-II protein and LAMP1 in TFEB overexpressed NCoR1 KD mo-MΦ. We found restored levels of LC3-II and LAMP1, indicating the dependency of NCoR1 on TFEB in regulating autophagy and lysosomal biogenesis upon *Mtb* infection (**Fig 5E**). In addition, overexpression of TFEB in NCoR1 KD mo-MΦ significantly rescued the bacterial clearance (**Fig 5F**). Next, we asked whether host cells regulate the NCoR1-mediated autophagy process regardless of active *Mtb* infection or any other stress. Control and NCoR1 KD mo-MΦ were starved and infected with heat-killed H37Rv, they showed similar increased levels of NCoR1 along with TFEB and LC3-II:LC3-I in control mo-MΦ, whereas their expression was significantly reduced in starvation and heat-killed *Mtb* treated NCoR1 KD mo-MΦ indicating a possible role of NCoR1 in the autophagy induction process (**S5K–S5N Fig**). Induction of NCoR1 was weaker in starved conditions as compared to *Mtb* infection in mo-MΦ. Next, we investigated the mechanisms underlying the regulation of TFEB through NCoR1. It has been shown in various reports that mTOR regulates the TFEB activity by phosphorylation [21,58,59]. Our RNA-seq data depicted similar up-regulation of mTOR pathway genes in NCoR1 KD mo-MΦ at 24 h post *Mtb* infection (**Fig 5G and S1 and S2 Tables**). To confirm our observation, we analysed the activated mTOR, i.e., phospho-mTOR upon H37Rv infection. We found significantly increased phosphorylation of mTOR in H37Rv-infected NCoR1 KD mo-MΦ as compared to control cells (**Fig 5H and 5I**). At the same time, we observed increased phospho-TFEB, an inactive form of TFEB, in the H37Rv-infected NCoR1 KD mo-MΦ along with decreased LC3 level, consistent with previous reports (**Fig 5H and 5I**) [21]. These data indicate possible direct control of elevated mTOR signalling
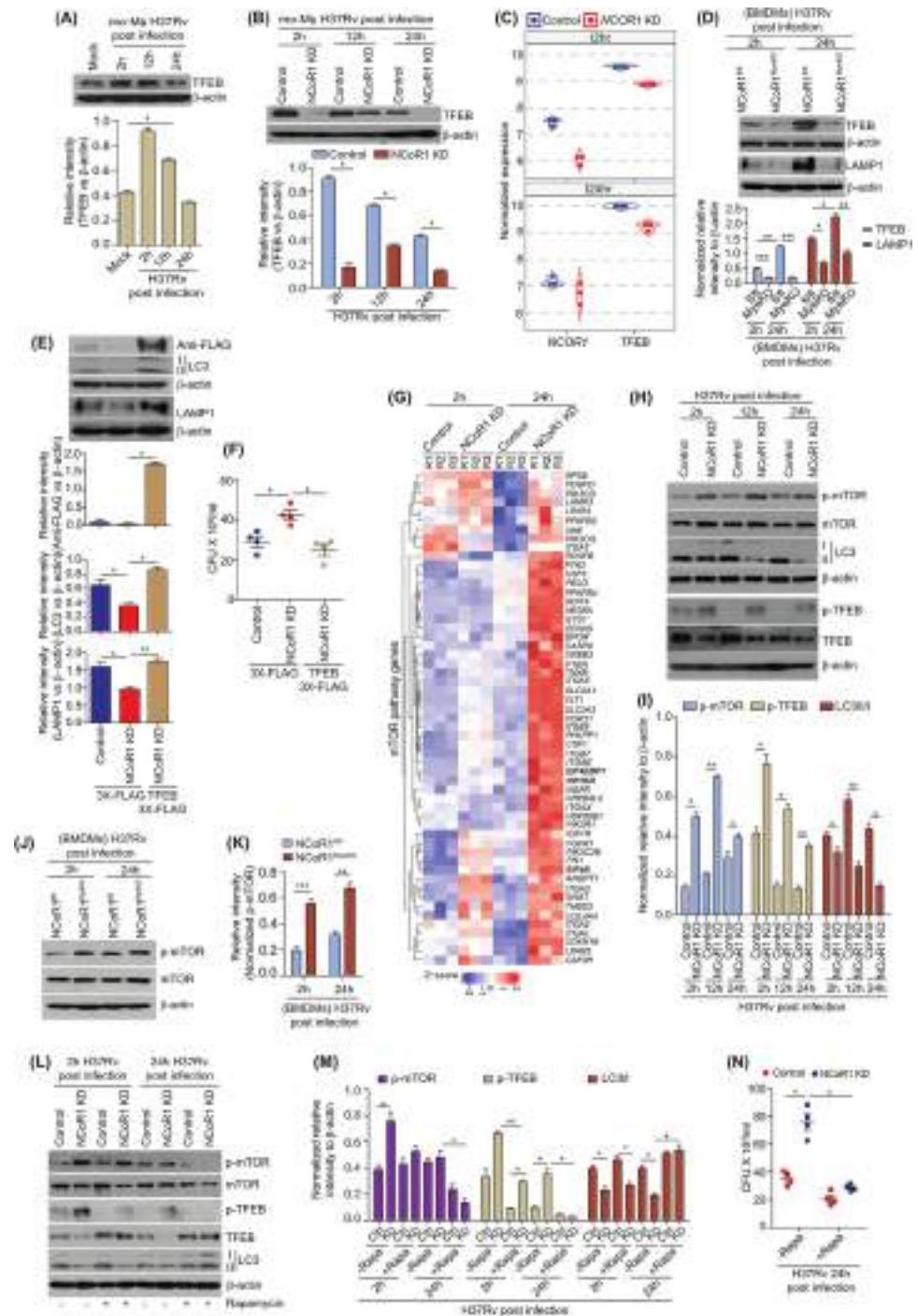
Fig 5. NCoR1 regulates mTOR-TFEB axis to control autophagy induction and lysosomal biogenesis in myeloid cells. (A) Representative western blot image along with bar plots for densitometric analysis depicting the TFEB protein kinetics (2 h, 12 h, and 24 h) in the H37Rv-infected human monocytic THP-1 differentiated macrophages. For normalisation, β-actin was used as housekeeping control (*n* = 3). (B) Western blot image depicting the levels of TFEB protein in H37Rv-infected control and NCoR1 KD human monocytic THP-1 differentiated macrophages at 2 h, 12 h, and 24 h post infection. Corresponding bar plots showing the densitometric analysis from 3 independent biological replicates. For normalisation, β-actin was used as housekeeping control (*n* = 3). (C) Violin plot depicting the normalised transcript expression of TFEB in RNA-seq data of control and NCoR1 KD human monocytic THP-1 differentiated macrophages at 2 h and 24 h post infection (*n* = 3). (D) Representative western blot image with densitometric analysis showing the TFEB and LAMP1 levels in the BMDMs from NCoR1^fl/fl and NCoR1^MyeKO mice at

2 h and 24 h post H37Rv infection. For normalisation, β-actin was used as housekeeping control (*n* = 4 mice). (E) Western blot image along with densitometric analysis showing the levels of LC3, LAMP1, and TFEB-flag in H37Rv-infected NCoR1 KD human monocytic THP-1 differentiated macrophages with or without overexpression of exogenous flag-tagged TFEB at 24 h post infection. For normalisation, β-actin was used as housekeeping control (*n* = 3). (F) Scatter plot demonstrating the H37Rv bacterial load by CFU assay in H37Rv-infected NCoR1 KD human monocytic THP-1 differentiated macrophages with or without exogenous overexpression of flag-tagged TFEB at 24 h post infection (*n* = 4). (G) Heat map showing the DEGs related to mTOR pathway in RNA-seq data of control and NCoR1 KD human monocytic THP-1 differentiated macrophages at 2 h and 24 h post infection (*n* = 3). (H) Representative western blot image depicting the kinetics (2 h, 12 h, 24 h) of phospho-mTOR (p-mTOR), mTOR, phospho-TFEB (p-TFEB), TFEB, and LC3-II:LC3-I protein levels in H37Rv-infected control and NCoR1 depleted human monocytic THP-1 differentiated macrophages (*n* = 3). (I) Bar plot showing the densitometric quantification of p-mTOR, mTOR, p-TFEB, TFEB, and LC3 protein bands from 3 independent biological replicates in H37Rv-infected human control and NCoR1 KD monocytic THP-1 differentiated macrophages at 2 h, 12 h, and 24 h post infection. p-mTOR and p-TFEB were normalised first with total protein levels and then with housekeeping control β-actin. LC3-II density versus LC3-I was quantified followed by normalisation with β-actin (*n* = 3). (J) Representative western blot image depicting the protein levels of p-mTOR and total mTOR in H37Rv-infected BMDMs generated from NCoR1$^{fl/fl}$ and NCoR1^{MyeKO} mice at 2 h and 24 h post infection. For normalisation, β-actin was used as housekeeping control (*n* = 4 mice). (K) Bar plot showing the densitometric quantification of p-mTOR levels from 3 independent biological replicates in H37Rv-infected BMDMs generated from NCoR1$^{fl/fl}$ and NCoR1^{MyeKO} mice at 2 h and 24 h post infection. p-mTOR was normalised first with total m-TOR followed by normalisation with β-actin (*n* = 4 mice). (L) Western blot representative image depicting the p-mTOR, mTOR, p-TFEB, TFEB, and LC3-II:LC3-I levels in H37Rv-infected control and NCoR1 KD human monocytic THP-1 differentiated macrophages at 2 h and 24 h post infection, with and without rapamycin treatment (*n* = 3). (M) Bar plot depicting the densitometric quantification of normalised p-mTOR, p-TFEB, and LC3 protein bands from 3 independent biological replicates. The p-mTOR and p-TFEB levels were normalised first with their respective total protein levels and then with housekeeping control β-actin. LC3-II versus LC3-I levels were quantified followed by normalisation with β-actin (*n* = 3). (N) Scatter plot showing the bacterial load in H37Rv-infected control and NCoR1 KD human monocytic THP-1 differentiated macrophages by CFU assay at 24 h post infection, with and without treatment of rapamycin (*n* = 4). *$p < 0.05$, *$p < 0.01$, and ***$p < 0.001$ using paired and unpaired two-tailed Student's *t* test. Where n represents independent biological replicates. The data underlying this figure are available in S1 Table and S1 Data. Western blot raw images can be found in S1 Raw Image. BMDM, bone marrow-derived macrophage; DEG, differentially expressed gene; KD, knockdown; TFEB, transcription factor EB.

https://doi.org/10.1371/journal.pbio.3002231.g005

on observed reduced TFEB activity in NCoR1 KD myeloid cells. Moreover, we found similar increased phospho-mTOR in BMDMs from NCoR1^{MyeKO} mice (**Fig 5J and 5K**). Next, we hypothesised that mTOR inhibition could rescue the active TFEB and restore autophagy in NCoR1 KD mo-MΦ, leading to decreased bacterial load. We treated the cells with rapamycin, which is well known to inhibit the mTOR activity [60]. Indeed, rapamycin treated with NCoR1 KD mo-MΦ showed reduced phospho-mTOR, confirming the inhibitory effect of rapamycin on mTOR activity (**Fig 5L and 5M**). We found decreased phospho-TFEB and increased TFEB with LC3-II levels in mTOR inhibited condition of NCoR1 KD mo-MΦ at 2 h and 24 h post H37Rv infection (**Fig 5L and 5M**). Moreover, we observed a comparable elevation of TFEB level when we used Torin1, which is a more specific mTOR inhibitor. At the same time, we observed a down-regulation of phospho-TFEB and phospho-mTOR (**S5O and S5P Fig**) [58]. In addition, rapamycin treated NCoR1 KD mo-MΦ showed decreased H37Rv bacterial load compared to untreated conditions in CFU and flow cytometry analysis (**Figs 5N, S5Q and S5R**). These findings elucidated how NCoR1 impacts the mTOR-TFEB axis, which in turn regulates the genes involved in autophagy and the lysosomal pathway in myeloid cells.

NCoR1 regulates mTOR activity by fine-tuning cellular ATP-AMPK levels

mTOR has been shown to sense different kinases to integrate different signalling axes to tailor key physiological processes based on specific local cues [61,62]. Using differentially expressed genes (DEGs) from RNA-seq data (**S1 Table**), we performed pathway enrichment analysis to comprehend the molecular signalling under the NCoR1 depleted condition. We found that the PI3K-AKT-mTOR pathway was the top signalling pathway up-regulated at 24 h in NCoR1 KD cells, while the proteasome pathways were down-regulated. (**Figs 6A and S6A and S2 Table**).

It has been well reported that mTORC regulates autophagy, which is known to be negatively regulated by phosphorylated AMPK [63]. Next, we investigated the levels of phospho-AMPK (p-AMPK) in NCoR1 KD mo-MΦ that showed significantly increased phospho-mTOR. NCoR1 KD mo-MΦ showed lower AMPK activity at 2 h and 24 h post *Mycobacterium* infection, which is consistent with the mTOR activity (**Fig 6B and 6C**). AMPK is a key sensor for dynamic ATP concentration in cells and responds inversely to cellular energy state with respect to mTOR [15,64]. Moreover, NCoR1 is well reported to modulate the expression of different metabolic genes [26,65,66]. Recently, it has been reported that liver-specific NCoR1 knock out (KO) mice showed elevated level of ATP and increased mitochondrial reactive oxygen species, which subsequently blocks the process of diethylnitrosamine (DEN)-induced HCG in mice [29]. We therefore considered whether NCoR1 KD mo-MΦ has a similar kind of perturbation at cellular energy levels upon bacterial infection or not. We found that NCoR1 KD mo-MΦ has elevated intracellular levels of ATP at 2 h and 24 h of *M. smegmatis* infection as compared to control cells (**Fig 6D**). In addition, BMDMs from NCoR1^{MyeKO} also showed increased ATP level as compared to WT BMDMs (**Fig 6E**). Next, we addressed the metabolic state in NCoR1 depleted cells using the Seahorse extracellular flux assay, where we found a similarly increased coupled ATP production rate through elevated OXPHOS in NCoR1 KD mo-MΦ (**Figs 6F, 6G, and S6B**). Similar observations are also attained in NCoR1 ablated cDC1 DCs reported previously [30]. To identify the role of AMPK/mTOR signalling culminating into dysregulated autophagy in NCoR1 KD mo-MΦ upon mycobacterial infection, we treated the cells with metformin, an AMPK activator. We found that metformin-treated NCoR1 KD mo-MΦ showed increased AMPK activity which in turn decreased the levels of p-mTOR leading to protection from *M. smegmatis* infection suggesting the NCoR1 mediated regulation of AMPK/mTOR pathway controlling the mycobacterial load through autophagy (**Fig 6H and 6I**). We further sought to confirm the role of NCoR1 mediated increased ATP levels in the compromised autophagy process leading to increased *Mtb* infection. We treated *M. smegmatis* infected cells with antimycin-A, an inhibitor of complex III of ETC, to deplete the ATP level at 6 h post infection. Antimycin-A treatment reduced the ATP levels and a subsequent reduction in infection levels were observed in NCoR1 KD mo-MΦ upon *M. smegmatis* infection (**S6C–S6G Fig**). Moreover, we observed that antimycin-A treated NCoR1 KD mo-MΦ had recovered AMPK activity, which consequently led to decreased levels of p-mTOR leading to increased TFEB and LC3-II:LC3-I (**S6H and S6I Fig**). In all the experiments, more than 90% cell viability upon antimycin-A treatment (0.125 μm to 0.25 μm) was confirmed by FACS (**S6J Fig**). We further confirmed our rescue experiments in BMDMs generated from NCoR1^{MyeKO} and found significant rescue from *Mtb* infection upon rapamycin, antimycin-A, and metformin treatments (**Fig 6J**). To complement our results that NCoR1 is a key candidate to control the pathogenesis of *Mtb* in the host and it could be a putative target in controlling *Mtb* infection, we overexpressed exogenous NCoR1 in NCoR1 depleted mo-MΦ. We found that exogenous delivery of NCoR1 was sufficient to restore the compromised AMPK/mTOR signalling leading to recovered LC3-II levels (**Fig 6K and 6L**). Moreover, exogenous NCoR1 complementation rescued the NCoR1 KD mo-MΦ from the susceptibility to *Mtb* infection (**Fig 6M**). Altogether, these results confirmed and propose an important role of NCoR1 in balancing the cellular ATP sensor AMPK-mTOR-TFEB pathway upon *Mtb* infection for the optimal induction of TFEB activity, hence, its clearance through auto-phagolysosome pathway (**Fig 6N**).

Discussion

This investigation is the first report depicting the role of NCoR1 mediated fine-tuning of the auto-phagolysosomal pathway in regulating *Mtb* pathogenesis through the AMPK-
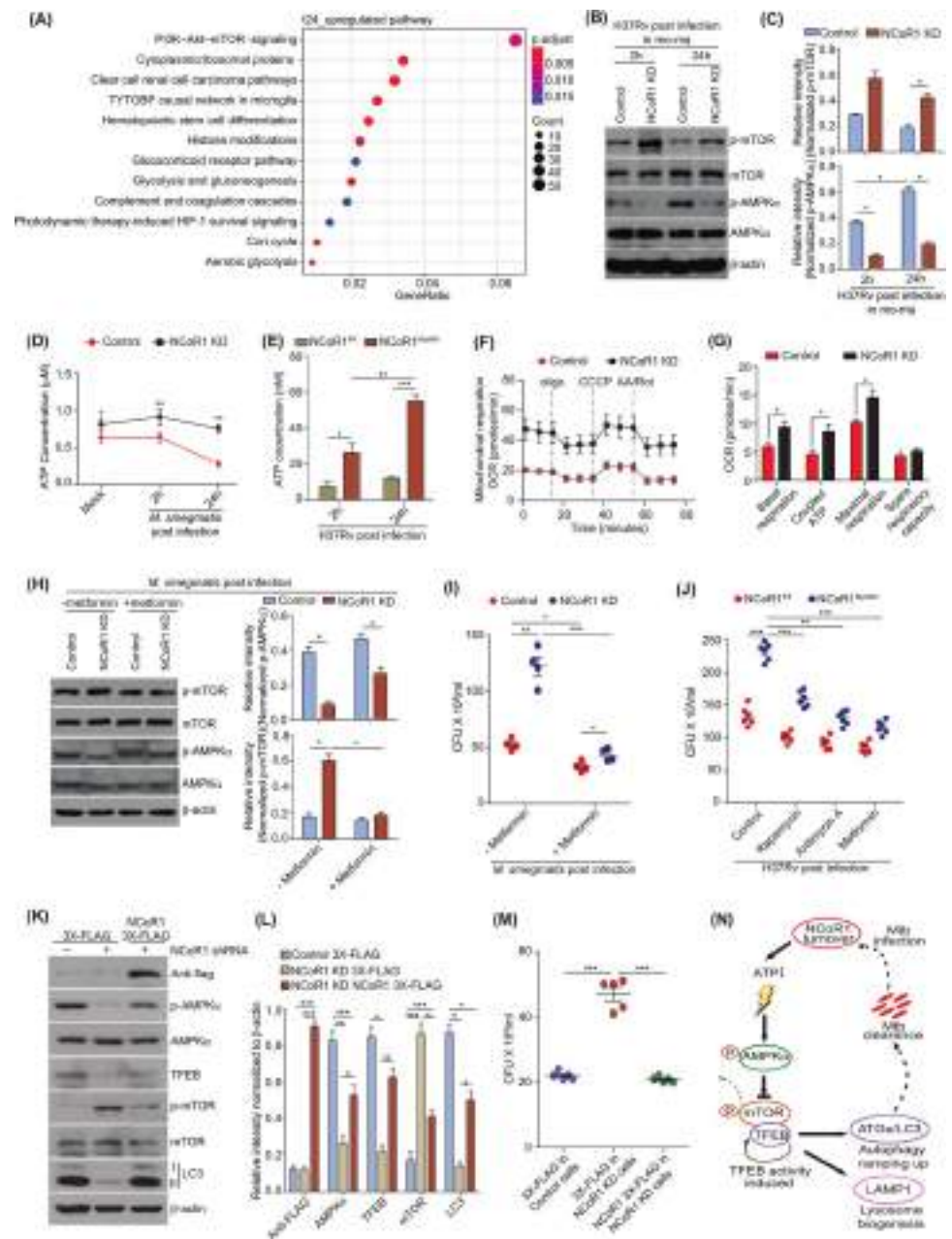
Fig 6. NCoR1 regulates mTOR activity by fine-tuning cellular ATP-AMPK levels. (A) Pathway enrichment analysis showing the top pathways enriched for the list of genes significantly up-regulated in RNA-seq data of NCoR1 KD human monocytic THP-1 differentiated macrophages at 24 h post infection with H37Rv (*n* = 3). (B, C) Representative western blot image depicting the p-mTOR, p-AMPKα along with total mTOR, AMPKα in H37Rv-infected control and NCoR1 KD human monocytic THP-1 differentiated macrophages at 2 h and 24 h post infection. Corresponding bar plots showing the densitometric analysis from western blots of 3 independent biological replicates (*n* = 3). (D) Line graph showing the intracellular ATP levels in *M. smegmatis*-infected control and NCoR1 KD human monocytic THP-1 differentiated macrophages at 2 h and 24 h post infection (*n* = 3). (E) Bar graph depicting the intracellular ATP levels in NCoR1^fl/fl and NCoR1^MyeKO BMDMs at 2 h and 24 h post H37Rv infection (*n* = 4 mice). (F) Representative seahorse assay line graph showing the OCR levels upon sequential injections with Oligomycin, CCCP, and Rotenone/ Antimycin A, measured in *M. smegmatis*-infected control and NCoR1 KD human monocytic THP-1 differentiated macrophages at 2 h and 24 h post infection (*n* = 4). (G) Bar plot depicting the quantification of OCR levels as basal respiration, coupled ATP, maximal respiration, and spare respiratory capacity, measured by seahorse assay, of *M. smegmatis*-infected control and NCoR1 KD human monocytic THP-1 differentiated macrophages at 2 h and 24 h post infection (*n* = 4). (H) Western blot representative image with corresponding densitometric analysis depicting the p-mTOR, p-AMPKα along with total mTOR, AMPKα protein level in *M. smegmatis*-infected control and NCoR1 KD

human monocytic THP-1 differentiated macrophages at 24 h post infection, with and without metformin treatment. All phosphorylated proteins were first normalised with its total form followed by housekeeping control β-actin (*n* = 3). (I) Scatter plot showing the *M. smegmatis* bacterial load in control and NCoR1 KD human monocytic THP-1 differentiated macrophages by CFU assay at 24 h post infection, with and without metformin treatment (*n* = 4). (J) Scatter plot showing the bacterial load in H37Rv-infected BMDMs at 24 h post infection by CFU assay, with and without treatment of antimycin A, rapamycin, and metformin. BMDMs were generated from NCoR1^{MyeKO} and NCoR1$^{fl/fl}$ mice (*n* = 6 mice). (K) Western blot image demonstrating the protein levels of exogenously expressed NCoR1-flag and its impact on p-AMPKα, AMPKα, TFEB, p-mTOR, total mTOR, and LC3-II:LC3-I in H37Rv-infected NCoR1 KD human monocytic THP-1 differentiated macrophages (*n* = 3). (L) Bar plot showing the densitometric quantitation of western blot bands of NCoR1-flag, p-AMPKα, TFEB, p-mTOR, and LC3 protein levels from 3 independent biological replicates of H37Rv-infected NCoR1 KD human monocytic THP-1 differentiated macrophages complemented with exogenous NCoR1-flag. All phosphorylated proteins were first normalised with its total form followed by housekeeping control β-actin (*n* = 3). (M) Scatter plot showing the bacterial load in H37Rv-infected control, NCoR1 KD, and exogenous NCoR1-flag overexpressed NCoR1 KD in human monocytic THP-1 differentiated macrophages by CFU assay at 24 h post infection (*n* = 5). (N) Cartoon diagram showing the proposed mechanism of NCoR1 regulating *Mtb* pathogenesis in myeloid cells. *$p < 0.05$, *$p < 0.01$, and ***$p < 0.001$ using paired and unpaired two-tailed Student's *t* test. Where n represents independent biological replicates. The data underlying this figure are available in S2 Table and S1 Data. Western blot raw images can be found in S1 Raw Image. AMPK, AMP-activated protein kinase; ATP, adenosine triphosphate; BMDM, bone marrow-derived macrophage; KD, knockdown.

https://doi.org/10.1371/journal.pbio.3002231.g006

mTOR-TFEB signalling axis. Increased expression of NCoR1 in myeloid cells during the early stage of *Mycobacterium* infection demonstrated its importance for the control of host defence against infection. NCoR1 loss of function impairs the clearance of H37Rv and *M. smegmatis* infection in myeloid cells by fine-tuning the AMPK-mTOR signalling axis, which in turn regulates TFEB activity. TFEB autonomously controls autophagic machinery and lysosomal biogenesis, giving *Mtb* a survival advantage in NCoR1 depleted condition. Overexpression of TFEB in NCoR1 depleted macrophages recovered the LC3 and LAMP1 expression and thus cleared the bacterial load. Active mTOR phosphorylates TFEB to inhibit translocation to the nucleus and thus hinder autophagy and lysosome biogenesis [21]. These reports were found to be consistent with our observations. Moreover, pharmacological inhibition of mTOR by rapamycin/Torin1 and activation of AMPK with metformin restored autophagy and consequently protected the macrophages from *Mtb* infection. Overall, our study showed that NCoR1 can influence *Mtb* survival in myeloid cells via modulating the auto-phagolysosomal machinery. NCoR1 has also been shown to regulate diverse biological functions [24]. Our and other previous reports have shown the role of NCoR1 in controlling anti-inflammatory and tolerogenic phenotype in macrophages and DCs, respectively [40,67]. However, any evidence for NCoR1 in regulating autophagy and lysosome biosynthesis processes and *Mtb* survival in host cells has not been reported. These findings gave strong indication that NCoR1 levels are crucial at early stages of *Mtb* infection in myeloid cells to protect from pathology. Among myeloid cells, DCs are also required to activate the systematic immune system to protect microbial insult [66,68]. cDC1 showed peak expression of TFEB earlier as compared to mo-MΦ upon *Mtb* infection that supports the urgency of TFEB mediated induction of autophagy process to control *Mtb* infection. Mechanistically, we demonstrated that NCoR1 regulates TFEB, and its depletion diminishes the auto-phagolysosome formation in cells, making them more susceptible to *Mtb* pathogenesis. To gain a global insight, we looked into the transcriptomics data of *Mtb*-infected NCoR1 KD cells and found key autophagy inducing genes like ATG13, ATG3, and ATG5 to be down-regulated. These ATGs are well reported to drive the autophagy induction process through optimal auto-phagosome maturation and LC3 lipidation [69–71]. We are hypothesising that NCoR1 might provide functional stoichiometry to autophagy machinery proteins in myeloid cells which is important to control *Mycobacterium* pathogenesis. On the other side, NCoR1 has been widely reported to regulate metabolic processes including fatty acid and lipid oxidation, mitochondrial respiration, and ATP synthesis [26,40,67]. We observed an increased

mitochondrial ATP as well as total cellular ATP in *M. smegmatis*-infected mo-MΦ. *Mycobacterium* mediated changes in host cell oxidative phosphorylation has been shown to be critical for their survival fitness [72–74]. Several reports have shown various evidences where *Mycobacterium* can manipulate cellular energy homeostasis by regulating AMPK-mTOR signalling to its own proliferation and survival [75,76]. Cellular energetic state is tightly monitored by AMPK-mTOR pathway to maintain homeostasis. AMP/ATP ratio sensed by AMPK in turn modulates the mTOR activity to operate optimum autophagic flux, hence refuelling required energy in cellular stress conditions [16,65,77]. As NCoR1 depletion is known to regulate energy homeostasis even without any infection, we performed starvation and heat-killed *Mtb* treatment experiments and found NCoR1 KD cells to have decreased autophagy process, suggesting the role of NCoR1 protein as an important component for the regulation of autophagy machinery. In addition, antimycin-A treatment reduced the p-mTOR levels and increased the AMPK activity, which in turn decreased the *Mtb* survival with the recovery of TFEB and LC3 levels. These results confirmed our observation that NCoR1 fine-tunes the AMPK-mTOR pathway by maintaining an optimal cellular energy state to control the intracellular *Mtb* survival. This mechanistic insight provided us 2 possible roles of NCoR1, first is the interaction with TFEB for its functionality or stability, and second is the regulation of AMPK-mTOR signalling. In conclusion, we revealed here a direct role of NCoR1 in controlling *Mtb* survival by maintaining optimum auto-phagolysosomal process. Furthermore, our results also revealed a clinically significant correlation of NCoR1 expression during active TB infection, which is restored after 12 months of TB treatment, showing a clear link between them. Similar findings were made in *Mtb*-infected PBMCs, where early infection showed increased NCoR1 expression, which thereafter decreased at 24 h. Therapeutically, NCoR1 might be a potential candidate for host-directed therapy.

Materials and methods

Ethics statement

Human primary PBMCs used for the experiment were isolated from 10 ml of venous blood isolated from 4 adult healthy control donors at the Institute of Life Sciences, Bhubaneswar, Odisha, India, with necessary ethical approval. The anonymised details of the individuals are provided in Table C in **S3 Table**. The Ethics Committee of the Institute of Life Sciences granted ethical permission for human subject PBMC samples. All procedures were fully compliant with the declaration of Helsinki 2013: the ethical principles for medical research involving human subjects. Before PBMCs were collected for ex vivo investigations as well as comprehensive confocal and qRT-PCR analyses (representative **Fig 1D**, **1E,** and **S1A**), the individuals gave written informed consent, and all the subject data was anonymised. The respective ethics statement for curated publicly available RNA-seq datasets used in representative **Fig 1A** and **1B** are available in the respective publications mentioned in Tables A and B in S3 Table.

Generation of stable NCoR1 KD in THP-1 human monocytes and cDC1 murine DCs

Lentiviral vector pLKO.1 (Sigma) containing NCoR1-specific shRNAs or control shRNA were used to develop stable NCoR1 KD and corresponding control THP-1 cells. Viral particles containing shRNA and packaging plasmids were generated using CalPhos Mammalian Transfection Kit (Takara, 631312) according to the previously used protocol [40]. After transfection, viral particles were concentrated at $50,000 \times g$ in an ultracentrifuge at 16°C for 2 h. Then,

THP-1 cells were transduced with concentrated virus particles and cultured for 72 h in presence of 8 μg/ml of polybrene. Transduced THP-1 cells were then selected using puromycin containing culture media for an additional 2 weeks. The efficiency of NCoR1 KD was quantified using NCoR1 gene-specific primers by qRT-PCR. We employed the CD8^{+} cDC1 mutu-cDC1 line developed by the research group of Prof. Hans Acha-Orbea. These DC lines have been thoroughly studied and compared to primary CD8^{+} cDC1 DCs, and researchers found that they completely mirror immature CD8^{+} DCs that were isolated from C57BL/6 mice's spleen in ex vivo studies. Control and stable NCoR1 KD cDC1 were directly used for experiments which were characterised previously [39,40,78].

Cell culture

NCoR1 KD THP-1 cells and NCoR1 KD cDC1 were cultured in RPMI 1640 (Gibco Laboratories) and IMDM (Gibco Laboratories), respectively, supplemented with 10% FBS (Gibco Laboratories). Cells were maintained with their respective controls at a cell density of 2.0 to 10.0×10^5 cells per ml with puromycin (1 μg/ml) at 37˚C in a humidified, 5% CO_2 atmosphere and the KD was confirmed before performing each experiment. The DCs were raised in IMDM-glutamax (GIBCO) that had been buffered with $NaHCO_3$ and supplemented with 8% to 10% heat-inactivated FCS (to test for endotoxin toxicity toward DC cultures), 10 mM HEPES (GIBCO 15630), 50 μm β-Mercaptoethanol (GIBCO 31350), 50 U/ml of penicillin, and 50 g/ml of streptomycin (GIBCO 15070). The cells were kept at 37˚C in an incubator that was humidified and contained 5% CO_2. These DCs were separated after a brief incubation at 37˚C in a non-enzymatic cell dissociation solution containing 5 mM EDTA (5 mM EDTA in 20 mM HEPES-PBS).

cDC1 cells were seeded in 96-well plates at a density of 1.0×10^4 cells per well or in 6-well plates at a density of 2.5×10^6 cells per well prior to infection, while THP-1 cells were being differentiated with PMA (Sigma, P1269) at a concentration of 20 ng/ml for 17 h prior to infection. THP-1 cells were also plated with the same number of cells as cDC1.

Bacterial culture

Mycobacterium sp. were grown mid-log phase on selective media Middlebrook 7H9 broth (BD Difco, Becton Dickinson) supplemented with 10% ADC (Becton Dickinson), 0.4% Glycerol and 0.05% Tween-80. mCherry-tagged and GFP-tagged *M. tuberculosis* and *M. smegmatis* were used for microscopy and FACS experiments.

Infection with *Mycobacterium* species

For infection, *Mycobacterium tuberculosis* (H37Rv strain) or *Mycobacterium smegmatis* single-cell suspensions were prepared and opsonized in antibiotic-free RPMI or IMDM media [9]. Bacteria were quantified by measuring the absorbance at a wavelength of 600 nm (0.6 O.D. corresponds to approximately 100×10^6 bacteria). Cells were infected with an MOI of 1:10 for 2 h followed by 3 times washing by prewarmed FCS-free RPMI media or IMDM media to remove extracellular bacteria. FLAG-tagged TFEB and FLAG-tagged NCoR1 were expressed in NCoR1 KD THP-1 cells by electroporation (Neon Transfection System 100 μl Kit, MPK10025) for 48 h followed by differentiation and infection as explained above.

PBMCs

For validating the results in primary human macrophages, 10 ml venous blood was obtained from healthy donors in EDTA tubes followed by PBMC separation using lymphoprep

(STEMCELL Technologies, 07801/07811). Cells were counted using trypan blue stain using a haemocytometer and 1.0×10^6 cells were plated in 12-well plates. Before infection, the cells (monocytes) were differentiated into macrophages using 20 ng/ml Human GM-CSF (Prospec-bio, CYT-221) for 5 days.

Phagocytosis assay

Cells were incubated with either *M. smegmatis*-GFP at an MOI of 10 or 1.0 μm yellow-green poly-styrene latex microbeads (Sigma Aldrich, L4655) in the ratio of 10 particles per cell. Incubation conditions included 37°C and 5% CO_2. *M. smegmatis*-GFP or latex beads phagocytosed cells were washed twice with 1× PBS before harvesting, i.e., 10 min, 30 min, and 60 min of incubation, and then they were stained for 10 min at 4°C using Live Dead Fixable Violet Dead Cell Stain Kit (Thermo Fisher Scientific, L34955) [43]. After washing, cells were resuspended in FACS buffer and acquired on BD LSR Fortessa Cell Analyzer (BD Biosciences). Acquired data was analysed using FlowJo-X software (Treestar). In parallel, CFU assay was performed for phagocytosis assay. Infected cells were collected at 10 min, 30 min, and 60 min intervals and lysed in 100 μl of 0.06% of SDS for 10 min at room temperature. Lysates were diluted by 7H9 broth in the ratio 1:10, 1:100, 1:1,000, and 1:10,000 and plated separately in duplicate sets on 7H11 agar plates supplemented with OADC (Becton Dickinson) and 0.5% glycerol and counted on day 21.

Generation of myeloid-specific NCoR1 knockout mice (NCoR1^{MyeKO})

The CD11c-specific NCoR1 KO homozygous mice were bred with the LysM cre FVB mice to obtain heterozygotes in the F1 generation. Further, the F1 mice were backcrossed with the NCoR1 KO Cd11c-Cre homozygous KO parent to obtain F2. Approximately 25% of the F2 mice showed NCoR1-loxP, CD11c-Cre, and LysM-Cre. These 25% of F2 were self-crossed to obtain F3. F3 generation thus obtained were having 25% of control mice exhibiting only NCoR1-loxP sites and 50% were showing both CD11c-Cre, LysM-Cre along with NCoR1-loxP. Further, to obtain proper inbred genotype, crossing was continued till 10 generations to select experimental mice. Selections were strongly adhered to the mouse genotyping results, added in (S2M Fig). LysM-cre mice were chosen due to their high fecundity rate. Since obtaining a pure homozygous breed takes at least 10 crosses [79]. Moreover, crossing C57BL/6 with FVB strains has no profound effect on systemic cytokine levels [80]. Adult mice of 6 to 8 weeks of age of both sexes were used indiscriminately. All the animal experiments were performed after getting due approval from the institutional animal ethics committee.

BMDM

Mice between the age of 6 to 8 weeks old were humanely euthanized by CO_2 asphyxiation, and their tibias and femurs were taken for experiments. Bone marrow cells were extracted using RPMI-1640 media supplemented with 10% FCS. In 6-well plates, the cells were seeded at a density of 1.0×10^6 cells/ml, and they were cultured with M-CSF at a concentration of 20 ng/ml for a period of 5 days. Following that, these cells were subsequently infected with H37Rv at a number of infection (MOI) of 1:10, as mentioned earlier, and more experiments were carried out further down the line.

Peritoneal macrophages

Mice 6 to 8 weeks of age were humanely euthanized by CO_2 asphyxiation and were dissected out keeping the peritoneal membrane intact. Approximately 5 ml of RPMI-1640 media was injected into the peritoneal cavity. The cells were collected after whirling the cavity for 5 min.

CFU determination *Mtb*-infected cells

H37Rv post-infected cells at different time points were collected and lysed in 100 μl of 0.06% of SDS for 10 min at room temperature. Lysates were diluted by 7H9 broth in the ratio 1:10, 1:100, 1:1,000, and 1:10,000 and plated separately in duplicate sets on 7H11 agar plates supplemented with OADC (Becton Dickinson) and 0.5% glycerol.

Intranasal infection of mice with *Mtb*

Before infection, culture of *Mtb*-GFP (H37Rv) bacilli at logarithmic phase ($OD_{600} = 0.5-0.6$) was aspirated using a 30-gauge needle for 15 to 20 times in order to prevent clumping. To infect mice, anaesthetized animals were given an inoculation of 20 μl containing 10^5 live bacilli through an intranasal route. Day 1 post infection, the inoculum dose was tracked and controlled by analysing the bacterial load that was present in the lungs of infected mice (10^4/lung) [45].

Organ processing

Control (*Mtb*), NCoR1$^{fl/fl}$ (*Mtb*-GFP), and NCoR1^{MyeKO} (*Mtb*-GFP) mice were humanely euthanized and dissected to collect lung and spleen. Tissues were processed for flow cytometry, CFU, histology, and bioplex. Histology samples were kept in 10% formalin and rest were treated with 0.5mg/ml collagenase A (10103578001, Sigma) in RPMI (10% FBS) and incubated for 20 min at 37˚C. For single cell suspension, they were RBC lysed and filtered with a 70 μm filter. Samples were then taken for flow, CFU, and bioplex.

CFU determination in organs

At a variety of post infection time points, i.e., day 7 and day 21, the levels of bacterial load in the lung and spleen of *Mtb*-infected mice were evaluated. In brief, organs from NCoR1$^{fl/fl}$ and NCoR1^{MyeKO} mice that had been humanely euthanized were extracted in an aseptic manner and then homogenised in 0.04% Tween 80. Difco Middlebrook 7H11 Agar (BD Biosciences) plates supplemented with 10% OADC (BD Biosciences) and 0.5% glycerol were used to grow colonies from serial dilutions, which were cultured at 37˚C for 21 days before counting.

FACS from organ

For flow, single-cell suspensions were first stained with live/dead Zombie UV fixable dye (1:1,000 diluted in 1× PBS) for 30 min at RT (as per the manufacturer's instruction) followed by washing with FACS buffer (3% FBS in 1× PBS). Cells were then stained with a combination of fluorochrome conjugated anti-mouse antibodies (according to the different multicolour group panel) in the FACS buffer for 45 min on ice. The panel comprised of CD45 (BUV496, BD, 423108), CD11c (ef450, ebioscience, 48-0114-82), Ly6C (BV711, biolegend, 128037), Ly6G (PerCP-Cy5.5, biolegend, 127616), MHCII (PerCP-eFlour710, ebioscience, 46-5320-82), Siglec F (APC, biolegend, 155507), F4/80 (AF700, biolegend, 123130), CD11b (APC-Cy7, tonbo, 25-01120U100), CD3 (PeCy5, tonbo, 55-0031-U100), CD8a (APC, tonbo, 20-1886-U100), CD4 (AF700, ebioscience, 56-0042-82), CD19 (APCeF780, ebioscience, 56-0042-82), and CD44 (eF450, ebioscience, 48-0441-82).

Thereafter, cells were washed, fixed in 2% PFA, and acquired on a Cytek Aurora (5 laser and 64 fluorescent detectors). Unmixing was performed using SpectroFlo version (Cytek) software. Auto-fluorescence was removed from the inbuilt software. Gating for *Mtb*-GFP positive infection was in accordance with *Mtb* infected un-tagged negative tissue samples. Further,

FMO controls were used to demarcate specific myeloid and lymphoid populations in lungs and spleen. Data were analysed with FlowJo version 10 and compiled in Prism software 8.0.2.

FACS from cell line

For the flow cytometric analyses of NCoR1 KD THP-1 differentiated macrophages and NCoR1 KD cDC1, post-infected cells were dissociated from plates according to their corresponding time point and washed 3 times with FACS buffer (3% FCS in 1× PBS, 5 mM EDTA). After washing, the cells were acquired for *Mtb* load analysis on Aria II Cell Sorter (BD Biosciences). The acquired data was analysed using FlowJo-X software (Treestar).

Bio-plex assay

Using a 23-plex mouse Cytokine Panel (M60009RDPD, Biorad) and a Bio-plex (multiplex ELISA-Luminex) reader, cytokines were analysed in *Mtb*-infected lung homogenates from NCoR1$^{fl/fl}$ and NCoR1^{MyeKO} mice, according to the recommended protocol. Prior to beginning the process of quantifying cytokines in the lung tissue samples, a commercial BCA test was done as recommended by Thermo Scientific to normalise the amounts of total protein in the lung lysate samples [81–83].

Tissue immunofluorescence

Triple immunofluorescence was performed in paraffin embedded murine tissue sections. The lung tissues were dewaxed in xylene for 5 min with 2 changes, followed by an acetone dip for 2 to 3 min followed by rehydration by sequential grades of alcohol for 5 min each. Antigen retrieval was done with proteinase-K solution (20 μg/ml) in 1× PBST (1× PBS + 0.05% Tween-20) followed by 3 washes in 1× PBS. The dewaxed sections were blocked by incubation with a blocking buffer (3% goat serum + 3% BSA in 1× PBST) for 1 h in dark at RT. Primary antibody staining for NCoR1 (1:400), TFEB (1:400), CD11c (1:400), and F4/80 (1:400) was done in 3% BSA in 1× PBST kept in a humidified chamber for 2 h in dark at RT. Subsequent secondary Ab (1:800) incubation was performed with the same buffer composition in a non-humidified chamber for 1 h in dark at RT. Sequential staining was performed with different combinations (CD11c and NCoR1 and F4/80 and NCoR1) followed by TFEB. Finally, the tissue sections were mounted with antifade-mounting media and observed under a microscope.

Lung inflammation histopathology

For histopathology, lung tissue samples were collected, fixed in 10% neutral-buffered formalin, embedded in paraffin, cut into sections measuring 5 to 6 μm, and stained using the HE stain. The degree of inflammation in the mice's lungs was assessed as previously mentioned [84]. In order to determine the lung area that was affected, HE-stained lung sections were photographed under a microscope at a magnification of about 5, 10, and 20.

Inhibitor and inducer treatments

Before harvesting the cells, Bafilomycin A1 (Invivogen, tlrl-baf1) and Rapamycin (Invivogen, tlrl-rap) were added at 100 nM and 20 nM, respectively, for 2 h and 24 h to monitor autophagy flux. In order to determine whether or not the phosphorylation of TFEB at Ser211 was reliant on mTORC activity, we treated Control versus NCoR1 KD THP-1 differentiated *Mtb*-infected cells with another mTOR inhibitor, Torin1, at 250 nM concentration (Selleckchem, S2827) [85]. Following *Mtb* infection, protein expressions were analysed using western blotting. Cells were also treated with 0.125 μm Antimycin-A (Sigma, A8674) prior to H37Rv infection and

harvested post infection at 6 h for CFU assay, western blot, and FACS. Cell viability assays of Antimycin-A treated cells were performed with the LIVE/DEAD Fixable Violet Dead Cell Stain Kit (Thermo Fisher Scientific, L34955). Further, metformin (20 nM) treatment was done (Sigma, 317240) to quantitate survival by CFU assay.

Immunoblotting

Cells were lysed in buffer containing 1% tritonX-100, 0.1% SDS, 50 mM HEPES (pH 7.5), 150 mM NaCl, 100 mM NaF, 10 mM EDTA, 10 mM $Na_4P_2O_7$, and protease inhibitors (Roche). BCA assay (Pierce BCA Protein Assay Kit, 23225) was used for protein estimation. Cell lysates were separated by SDS-PAGE and transferred onto Nitrocellulose membrane (BIO-RAD, 1620112). Membranes were then probed with primary antibodies of TFEB (Cell Signaling Technology, 4240S), NCoR1 (Abcam, ab24552), LC3 (Cell Signaling Technology, 2775S), Phospho-mTOR (Ser2448) (Cell Signaling Technology, 5536S), mTOR (Cell Signaling Technology, 2972S), Phospho-AMPKα (Cell Signaling Technology, 50081T), AMPKα (Cell Signaling Technology, 5831T), Beclin1 (Cell Signaling Technology, 3495S), ATG12 (Cell Signaling Technology, 4180S), FLAG (Cell Signaling Technology, 14793S), Phospho-TFEB (Ser211) (Cell Signaling Technology, 37681S), LAMP1 (Cell Signaling Technology, 3243S), and β-actin (Cell Signaling Technology, 8457S).

Immunofluorescence (in vitro and ex vivo)

After each time point, cells were washed with 1× PBS and fixed with 4% paraformaldehyde (Sigma) for 20 min, followed by 3 washes with 1× PBS. The cells were permeabilized using 0.2% (w/v) TritonX-100 prepared in 1× PBS for 20 min and blocked with 3% (w/v) BSA and 0.5% Tween20 in 1× PBS for 1 h. After blocking, cells were stained for 2 h at RT with a primary antibody (1:200), washed thoroughly 3 times with 1× PBST (0.5% Tween20 in 1× PBS), then incubated for 45 min at RT with suitable Alexa-Fluor conjugated secondary antibodies (1:500). After incubation, the cells were washed 3 times in 1× PBS and mounted with an antifade-DAPI mounting solution (Invitrogen, P36983) before being examined under a microscope. Primary antibodies used in the study were TFEB (Cell Signaling Technology, 4240S), NCoR1 (Abcam, ab24552), LC3 (Cell Signaling Technology, 2775S), and LAMP1 (Cell Signaling Technology, 3243S).

RNA extraction and qRT-PCR

RNA was extracted from NCoR1 KD THP-1 cells or PBMCs-derived macrophages using NucleoSpin RNA Plus miniprep kit (Macherey-Nagel 740984.250) as per manufacturer's manual. Then, cDNA was synthesised using the Transcriptor First-Strand cDNA Synthesis Kit (Roche Applied Science, Indianapolis, Indiana, United States of America). For gene expression analysis, qRT-PCR was performed using Power SYBR Green PCR Master Mix (Invitrogen) on a QuantStudio-6 Flex Real-Time PCR System (The Applied Biosystems). Human and mouse-specific primers used for qRT-PCR are provided in **S4 Table**.

ATP determination assay

Intracellular ATP was evaluated using an ATP determination kit (Invitrogen, A22066), according to the manufacturer's instructions. NCoR1 KD and Control THP-1 differentiated macrophages (approximately 10^5 cells) were infected with *Mycobacterium* (1:10 MOI) and intracellular ATP was extracted at various time intervals. Dissociated cells were pelleted and washed twice with 1× PBS after centrifugation at 12,000 × g for 10 min. After that, 1 ml boiling

water (90˚C) was added to the cell pellet and vortexed vigorously to extract the cellular ATP. Following the vortex, the lysed cells were centrifuged at $12,000 \times g$ for 5 min at 4˚C, with 20 μl of the suspension used for bioluminescence measurement as directed by the kit manufacturer. Serial dilutions of 10 μm ATP solution were used to generate the ATP standard curve.

Extracellular flux assay (Seahorse)

Mito-Stress Test (Agilent technologies, 103010–100) was performed on a Seahorse XFp extracellular flux analyzer. Control and NCoR1 KD cells were plated on a sterile XFp plate (Agilent technologies, C21119) in triplicates at 2.0×10^4 total cells per well with sequential additions of the following compounds 1 μm oligomycin, 2 μm carbonyl cyanide-4-(trifluoromethoxy) phenylhydrazone (CCCP), and 1 μm rotenone/antimycin-A. All the chemicals were prepared according to the manufacturer's protocol. Respiratory parameters like basal oxygen consumption rate (OCR), coupled ATP production, maximal respiratory capacity, and spare respiratory capacity were calculated using the WAVE software.

Library preparation for RNA-seq

Total RNA was extracted from *Mtb*-infected THP-1 differentiated macrophages with RNeasy Plus Mini Kit according to the manufacturer's instructions. The RNA was quantified by Nano-Drop 2000 Spectrophotometer and purity was assessed by a 2100 Bioanalyzer (Agilent Technologies, Waldbronn, Germany). RNA integrity number (RIN) >8, RNA was taken for library preparation. llumina TruSeq Stranded Total RNA Library Prep Human/Mouse/Rat Kit (llumina, San Diego, California, USA) was used for preparation of sequencing library with 1 μg of total RNA for each sample. Total RNA samples were treated with the Ribo-Zero rRNA Removal Kit (llumina, San Diego, California, USA) to deplete bacterial and eukaryotic ribosomal RNA (rRNA). First, Ribo-zero treated RNA was used to synthesise single-stranded cDNA and then second strand was synthesised using DNA Polymerase I and RNase H to produce double-stranded cDNA. Next, the cDNA was fragmented and the cDNA fragments were end repaired by addition of single "A" and then indexing adapters were ligated to each sample. The products were then purified and enriched using PCR with adapter universal primers to generate NGS libraries. Final prepared libraries were then quantified and checked for fragment size using Qubit High sensitivity DNA reagent (Qubit 2.0) followed by TapeStation D1000 ScreenTape (Agilent Technologies). The resulting NGS libraries were then sequenced using the NextSeq550 platform (llumina).

RNA-seq data curation and processing

From demultiplexed FASTQ files low-quality reads and adapter sequences were removed using Cutadapt. Trimmed files were then aligned using HISAT2 to the human reference genome (GRCh38) with rna-strandness set to RF. The aligned data was quantified using featureCounts and GENCODE human genome (GRCh38) GTF version 33 with -p and -s 2 option enabled. Differential expression analysis performed using DESeq2, genes having p adjusted < 0.05 and log2 fold change $<= -0.5849$, $>= +0.5849$ considered for further analysis. Pathway enrichment analysis was performed using the ClusterProfiler R package.

Public datasets downloaded from NCBI SRA for the search term "active tuberculosis" and "healthy control" using RNA expression by next generation sequencing and *Homo sapiens* filter terms [32,33]. The samples were processed using a similar analysis process except p adjusted <0.001 cut off was used, outliers were filtered based on normalised expression PCA and no filtering was done based on fold change values. The curated publicly available RNA-seq datasets used in representative **Fig 1A and 1B** are available in Tables A and B in **S3 Table**.

Computational and statistical analysis

Details of statistical tests can be found in figure legends and statistics for genomic analysis. Prism version 5 and 8.0.2 (Figs 3 and **S3**) were used for statistical calculations. The bar plot of fold changes in gene expression was generated using the GGPLOT2 R package, pairwise comparison and plotting of tuberculosis treatment data were done using the GGPUBR package. Heat maps were plotted using ComplexHeatmap package and hierarchical clustering was performed using the inbuilt clustering functions.

Supporting information

S1 Table. Differentially expressed genes from RNA-seq Data.
(XLSX)

S2 Table. Up- and down-regulated pathways from RNA-seq Data.
(XLSX)

S3 Table. Publicly available Metadata across TB subjects.
(XLSX)

S4 Table. Resources and primers.
(XLSX)

S1 Data. Numerical values for all datasets. Figs 1A–1C, 1E–1G, 2B–2C, 2E, 2G–2H, 2J–2M, 2O–2R, 3A–3K, 4A–4C, 4E–4F, 4H, 4J, 4L, 5A–5G, 5I, 5K, 5M, 5N, 6A, 6C–6J, 6L, 6M, **S1A–S1**B, **S2**A–**S2**B, **S2**E, **S2**G–**S2**H, **S2**J, **S2**L–**S2**N, **S2**O, **S4**C, **S4**E–**S4**F, **S4**H, **S5**B, **S5**F, **S5**H, **S5**J, **S5**, **S5**L, **S5**N, **S5**P, **S5**R, **S6**A–**S6**D, **S6**G, **S6**I, and **S6**J.
(XLSX)

S1 Raw Images. Uncropped western raw images. Figs 1F, 1G, 2A, 2I, 2N, 4D, 4G, 4I, 5A, 5B, 5D, 5E, 5H, 5J, 5L, 6B, 6H, 6K, **S4**D, **S4**F, **S5**A, **S5**E, **S5**M, **S5**K, **S5**O, and **S6**H.
(PDF)

S1 Fig. NCoR1 expression in PBMCs and murine cDC1 DCs. (A) RT-qPCR line graph showing the *NCOR1* transcript kinetics (2 h, 12 h, 24 h, and 48 h) in H37Rv infected human PBMCs ($n = 3$ independent biological repeats). (B) RT-qPCR line graph showing the *Ncor1* transcript kinetics (2 h, 12 h, and 24 h) upon *M. smegmatis* infection in cDC1 ($n = 3$ independent biological repeats). $^*p < 0.05$, $^*p < 0.01$, and $^{***}p < 0.001$ were considered significant. Data analysis was performed using one-way ANOVA with Tukey's statistical test. Where n represents independent biological replicates. The data underlying this figure are available in S4 Table and S1 Data.
(TIF)

S2 Fig. NCoR1 perturbation increases *Mycobacterium* burden in myeloid cells. (A) Bar plot depicting the *NCOR1* transcript expression at 2 h, 6 h, and 24 h of H37Rv infected control and NCoR1 KD human monocytic THP-1 differentiated macrophages ($n = 3$). (B) Scatter plot showing the *M. smegmatis* load in control and NCoR1 KD human monocytic THP-1 differentiated macrophages by CFU assay at 24 h post infection ($n = 4$). (C) Flow cytometry dot plot showing the percentage of *M. smegmatis* infected control and NCoR1 KD human monocytic THP-1 differentiated macrophages at 6 h post infection ($n = 3$). (D) Flow cytometry histograms showing MFI shifts for the *M. smegmatis* infection in control and NCoR1 KD human monocytic THP-1 differentiated macrophages at 6 h post infection ($n = 3$). (E) Bar plot showing the quantification of percent positive cells and MFI shifts for the *M. smegmatis* infected control and NCoR1 KD human monocytic THP-1 differentiated macrophages at 6 h post

infection ($n = 3$). (F) Flow cytometry plots showing the back gating strategies used in flow cytometry analysis. (G) Bar plot of shRNA3-mediated NCoR1 depletion shown by RT-qPCR ($n = 3$). (H) Scatter plot showing the H37Rv load in control and shRNA3-mediated NCoR1 KD human monocytic THP-1 differentiated macrophages by CFU assay at 24 h ($n = 6$). (I) Flow cytometry contour plot showing the phagocytosis rate of GFP-tagged *M. smegmatis* in control and NCoR1 KD human monocytic THP-1 differentiated macrophages at 10 min, 30 min, and 60 min post infection ($n = 3$). (J) Bar plot showing the quantification of phagocytosis rate of *M. smegmatis* in control and NCoR1 KD human monocytic THP-1 differentiated macrophages at 10 min, 30 min, and 60 min post infection ($n = 3$). (K, L) Microscopy images and bar plot showing the levels of H37Rv infection in control and shRNA3-mediated NCoR1 KD at 24 h post infection ($n = 3$). (M) PCR results showing genotyping of NCoR1$^{fl/fl}$ and NCoR1-^{MyeKO} mice. (N) RT-qPCR depicting transcript levels of NCoR1 in CD11c$^+$ cells compared to CD11c$^-$ fraction ($n = 2$ mice). (O) Scatter plot showing the *M. smegmatis* load in control and NCoR1 KD cDC1 by CFU assay at 6 h post infection ($n = 6$). (P) Microscopy images showing the levels of *M. smegmatis* infection in control and NCoR1 KD cDC1 at 6 h post infection ($n = 3$). $^*p < 0.05$, $^*p < 0.01$, and $^{***}p < 0.001$ using paired and unpaired two-tailed Student's t test. Where n represents independent biological replicates. The data underlying this figure are available in S4 Table and S1 Data.
(TIF)

S3 Fig. Gating strategies and cell numbers of myeloid and lymphoid cell types in lung and spleen. (A) Schematic outline depicting the in vivo experimental strategy for *Mtb* infection in mice. (B) Images showing the size of spleens isolated from NCoR1$^{fl/fl}$ and NCoR1^{MyeKO} mice at 21 days post H37Rv infection ($n = 5$ mice). (C) Flow cytometry plots showing the gating strategy used for identification of myeloid cell subtypes in the lung tissues of NCoR1$^{fl/fl}$ and NCoR1^{MyeKO} mice at day 21 post infection. (D) Bar plots depicting the myeloid cell numbers in the lung along with *Mtb* infected ones. (E) Flow cytometry plots showing the gating strategy used to analyse myeloid cell subtypes in the spleen tissues of NCoR1$^{fl/fl}$ and NCoR1^{MyeKO} mice at day 21 post infection. (F) Bar plots demonstrating the myeloid cell numbers in the spleen along with *Mtb* infected ones. (G) Flow cytometry plots showing the gating strategy used to analyse B and T cell subtypes in the splenic tissues of NCoR1$^{fl/fl}$ and NCoR1^{MyeKO} mice at day 21 post infection. (H) Bar plots showing the lymphoid cell numbers in the spleen. $^*p < 0.05$, $^*p < 0.01$, and $^{***}p < 0.001$ using unpaired two-tailed Student's t test. Where n represents the total number of used mice. The data underlying this figure are available in S1 Data.
(TIF)

S4 Fig. NCoR1 controls the autophagy induction in both human and murine myeloid cells upon *Mycobacterium* infection. (A) Flow cytometry contour plots showing the intracellular H37Rv bacterial load in control and NCoR1 KD human monocytic THP-1 differentiated macrophages, with and without bafilomycin treatment ($n = 3$). (B, C) Flow cytometry histograms showing the MFI shifts for the H37Rv infection in control and NCoR1 KD human monocytic THP-1 differentiated macrophages with and without treatment of bafilomycin, bar plots depicting the quantification of the same ($n = 3$). (D) Western blot image showing the NCoR1 and LC3-II:LC3-I protein levels in control and NCoR1 KD cDC1 at different time points upon H37Rv infection ($n = 3$). (E) Bar plot showing densitometric quantification for the NCoR1 and LC3-II:LC3-I levels in control and NCoR1 KD cDC1 at different time points upon H37Rv infection. All protein bands were normalised with β-actin housekeeping control ($n = 3$). (F) Western blot image and corresponding densitometric analysis demonstrating the LC3-II:LC3-I protein levels in control and NCoR1 KD THP-1 differentiated mo-mΦ upon H37Rv infection vs. uninfected ($n = 3$). (G, H). Confocal microscopy and corresponding bar plot

demonstrating the colocalization of H37Rv with LC3 protein in the BMDMs from NCoR1^{fl/fl} and NCoR1^{MyeKO} mice at 2 h and 24 h post infection ($n = 4$ mice). $^*p < 0.05$, $^*p < 0.01$, and $^{***}p < 0.001$ using paired and unpaired two-tailed Student's t test, where n represents independent biological replicates. The data underlying this figure are available in S1 Data. Western blot raw images can be found in S1 Raw Image.
(TIF)

S5 Fig. NCoR1 controls the mTOR-TFEB axis to regulate autophagy and lysosome biogenesis in myeloid cells. (A, B) Representative western blot image with corresponding densitometric analysis depicting the TFEB protein kinetics (2 h, 12 h, and 24 h) in the H37Rv infected cDC1. All protein bands were normalised with β-actin housekeeping control ($n = 3$). (C, D) Microscopy images showing the relative levels of NCoR1 and TFEB levels in CD11c+ and F4/80+ H37Rv-GFP infected lung tissue sections compared to uninfected C57BL/6 mice. (E, F) Western blot image and bar plot demonstrating the TFEB level in control and NCoR1 KD cDC1 at different time points upon H37Rv infection ($n = 3$). (G) Confocal microscopy showing NCoR1 and TFEB expression in H37Rv infected BMDMs generated from NCoR1^{MyeKO} and NCoR1^{fl/fl} mice ($n = 4$ mice). (H) Bar plot showing the quantification for NCoR1 and TFEB protein levels from confocal microscopy of H37Rv infected BMDMs generated from NCoR1^{MyeKO} and NCoR1^{fl/fl} mice ($n = 4$ mice). (I, J) Confocal microscopy images and bar plots showing the entrapment of H37Rv with LAMP1 protein in control and NCoR1 KD human monocytic THP1 differentiated macrophages at different time points ($n = 3$). (K) Western blot image showing the protein levels of NCoR1, TFEB, and LC3-II:LC3-I in starved and fed condition in control and NCoR1 KD human monocytic THP-1 differentiated macrophages ($n = 3$). (L) Bar plot showing densitometric quantification of NCoR1, TFEB, and LC3-II:LC3-I western bands in starved and fed condition in control and NCoR1 KD human monocytic THP-1 differentiated macrophages. All bands were normalised with β-actin as housekeeping control ($n = 3$). (M) Western blot image showing NCoR1 and LC3-II:LC3-I protein levels in control and NCoR1 KD human monocytic THP-1 differentiated macrophages treated with heat killed H37Rv at different time points ($n = 3$). (N) Bar plot depicting densitometric quantification of NCoR1 and LC3-II:LC3-I in control and NCoR1 KD human monocytic THP-1 differentiated macrophages treated with heat killed H37Rv at different time points. All bands were normalised with β-actin as housekeeping control ($n = 3$). (O) Western blot representative image depicting the p-mTOR, mTOR, and p-TFEB, TFEB levels in H37Rv infected control and NCoR1 KD human monocytic THP-1 differentiated macrophages at 2 h and 24 h post infection, with and without Torin1 treatment ($n = 3$). (P) Bar plot depicting the densitometric quantification of normalised p-mTOR and p-TFEB protein bands. The p-mTOR and p-TFEB levels were normalised first with their respective total protein levels and then with housekeeping control β-actin, with and without Torin1 ($n = 3$). (Q) FACS analysis demonstrating the MFI shifts for H37Rv infection in control and NCoR1 KD human monocytic THP-1 differentiated macrophages at 24 h of infection with and without treatment of rapamycin ($n = 3$). (R) Bar plot demonstrating the MFI shift quantification of H37Rv infection in control and NCoR1 KD human monocytic THP-1 differentiated macrophages at 24 h of infection with and without treatment of rapamycin ($n = 3$). $^*p < 0.05$, $^*p < 0.01$, and $^{***}p < 0.001$ using paired and unpaired two-tailed Student's t test. Where n represents independent biological replicates. The data underlying this figure are available in S1 Data. Western blot raw images can be found in S1 Raw Image.
(TIF)

S6 Fig. NCoR1 regulates mTOR activity by fine-tuning cellular ATP-AMPK level. (A) Pathway enrichment analysis showing the top pathways for the list of down-regulated genes found

in RNA-seq data of NCoR1 KD human monocytic THP-1 differentiated macrophages as compared to control cells at 24 h post H37Rv infection (n = 3). (B) Heat map depicting differentially expressed genes of oxidative phosphorylation in post-infected Control and NCoR1 KD cells (n = 3). (C) Bar graph showing the intracellular ATP level in control and NCoR1 KD human monocytic THP-1 differentiated macrophages upon *M. smegmatis* infection at 6 h time point with and without antimycin A treatment (n = 3). (D) Scatter plot demonstrating the *M. smegmatis* bacterial load in control and NCoR1 KD human monocytic THP-1 differentiated macrophages at 6 h time point by CFU assay with and without antimycin A treatment (n = 3). (E) Flow cytometry contour plots depicting the GFP-tagged *M. smegmatis* infection in control and NCoR1 KD human monocytic THP-1 differentiated macrophages at 6 h with and without antimycin A treatment (n = 3). (F) Flow cytometry histogram plots showing the MFI shifts for *M. smegmatis* infection load in control and NCoR1 KD human monocytic THP-1 differentiated macrophages at 6 h with and without antimycin A treatment (n = 3). (G) Bar plots depicting the quantitation of percent positive infected cells and corresponding MFI shifts in flow cytometry analysis of *M. smegmatis* infection in control and NCoR1 KD human monocytic THP-1 differentiated macrophages at 6 h with and without antimycin A treatment (n = 3). (H) Western blot representative image demonstrating the p-AMPKα, p-mTOR, TFEB, and LC3 protein levels in *M. smegmatis* infected control and NCoR1 KD human monocytic THP-1 differentiated macrophages with and without antimycin A treatment (n = 3). (I) Bar plots demonstrating the quantification of p-AMPKα, p-mTOR, TFEB, and LC3 western blot bands in *M. smegmatis* infected control and NCoR1 KD human monocytic THP-1 differentiated macrophages with and without antimycin A treatment. All the phosphorylated proteins were normalised with their totals first, followed by β-actin housekeeping control (n = 3). (J) Scatter plot showing percent viability upon antimycin A treatment by FACS at 6 h (n = 6). $p < 0.05$, *$p < 0.01$, and ***$p < 0.001$ using two-tailed paired Student's t test. Where n represents independent biological replicates. The data underlying this figure are available in S1 and S2 Tables and S1 Data. Western blot raw images can be found in S1 Raw Image. (TIF)

S7 Fig. Graphical abstract. "Created with BioRender.com."
(PDF)

Acknowledgments

Author Contributions

Conceptualization: Viplov Kumar Biswas, Kaushik Sen, Abdul Ahad, Arup Ghosh, Sunil Kumar Raghav.

Data curation: Arup Ghosh, Sunil Kumar Raghav.

Formal analysis: Viplov Kumar Biswas, Kaushik Sen, Abdul Ahad, Arup Ghosh.

Funding acquisition: Sunil Kumar Raghav.

Investigation: Viplov Kumar Biswas, Kaushik Sen, Abdul Ahad, Sunil Kumar Raghav.

Methodology: Viplov Kumar Biswas, Kaushik Sen, Abdul Ahad, Surbhi Verma, Rashmirekha Pati, Subhasish Prusty, Sourya Prakash Nayak, Sreeparna Podder, Dhiraj Kumar, Sunil Kumar Raghav.

Project administration: Sunil Kumar Raghav.

Resources: Sunil Kumar Raghav.

Software: Arup Ghosh.

Supervision: Bhawna Gupta, Sunil Kumar Raghav.

Validation: Viplov Kumar Biswas, Sunil Kumar Raghav.

Visualization: Kaushik Sen, Abdul Ahad, Arup Ghosh, Sunil Kumar Raghav.

Writing – original draft: Viplov Kumar Biswas, Abdul Ahad, Arup Ghosh, Bhawna Gupta, Sunil Kumar Raghav.

Writing – review & editing: Viplov Kumar Biswas, Kaushik Sen, Abdul Ahad, Arup Ghosh, Bhawna Gupta, Sunil Kumar Raghav.

References

1. Mihret A. The role of dendritic cells in Mycobacterium tuberculosis infection. Virulence. 2012; 3:654–659. https://doi.org/10.4161/viru.22586 PMID: 23154283

2. Weiss G, Schaible UE. Macrophage defense mechanisms against intracellular bacteria. Immunol Rev. 2015; 264:182–203. https://doi.org/10.1111/imr.12266 PMID: 25703560

3. Srivastava S, Ernst JD, Desvignes L. Beyond macrophages: the diversity of mononuclear cells in tuberculosis. Immunol Rev. 2014; 262:179–192. https://doi.org/10.1111/imr.12217 PMID: 25319335

4. McClean CM, Tobin DM. Macrophage form, function, and phenotype in mycobacterial infection: lessons from tuberculosis and other diseases. Pathog Dis. 2016;74. https://doi.org/10.1093/femspd/ftw068 PMID: 27402783

5. Liu CH, Liu H, Ge B. Innate immunity in tuberculosis: host defense vs pathogen evasion. Cell Mol Immunol. 2017; 14:963–975. https://doi.org/10.1038/cmi.2017.88 PMID: 28890547

6. Upadhyay S, Mittal E, Philips JA. Tuberculosis and the art of macrophage manipulation. Pathog Dis. 2018;76. https://doi.org/10.1093/femspd/fty037 PMID: 29762680

7. Pieters J, Gatfield J. Hijacking the host: survival of pathogenic mycobacteria inside macrophages. Trends Microbiol. 2002; 10:142–146. https://doi.org/10.1016/s0966-842x(02)02305-3 PMID: 11864824

8. Romagnoli A, Etna MP, Giacomini E, Pardini M, Remoli ME, Corazzari M, et al. ESX-1 dependent impairment of autophagic flux by Mycobacterium tuberculosis in human dendritic cells. Autophagy. 2012; 8:1357–1370. https://doi.org/10.4161/auto.20881 PMID: 22885411

9. Chandra P, Ghanwat S, Matta SK, et al. Mycobacterium tuberculosis Inhibits RAB7 Recruitment to Selectively Modulate Autophagy Flux in Macrophages. Sci Rep. 2015; 5:16320. https://doi.org/10.1038/srep16320 PMID: 26541268

10. Chandra P, Grigsby SJ, Philips JA. Immune evasion and provocation by Mycobacterium tuberculosis. Nat Rev Microbiol. 2022; 20:750–766. https://doi.org/10.1038/s41579-022-00763-4 PMID: 35879556

11. Cohen SB, Gern BH, Delahaye JL. Alveolar Macrophages Provide an Early Mycobacterium tuberculosis Niche and Initiate Dissemination. Cell Host Microbe. 2018; 24(439–446):e4. https://doi.org/10.1016/j.chom.2018.08.001 PMID: 30146391

12. Zhao E, Czaja MJ. Transcription factor EB: a central regulator of both the autophagosome and lysosome. Hepatology. 2012; 55:1632–1634. https://doi.org/10.1002/hep.25619 PMID: 22517549

13. Czaja MJ. Functions of autophagy in hepatic and pancreatic physiology and disease. Gastroenterology. 2011; 140:1895–1908. https://doi.org/10.1053/j.gastro.2011.04.038 PMID: 21530520

14. Florey O, Overholtzer M. Macropinocytosis and autophagy crosstalk in nutrient scavenging. Philos Trans R Soc Lond B Biol Sci. 2019; 374:20180154. https://doi.org/10.1098/rstb.2018.0154 PMID: 30967004

15. Hardie DG, Ross FA, Hawley SA. AMPK: a nutrient and energy sensor that maintains energy homeostasis. Nat Rev Mol Cell Biol. 2012; 13:251–262. https://doi.org/10.1038/nrm3311 PMID: 22436748

16. Garcia D, Shaw RJ. AMPK: Mechanisms of Cellular Energy Sensing and Restoration of Metabolic Balance. Mol Cell. 2017; 66:789–800. https://doi.org/10.1016/j.molcel.2017.05.032 PMID: 28622524

17. Russell RC, Yuan HX, Guan KL. Autophagy regulation by nutrient signaling. Cell Res. 2014; 24:42–57. https://doi.org/10.1038/cr.2013.166 PMID: 24343578

18. Yan Q, Han C, Wang G. Activation of AMPK/mTORC1-Mediated Autophagy by Metformin Reverses Clk1 Deficiency-Sensitized Dopaminergic Neuronal Death. Mol Pharmacol. 2017; 92:640–652. https://doi.org/10.1124/mol.117.109512 PMID: 29025968

19. Kim YC, Guan KL. mTOR: a pharmacologic target for autophagy regulation. J Clin Invest. 2015; 125:25–32. https://doi.org/10.1172/JCI73939 PMID: 25654547

20. Settembre C, Di Malta C, Polito VA. TFEB links autophagy to lysosomal biogenesis. Science. 2011; 332:1429–1433. https://doi.org/10.1126/science.1204592 PMID: 21617040

21. Martina JA, Chen Y, Gucek M, Puertollano R. MTORC1 functions as a transcriptional regulator of autophagy by preventing nuclear transport of TFEB. Autophagy. 2012; 8:903–914. https://doi.org/10.4161/auto.19653 PMID: 22576015

22. Roczniak-Ferguson A, Petit CS, Froehlich F. The transcription factor TFEB links mTORC1 signaling to transcriptional control of lysosome homeostasis. Sci Signal. 2012; 5:ra42. https://doi.org/10.1126/scisignal.2002790 PMID: 22692423

23. Qi X, Man SM, Malireddi RK. Cathepsin B modulates lysosomal biogenesis and host defense against Francisella novicida infection. J Exp Med. 2016; 213:2081–2097. https://doi.org/10.1084/jem.20151938 PMID: 27551156

24. Mottis A, Mouchiroud L, Auwerx J. Emerging roles of the corepressors NCoR1 and SMRT in homeostasis. Genes Dev. 2013; 27:819–835. https://doi.org/10.1101/gad.214023.113 PMID: 23630073

25. Perissi V, Jepsen K, Glass CK, Rosenfeld MG. Deconstructing repression: evolving models of corepressor action. Nat Rev Genet. 2010; 11:109–123. https://doi.org/10.1038/nrg2736 PMID: 20084085

26. Yamamoto H, Williams EG, Mouchiroud L. NCoR1 is a conserved physiological modulator of muscle mass and oxidative function. Cell. 2011; 147:827–839. https://doi.org/10.1016/j.cell.2011.10.017 PMID: 22078881

27. Saito T, Kuma A, Sugiura Y. Autophagy regulates lipid metabolism through selective turnover of NCoR1. Nat Commun. 2019; 10:1567. https://doi.org/10.1038/s41467-019-08829-3 PMID: 30952864

28. Lima TI, Valentim RR, Araujo HN, Oliveira AG, Favero BC, Menezes ES, et al. Role of NCoR1 in mitochondrial function and energy metabolism. Cell Biol Int. 2018; 42:734–741. https://doi.org/10.1002/cbin.10973 PMID: 29660213

29. Ou-Yang Q, Lin XM, Zhu YJ. Distinct role of nuclear receptor corepressor 1 regulated de novo fatty acids synthesis in liver regeneration and hepatocarcinogenesis in mice. Hepatology. 2018; 67:1071–1087. https://doi.org/10.1002/hep.29562 PMID: 28960380

30. Sen K, Pati R, Jha A. NCoR1 controls immune tolerance in conventional dendritic cells by fine-tuning glycolysis and fatty acid oxidation. Redox Biol. 2023; 59:102575. https://doi.org/10.1016/j.redox.2022.102575 PMID: 36565644

31. Koster S, Upadhyay S, Chandra P. Mycobacterium tuberculosis is protected from NADPH oxidase and LC3-associated phagocytosis by the LCP protein CpsA. Proc Natl Acad Sci U S A. 2017; 114:E8711–E8720. https://doi.org/10.1073/pnas.1707792114 PMID: 28973896

32. Bouquet J, Soloski MJ, Swei A. Longitudinal Transcriptome Analysis Reveals a Sustained Differential Gene Expression Signature in Patients Treated for Acute Lyme Disease. mBio. 2016; 7:e00100–e00116. https://doi.org/10.1128/mBio.00100-16 PMID: 26873097

33. Leong S, Zhao Y, Ribeiro-Rodrigues R. Cross-validation of existing signatures and derivation of a novel 29-gene transcriptomic signature predictive of progression to TB in a Brazilian cohort of household

contacts of pulmonary TB. Tuberculosis (Edinb). 2020; 120:101898. https://doi.org/10.1016/j.tube.2020.101898 PMID: 32090859

34. Sambarey A, Devaprasad A, Mohan A. Unbiased Identification of Blood-based Biomarkers for Pulmonary Tuberculosis by Modeling and Mining Molecular Interaction Networks. EBioMedicine. 2017; 15:112–126. https://doi.org/10.1016/j.ebiom.2016.12.009 PMID: 28065665

35. Kalam H, Fontana MF, Kumar D. Alternate splicing of transcripts shape macrophage response to Mycobacterium tuberculosis infection. PLoS Pathog. 2017; 13:e1006236. https://doi.org/10.1371/journal.ppat.1006236 PMID: 28257432

36. Blischak JD, Tailleux L, Mitrano A. Mycobacterial infection induces a specific human innate immune response. Sci Rep. 2015; 5:16882. https://doi.org/10.1038/srep16882 PMID: 26586179

37. Cadena AM, Flynn JL, Fortune SM. The Importance of First Impressions: Early Events in Mycobacterium tuberculosis Infection Influence Outcome. mBio. 2016; 7:e00342–e00316. https://doi.org/10.1128/mBio.00342-16 PMID: 27048801

38. von Both U, Berk M, Agapow PM. Mycobacterium tuberculosis Exploits a Molecular Off Switch of the Immune System for Intracellular Survival. Sci Rep. 2018; 8:661. https://doi.org/10.1038/s41598-017-18528-y PMID: 29330469

39. Fuertes Marraco SA, Grosjean F, Duval A. Novel murine dendritic cell lines: a powerful auxiliary tool for dendritic cell research. Front Immunol. 2012; 3:331. https://doi.org/10.3389/fimmu.2012.00331 PMID: 23162549

40. Ahad A, Stevanin M, Smita S. NCoR1: Putting the Brakes on the Dendritic Cell Immune Tolerance. iScience. 2019; 19:996–1011. https://doi.org/10.1016/j.isci.2019.08.024 PMID: 31522122

41. Smita S, Ahad A, Ghosh A. Importance of EMT Factor ZEB1 in cDC1 "MutuDC Line" Mediated Induction of Th1 Immune Response. Front Immunol. 2018; 9:2604. https://doi.org/10.3389/fimmu.2018.02604 PMID: 30483264

42. Volpe E, Cappelli G, Grassi M. Gene expression profiling of human macrophages at late time of infection with Mycobacterium tuberculosis. Immunology. 2006; 118:449–460. https://doi.org/10.1111/j.1365-2567.2006.02378.x PMID: 16895554

43. Bonilla DL, Bhattacharya A, Sha Y. Autophagy regulates phagocytosis by modulating the expression of scavenger receptors. Immunity. 2013; 39:537–547. https://doi.org/10.1016/j.immuni.2013.08.026 PMID: 24035364

44. Petruccioli E, Petrone L, Vanini V. IFNgamma/TNFalpha specific-cells and effector memory phenotype associate with active tuberculosis. J Infect. 2013; 66:475–486.

45. Guler R, Parihar SP, Spohn G. Blocking IL-1alpha but not IL-1beta increases susceptibility to chronic Mycobacterium tuberculosis infection in mice. Vaccine. 2011; 29:1339–1346.

46. Nair S, Huynh JP, Lampropoulou V. Irg1 expression in myeloid cells prevents immunopathology during M. tuberculosis infection. J Exp Med. 2018; 215:1035–1045. https://doi.org/10.1084/jem.20180118 PMID: 29511063

47. Azzam KM, Madenspacher JH, Cain DW. Irgm1 coordinately regulates autoimmunity and host defense at select mucosal surfaces. JCI Insight. 2017;2. https://doi.org/10.1172/jci.insight.91914 PMID: 28814662

48. Netea-Maier RT, Plantinga TS, van de Veerdonk FL. Modulation of inflammation by autophagy: Consequences for human disease. Autophagy. 2016; 12:245–260. https://doi.org/10.1080/15548627.2015.1071759 PMID: 26222012

49. Cadwell K. Crosstalk between autophagy and inflammatory signalling pathways: balancing defence and homeostasis. Nat Rev Immunol. 2016; 16:661–675. https://doi.org/10.1038/nri.2016.100 PMID: 27694913

50. Gutierrez MG, Master SS, Singh SB, Taylor GA, Colombo MI, Deretic V. Autophagy is a defense mechanism inhibiting BCG and Mycobacterium tuberculosis survival in infected macrophages. Cell. 2004; 119:753–766. https://doi.org/10.1016/j.cell.2004.11.038 PMID: 15607973

51. Kovoor P, Mathew M, Abraham T, Taneja PK. Enteric fever complicated by myocarditis, hepatitis and shock. J Assoc Physicians India. 1988; 36:353. PMID: 3182706

52. Sachdeva K, Goel M, Sudhakar M. Mycobacterium tuberculosis (Mtb) lipid mediated lysosomal rewiring in infected macrophages modulates intracellular Mtb trafficking and survival. J Biol Chem. 2020; 295:9192–9210. https://doi.org/10.1074/jbc.RA120.012809 PMID: 32424041

53. He WS, Dai XF, Jin M. Hypoxia-induced autophagy confers resistance of breast cancer cells to ionizing radiation. Oncol Res. 2012; 20:251–258. https://doi.org/10.3727/096504013x13589503483012 PMID: 23581232

54. Chang CJ, Lin JF, Hsiao CY. Lutein Induces Autophagy via Beclin-1 Upregulation in IEC-6 Rat Intestinal Epithelial Cells. Am J Chin Med. 2017; 45:1273–1291. https://doi.org/10.1142/S0192415X17500707 PMID: 28893091

55. Brady OA, Martina JA, Puertollano R. Emerging roles for TFEB in the immune response and inflammation. Autophagy. 2018; 14:181–189. https://doi.org/10.1080/15548627.2017.1313943 PMID: 28738171

56. Franco-Juarez B, Coronel-Cruz C, Hernandez-Ochoa B. TFEB; Beyond Its Role as an Autophagy and Lysosomes Regulator. Cells. 2022, 11.

57. Palmieri M, Impey S, Kang H. Characterization of the CLEAR network reveals an integrated control of cellular clearance pathways. Hum Mol Genet. 2011; 20:3852–3866. https://doi.org/10.1093/hmg/ddr306 PMID: 21752829

58. Settembre C, Zoncu R, Medina DL. A lysosome-to-nucleus signalling mechanism senses and regulates the lysosome via mTOR and TFEB. EMBO J. 2012; 31:1095–1108. https://doi.org/10.1038/emboj.2012.32 PMID: 22343943

59. Pena-Llopis S, Vega-Rubin-de-Celis S, Schwartz JC. Regulation of TFEB and V-ATPases by mTORC1. EMBO J. 2011; 30:3242–3258. https://doi.org/10.1038/emboj.2011.257 PMID: 21804531

60. Singh P, Subbian S. Harnessing the mTOR Pathway for Tuberculosis Treatment. Front Microbiol. 2018; 9:70. https://doi.org/10.3389/fmicb.2018.00070 PMID: 29441052

61. Bolourian A, Mojtahedi Z. Obesity and COVID-19: The mTOR pathway as a possible culprit. Obes Rev. 2020; 21:e13084. https://doi.org/10.1111/obr.13084 PMID: 32578354

62. Yeh HS, Yong J. mTOR-coordinated Post-Transcriptional Gene Regulations: from Fundamental to Pathogenic Insights. J Lipid Atheroscler. 2020; 9:8–22. https://doi.org/10.12997/jla.2020.9.1.8 PMID: 32821719

63. Puente C, Hendrickson RC, Jiang X. Nutrient-regulated Phosphorylation of ATG13 Inhibits Starvation-induced Autophagy. J Biol Chem. 2016; 291:6026–6035. https://doi.org/10.1074/jbc.M115.689646 PMID: 26801615

64. Gwinn DM, Shackelford DB, Egan DF. AMPK phosphorylation of raptor mediates a metabolic checkpoint. Mol Cell. 2008; 30:214–226. https://doi.org/10.1016/j.molcel.2008.03.003 PMID: 18439900

65. Alenghat T, Meyers K, Mullican SE. Nuclear receptor corepressor and histone deacetylase 3 govern circadian metabolic physiology. Nature. 2008; 456:997–1000. https://doi.org/10.1038/nature07541 PMID: 19037247

66. Etna MP, Sinigaglia A, Grassi A. Mycobacterium tuberculosis-induced miR-155 subverts autophagy by targeting ATG3 in human dendritic cells. PLoS Pathog. 2018; 14:e1006790. https://doi.org/10.1371/journal.ppat.1006790 PMID: 29300789

67. Li P, Spann NJ, Kaikkonen MU. NCoR repression of LXRs restricts macrophage biosynthesis of insulin-sensitizing omega 3 fatty acids. Cell. 2013; 155:200–214. https://doi.org/10.1016/j.cell.2013.08.054 PMID: 24074869

68. Khan N, Pahari S, Vidyarthi A. Stimulation through CD40 and TLR-4 Is an Effective Host Directed Therapy against Mycobacterium tuberculosis. Front Immunol. 2016; 7:386. https://doi.org/10.3389/fimmu.2016.00386 PMID: 27729911

69. Ganley IG, Lam du H, Wang J. ULK1.ATG13.FIP200 complex mediates mTOR signaling and is essential for autophagy. J Biol Chem. 2009; 284:12297–12305. https://doi.org/10.1074/jbc.M900573200 PMID: 19258318

70. Frudd K, Burgoyne T, Burgoyne JR. Oxidation of Atg3 and Atg7 mediates inhibition of autophagy. Nat Commun. 2018; 9:95. https://doi.org/10.1038/s41467-017-02352-z PMID: 29311554

71. Walczak M, Martens S. Dissecting the role of the Atg12-Atg5-Atg16 complex during autophagosome formation. Autophagy. 2013; 9:424–425. https://doi.org/10.4161/auto.22931 PMID: 23321721

72. Canaday DH, Beigi R, Silver RF. ATP and control of intracellular growth of mycobacteria by T cells. Infect Immun. 2002; 70:6456–6459. https://doi.org/10.1128/IAI.70.11.6456-6459.2002 PMID: 12379727

73. Kusner DJ, Barton JA. ATP stimulates human macrophages to kill intracellular virulent Mycobacterium tuberculosis via calcium-dependent phagosome-lysosome fusion. J Immunol. 2001; 167:3308–3315. https://doi.org/10.4049/jimmunol.167.6.3308 PMID: 11544319

74. Akela AK, Kumar A. Bioenergetic Heterogeneity in Mycobacterium tuberculosis Residing in Different Subcellular Niches. mBio. 2021; 12:e0108821. https://doi.org/10.1128/mBio.01088-21 PMID: 34060333

75. Brunton J, Steele S, Ziehr B. Feeding uninvited guests: mTOR and AMPK set the table for intracellular pathogens. PLoS Pathog. 2013; 9:e1003552. https://doi.org/10.1371/journal.ppat.1003552 PMID: 24098109

76. Yang CS, Kim JJ, Lee HM. The AMPK-PPARGC1A pathway is required for antimicrobial host defense through activation of autophagy. Autophagy. 2014; 10:785–802. https://doi.org/10.4161/auto.28072 PMID: 24598403

77. Meijer AJ, Codogno P. Autophagy: regulation by energy sensing. Curr Biol. 2011; 21:R227–R229. https://doi.org/10.1016/j.cub.2011.02.007 PMID: 21419990

78. Ahad A, Smita S, Mishra GP. NCoR1 fine-tunes type-I IFN response in cDC1 dendritic cells by directly regulating Myd88-IRF7 axis under TLR9. Eur J Immunol. 2020; 50:1959–1975. https://doi.org/10.1002/eji.202048566 PMID: 32644192

79. Davie SA, Maglione JE, Manner CK. Effects of FVB/NJ and C57Bl/6J strain backgrounds on mammary tumor phenotype in inducible nitric oxide synthase deficient mice. Transgenic Res. 2007; 16:193–201. https://doi.org/10.1007/s11248-006-9056-9 PMID: 17206489

80. Szade A, Nowak WN, Szade K. Effect of crossing C57BL/6 and FVB mouse strains on basal cytokine expression. Mediat Inflamm. 2015; 2015:762419. https://doi.org/10.1155/2015/762419 PMID: 25834307

81. Nemeth J, Olson GS, Rothchild AC. Contained Mycobacterium tuberculosis infection induces concomitant and heterologous protection. PLoS Pathog. 2020; 16:e1008655. https://doi.org/10.1371/journal.ppat.1008655 PMID: 32673357

82. Schneider BE, Korbel D, Hagens K. A role for IL-18 in protective immunity against Mycobacterium tuberculosis. Eur J Immunol. 2010; 40:396–405. https://doi.org/10.1002/eji.200939583 PMID: 19950174

83. Rothchild AC, Stowell B, Goyal G. Role of Granulocyte-Macrophage Colony-Stimulating Factor Production by T Cells during Mycobacterium tuberculosis Infection. mBio. 2017:8.

84. Peters W, Scott HM, Chambers HF. Chemokine receptor 2 serves an early and essential role in resistance to Mycobacterium tuberculosis. Proc Natl Acad Sci U S A. 2001; 98:7958–7963. https://doi.org/10.1073/pnas.131207398 PMID: 11438742

85. Andersson AM, Andersson B, Lorell C. Autophagy induction targeting mTORC1 enhances Mycobacterium tuberculosis replication in HIV co-infected human macrophages. Sci Rep. 2016; 6:28171. https://doi.org/10.1038/srep28171 PMID: 27302320

NCoR1 controls immune tolerance in conventional dendritic cells by fine-tuning glycolysis and fatty acid oxidation

Kaushik Sen [a,b], Rashmirekha Pati [a], Atimukta Jha [a], Gyan Prakash Mishra [a,c], Subhasish Prusty [a,b], Shweta Chaudhary [d], Swati Swetalika [a], Sreeparna Podder [a,c], Aishwarya Sen [a,b], Mamuni Swain [a], Ranjan Kumar Nanda [d], Sunil K. Raghav [a,b,*]

[a] Institute of Life Sciences (ILS), Bhubaneswar, Odisha, 751023, India
[b] Regional Centre for Biotechnology, Faridabad, Haryana, 121001, India
[c] Kalinga Institute of Industrial Technology, Bhubaneswar, Odisha, 751024, India
[d] Translational Health Group, International Centre for Genetic Engineering and Biotechnology (ICGEB), New Delhi, 110067, India

ARTICLE INFO

ABSTRACT

Dendritic cells (DCs) undergo rapid metabolic reprogramming to generate signal-specific immune responses. The fine control of cellular metabolism underlying DC immune tolerance remains elusive. We have recently reported that NCoR1 ablation generates immune-tolerant DCs through enhanced IL-10, IL-27 and SOCS3 expression. In this study, we did comprehensive metabolic profiling of these tolerogenic DCs and identified that they meet their energy requirements through enhanced glycolysis and oxidative phosphorylation (OXPHOS), supported by fatty acid oxidation-driven oxygen consumption. In addition, the reduced pyruvate and glutamine oxidation with a broken TCA cycle maintains the tolerogenic state of the cells. Mechanistically, the AKT-mTOR–HIF–1α-axis mediated glycolysis and CPT1a-driven β-oxidation were enhanced in these tolerogenic DCs. To confirm these observations, we used synthetic metabolic inhibitors and found that the combined inhibition of HIF-1α and CPT1a using KC7F2 and etomoxir, respectively, compromised the overall transcriptional signature of immunological tolerance including the regulatory cytokines IL-10 and IL-27. Functionally, treatment of tolerogenic DCs with dual KC7F2 and etomoxir treatment perturbed the polarization of co-cultured naïve CD4+ T helper (Th) cells towards Th1 than Tregs, *ex vivo* and *in vivo*. Physiologically, the *Mycobacterium tuberculosis (Mtb)* infection model depicted significantly reduced bacterial burden in BMcDC1 *ex vivo* and in CD103+ lung DCs in *Mtb* infected NCoR1[DC−/−]mice. The spleen of these infected animals also showed increased Th1-mediated responses in the inhibitor-treated group. These findings suggested strong involvement of NCoR1 in immune tolerance. Our validation in primary human monocyte-derived DCs (moDCs) showed diminished NCOR1 expression in dexamethasone-derived tolerogenic moDCs along with suppression of CD4+T cell proliferation and Th1 polarization. Furthermore, the combined KC7F2 and etomoxir treatment rescued the decreased T cell proliferative capacity and the Th1 phenotype. Overall, for the first time, we demonstrated here that NCoR1 mediated control of glycolysis and fatty acid oxidation fine-tunes immune tolerance versus inflammation balance in murine and human DCs.

1. Introduction

The process of DC activation and cytokine production is highly co-ordinated. Activation also necessitates significant energy needs by undergoing rapid metabolic reprogramming events. Metabolic reprogramming processes in addition to signalling cascades, transcription factors, and co-regulators, play pivotal roles in fine-tuning the

balance between inflammation and tolerance [1]. DCs differentiated with either GM-CSF or FLT3 show differential metabolic adaptations upon TLR specific activation [2]. Among which, early and late activation profiles are also distinct. Under steady-state conditions, OXPHOS dominates in DCs, reducing power being generated primarily by fatty acid oxidation (FAO) and the glutaminolysis-driven TCA cycle [1,3–6]. These steady state adaptations are regulated by the AMP/ATP sensor AMPK and maintain the metabolic homeostasis of the cell. Early activation of

Abbreviations

BMDCs	Bone marrow derived dendritic cells
DCs	Dendritic cells
Dex	Dexamethasone
DEGs	Differentially expressed genes
ECAR	Extracellular acidification rate
ETC	Electron transport chain
FAO	Fatty acid oxidation
mtDNA	Mitochondrial DNA
NCoR1	Nuclear receptor co-repressor 1
moDCs	Monocyte derived dendritic cells
Mtb	*Mycobacterium tuberculosis*
OXPHOS	Oxidative phosphorylation
OCR	Oxygen consumption rate
ROS	Reactive oxygen species
TLR9	Toll-like receptor 9
TMRM	Tetramethylrhodamine, methyl ester

immunogenic DCs upon TLR engagement alters the metabolic profile to glycolytic with stable OXPHOS. Such metabolic energy needs in inflammatory DCs are primarily controlled via the kinases TBK1, IKKε, and HK2 [7] whereas, sustained activation leads to decreased OXPHOS and a dominant glycolytic profile mediated by the mTOR/HIF-1α axis [8,9]. These events are crucial regarding DC migration, up-regulation of co-stimulatory or inhibitory molecules and secretion of cytokines. Such evidence is also being drawn from the 2-DG inhibitor studies [10–12]. Another important aspect of DC biology is to prevent hyperactivation and auto-immune diseases by inducing immune-tolerance. Tolerogenic DCs assist in overcoming such conditions by secreting increased levels of IL-10, IL-27, and TGF-β cytokines resulting in increased frequency of Treg induction than Th1 cells [13,14]. These DCs are conventionally attained by Vitamin D3 (VD3), and Dexamethasone (Dex), either individually or in combination. Whereas antigen presenting cell (APC) mediated Treg induction is obtained by IL-10, retinaldehyde dehydrogenase (RALDH), and indoleamine 2,3-dioxygenase (IDO-1) [15,16].

Metabolism in tolerized DCs is governed by increased OXPHOS, FAO and glycolytic capacity [17–23]. However, the transcriptional and molecular cues underpinning such metabolic activities that generates tolerance in DCs is still lacking. Also, metabolic events impacted by such a transcriptional network are unexplored. Global co-regulators such as nuclear receptor co-repressor 1 (NCoR1) and silencing mediator of retinoic acid and thyroid hormone receptor (SMRT) are well characterized for their metabolic functions. They're recognized to be important in maintaining homeostasis and regulating systemic metabolic processes [24,25]. Among these, NCoR1 has diverse metabolic roles in muscle cells and adipocytes [26,27]. The preferential implication of NCoR1 is also being established in energy metabolism with respect to autophagy and atherosclerosis [28–30]. In the context of regulation of inflammatory versus tolerogenic immune response, our earlier functional and epigenomics studies on type I conventional DCs have demonstrated that NCoR1 depletion polarizes DCs towards tolerance that in turn shifts the balance of naïve CD4$^+$ co-cultured T cells towards Tregs [31,32]. However, the metabolic adjustments of these tolerogenic DCs is largely unknown, hence, in this study we focused to understand the control of various metabolic pathways required to maintain a fine balance of inflammation and tolerance in pursuit of energy metabolism in both murine and human DCs.

In this study, we performed comprehensive molecular and metabolic characterization of NCoR1 depleted immune-tolerant DCs *in-vitro* (CD8α$^+$ DC line) and *ex vivo* (bone marrow-derived dendritic cells from NCoR1$^{DC-/-}$ mice). DCs were activated by ligating TLR9 using unmethylated CpG (CPG-B) as an immunological stimulant. Characteristic

pathways specific for energy metabolism were profiled by employing extracellular flux assays, transcriptome analysis and T cell polarization. In addition, primary human DCs and *Mtb* infection model substantiated the key metabolic adaptations required to fine-tune immunogenic versus tolerogenic balance.

2. Results

2.1. NCoR1 depleted tolerogenic DCs depicted enhanced glycolysis and OXPHOS

To decipher the metabolic adaptations controlled by NCoR1 leading to strong immune-tolerant state in conventional Type-I DCs (cDC1), we have used a stable *Ncor1* gene knock-down (KD) cDC1 mutu-DC line where the mean *Ncor1* gene KD efficiency of ~80% at transcript level was confirmed by RT-qPCR (Fig. S1A). We have already confirmed in details the tolerogenic phenotype of NCoR1 depleted cDC1 in our earlier studies [31]. Now to investigate the real-time metabolic changes of these NCoR1 depleted and control cDC1 in unstimulated (Uns) and CpG challenged conditions, extracellular flux assays were performed using Seahorse flux analyzer. The CpG challenged NCoR1 deficient tolerogenic DCs demonstrated significantly enhanced glycolysis and glycolytic capacity (Fig. 1A and Fig. S1B). Along with it, increased extracellular lactate build-up and decreased pH complemented the same (Fig. 1B and Fig. S1C). Furthermore, glycolytic ATP determined with and without 2-DG (2-Deoxy-D-glucose) also showed a similar pattern (Fig. S1D). To further confirm this phenotype, we looked into the transcript expression of the key characteristic glycolytic genes in the RNAseq data and found that genes like *Pkm, Pfkp, Pfkfb3, Hk2,* and *Ldhal6b* were upregulated in the NCoR1 KD CpG condition compared to control (Fig. 1C). In addition, metabolic pathways such as "Respiratory electron transport" and "Pyruvate metabolism" were top enriched pathways in the differentially expressed genes (DEGs) of 6h CpG activated NCoR1 depleted DCs (Fig. 1D). Following which we also performed RT-qPCR and specifically examined the relative mRNA expression of glucose transporter *Slc2a1* and rate-limiting enzymes like *Hk2* and *Pkm2*, along with *Ldha.* The mRNA levels were found to be significantly higher in stimulated NCoR1 KD DCs compared to controls (Fig. 1E). Increased expression of the glut transporter 1 and rate-limiting enzymes confirmed enhanced glucose uptake and its metabolization through the glycolytic pathway. At the metabolite level, quantitation by Gas chromatography-mass spectrometry (GC-MS) depicted significantly increased levels of pyruvic acid, lactic acid, and alanine reassuring similar bioenergetic profiles (Fig. 1F). Increased lactic acid and alanine hint towards a decreased TCA cycle activity and acetyl Co-A conversion [33]. Furthermore, NCoR1 ChIPseq data depicted that the rate limiting glycolytic genes such as *Pfkb* and *Pfkfb3* are directly bound and regulated by NCoR1 in control Uns and 6h CpG condition (Fig. 1G). This implies that when the co-repressor is removed, *Pfk's* gene expression increases and thus glycolysis. Next, we focussed on a major parallel pathway of glycolysis called pentose phosphate pathway (PPP) since it is important for regulating redox homeostasis and biosynthesis. We first checked the transcript level expression (log2 FC) of the oxidative and non-oxidative PPP genes in our RNAseq data and found them to be downregulated except Glucose 6 phosphate dehydrogenase 2 (*G6pd2*), an important rate-limiting enzyme of PPP, although not significant (Fig. S1E). Further to confirm, we analysed the protein level expression of G6PD, and found it to be profoundly reduced (Fig. S1F) supporting that PPP might not be playing a pivotal role in metabolizing Glucose 6-phosphate. Therefore, the above results confirmed enhanced glycolysis to be a distinctive feature of NCoR1 depleted immune-tolerant DCs upon CpG stimulation.

We then investigated the OXPHOS levels, since a fine-balance of glycolysis and OXPHOS in response to activation are reported to be important for inflammation and immune-tolerance. Tolerogenic DCs are known to exhibit higher levels of OXPHOS [18,34]. To decipher the OXPHOS levels in control and NCoR1 KD DCs, first we checked the
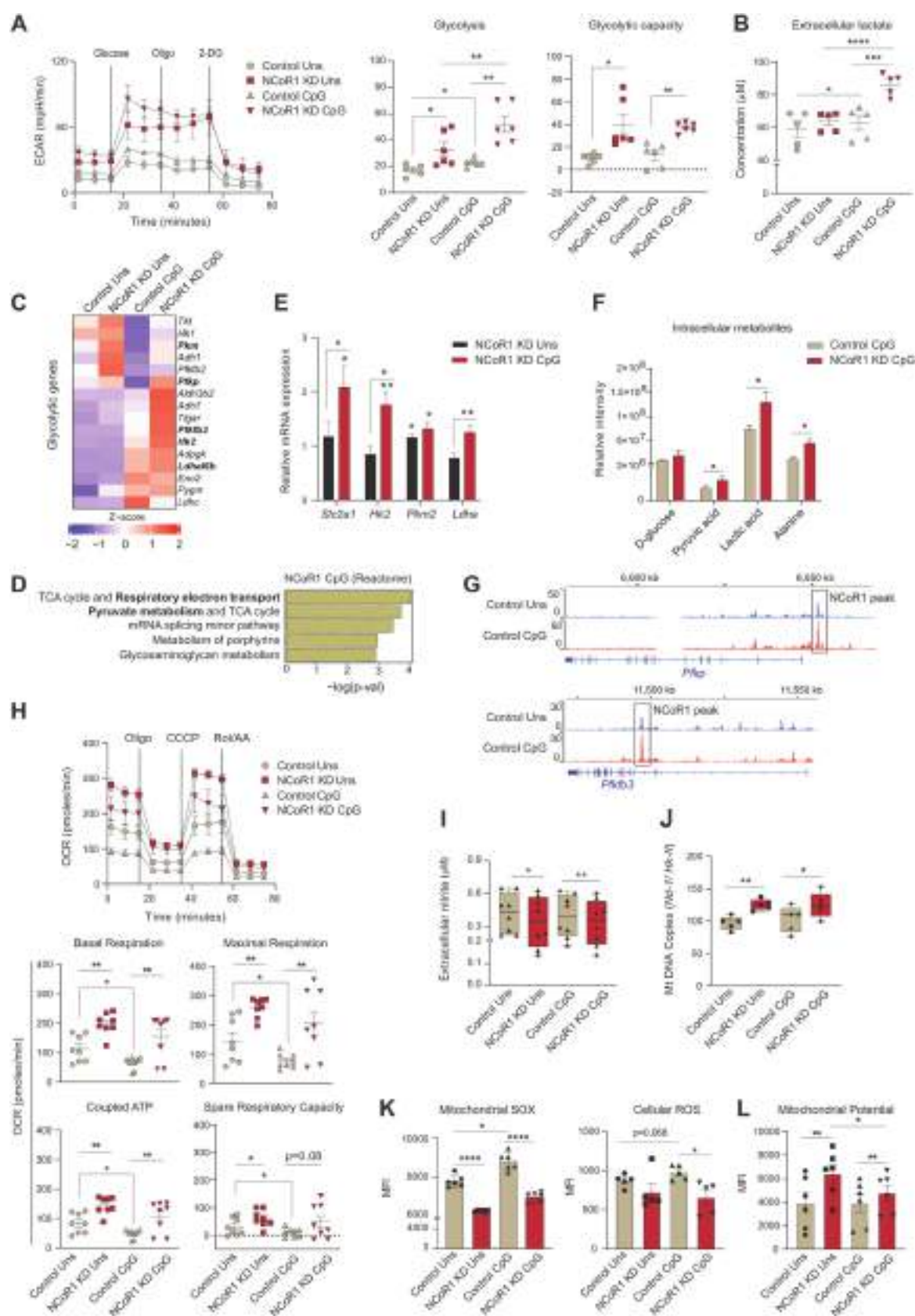
(caption on next page)

Fig. 1. NCoR1 depleted tolerogenic cDC1 DCs depicted enhanced glycolysis and OXPHOS as compared to control cells

A. Representative line graph and scatter plots showing the glyco-stress parameters (glycolysis and glycolytic capacity) in unstimulated and 6h CpG activated control and NCoR1 depleted tolerogenic DCs, as measured using Seahorse extracellular flux analyzer. (n = 6)

B. Scatter plot depicting the extracellular lactate accumulation in the culture supernatants of unstimulated and 6h CpG activated control and NCoR1 depleted tolerogenic DCs at a dilution of 1:10. (n = 5)

C. Heatmap showing the differentially expressed genes (DEGs) enriched for the glycolytic pathway. RNAseq of unstimulated and 6h CpG activated NCoR1 KD as compared to control DCs were used to determine the DEGs. (n = 2)

D. Bar graphs depicting the top enriched metabolic pathways from the DEGs in NCoR1 KD CpG activated tolerogenic DCs as compared to controls, using Reactome Pathway Database. (n = 2)

E. RT-qPCR analysis showing the relative transcript expression of glut transporter *Slc2a1,* and glycolytic genes *Hk2, Pkm2* and *Ldha* in unstimulated and 6h CpG activated NCoR1 KD tolerogenic DCs. (n = 5–7)

F. Bar graphs demonstrating the relative intensities of intracellular metabolites of NCoR1 KD CpG activated DCs as compared to controls as quantified using GC-MS. (n = 3)

G. IGV snapshots showing the ChIPseq binding of NCoR1 at the *Pfkp* and *Pfkfb3* gene loci in unstimulated and 6h CpG stimulated control DCs.

H. Representative line graph and scatter plots showing the mito-stress parameters (basal respiration, maximal respiration, coupled ATP and spare respiratory capacity) in unstimulated and 6h CpG activated control and NCoR1 depleted tolerogenic DCs as measured using an extracellular flux analyzer. (n = 8)

I. Box and whisker plots showing the min-max values for extracellular nitrite in the culture supernatant collected from unstimulated and 6h CpG activated control and NCoR1 depleted tolerogenic DCs. (n = 8)

J. Box and whisker plots depicting the min-max values for mitochondrial DNA copies (*Nd-1/Hk-II*) quantified by RT-qPCR in unstimulated and 6h CpG activated control and NCoR1 KD DCs. (n = 5)

K. Bar graphs with dots depicting the MFI levels of mitochondrial SOX, (n = 6) and cellular ROS, (n = 5) in unstimulated and 6h CpG stimulated control and NCoR1 KD DCs as quantified from flow cytometry.

L. Bar graphs with dots showing the MFI levels of TMRM measured for mitochondrial potential estimation in unstimulated and 6h CpG activated control and NCoR1 KD DCs. (n = 6)

*p ≤ 0.05, **p ≤ 0.01, ***p ≤0.001 and ****p ≤0.0001. p-value has been calculated using two tailed paired student's t-test. Data shown in figure is combined from 3 independent experiments [A] and from 4 independent experiments [H]. Error bars represent SEM, except I and J, horizontal lines depicting mean.

expression of genes belonging to complex I–V of the electron transport chain (ETC) using RNAseq data. The ETC genes were enriched for the NCoR1 ablated DCs both in Uns and CpG condition (Fig. S1G). Further, transcript expressions of the nuclear respiratory factor-1 (*Nrf-1*) and Complex-IV gene *Cox5a* were found to behave in a similar manner (Fig. S1H). Moreover, oxygen consumption rate (OCR) with regard to basal respiration, maximal respiration, coupled ATP, and spare respiratory capacity were found to be significantly higher in NCoR1 KD cells both in Uns and CpG conditions with respect to controls. The activated states depicted significantly lowered OCR levels in control and a decreasing trend in NCoR1 KD DCs (Fig. 1H and Fig. S1I). This suggested an inclination of stimulated NCoR1 KD cells towards glycolysis for energy requirement. Also, the coupled ATP from OXPHOS differed from the total intracellular ATP levels, which points towards the direct generation of ATP from glycolysis (Fig. S1J). To substantiate the preceding assertion regarding OXPHOS, we measured the extracellular nitrite levels. Nitrite and nitrate, stable end products of Nitric Oxide (NO), impact mitochondrial respiration inversely [35,36]. Since NCoR1 KD cells showed higher mitochondrial respiration, their extracellular nitrite levels were found to be significantly lower (Fig. 1I). Other important parameters like mitochondrial DNA (mtDNA) copy number can also facilitate OXPHOS proportionately [37]. Therefore, mtDNA copy numbers were determined taking the ratio of *Nd-1/Hk-II* (mitochondrial/nuclear) [38]. NCoR1 KD cells had significantly more mtDNA copies and gave a plausible explanation for the enhanced mitochondrial respiratory parameters (Fig. 1J). Besides nitrite and mtDNA copy numbers, pivotal aspects impacting respiratory levels are mitochondrial potential and reactive oxygen species. Mitochondrial SOX and cellular ROS levels were estimated and found to be significantly reduced in CpG-stimulated NCoR1 KD tolerant DCs (Fig. 1K and Fig. S1K), distinctive features of inflammatory DCs. On the other side, increased TMRM (Tetramethylrhodamine, methyl ester) levels in NCoR1 KD DCs showed enhanced mitochondrial potential, supporting elevated OXPHOS (Fig. 1L and Fig. S1L). The median levels for Mitochondrial SOX, cellular ROS and TMRM were determined by flow cytometry and uniform gating strategies were used (Fig. S1M). Overall, the tolerogenic NCoR1 KD DCs exhibited, although not significantly, higher OXPHOS levels in Uns condition than in CpG. In comparison to control cells, the levels were elevated and significant. The relative increase in OXPHOS in NCoR1 depleted DCs hinted towards increased bioenergetic pathways

fuelling the electron transport chain (ETC). This also suggested that regulation of stimulation-dependent tolerogenic cytokine secretion is an integral part of metabolic pathways.

2.2. FLT3L differentiated primary BMDCs from NCoR1^(DC−/−) mice depicted similar bioenergetics as mutu-cDC1 line

We further confirmed the glycolytic and mitochondrial bioenergetic parameters observed in the mutu-cDC1 line in primary BMDCs generated from NCoR1^(DC−/−) mice. First genotyping was performed to confirm homozygous NCoR1^(DC−/−) progenies (Fig. S2A). In addition, the NCoR1 ablation in BMDCs was confirmed by RT-qPCR with respect to control CD11c-Cre BMDCs (Fig. S2B). Furthermore, cellular homeostasis of FLT3L differentiated DCs at day 9 (CD11c^+MHCII^+) in NCoR1^(DC−/−) and CD11c-Cre control mice were confirmed by flow cytometry (Fig. S2C). No disparity in percentage of DC numbers were observed between the NCoR1^(DC−/−) and CD11c-Cre control mice. Unlike the DC line, extracellular bioenergetic parameters in BMDCs were determined at Uns and CpG 18h, since a prolonged and sustained activation was required for primary DCs to generate effective immune responses [39,40]. Real-time metabolic changes pertaining to glycolysis and glycolytic capacity were significantly increased in NCoR1^(DC−/−) BMDCs upon stimulation (Fig. 2A). Extracellular lactate levels also complemented the enhanced glycolytic levels (Fig. 2B). The relative mRNA expression of the glucose transporter *Slc2a1* and rate-limiting enzymes like *Hk2* and *Pkm2,* along with *Ldha* were elevated as in the DC line and confirmed the enhanced glycolytic rate in NCoR1^(DC−/−) BMDCs at CpG 18h (Fig. 2C). Further, mitochondrial energy parameters like basal respiration, maximal respiration, and spare respiratory capacity also showed a similar trend in NCoR1^(DC−/−) and control CD11c-Cre BMDCs as observed in the DC line (Fig. 2D). Parameters regulating mitochondrial respiration and inflammation like cellular ROS were found to be significantly decreased in the NCoR1^(DC−/−) BMcDC1s (Fig. 2E and Fig. S2D). Whereas TMRM mediated mitochondrial potential was high in both Uns and 18h CpG stimulation (Fig. 2F and Fig. S2E). Uniform gating strategies were used for depicting the median levels of cellular ROS and TMRM in BMcDC1s (Fig. S2F). Overall, the tolerogenic NCoR1^(DC−/−) BMDCs displayed similar bioenergetic profiles as mutu-cDC1 line both in Uns and CpG activated conditions.
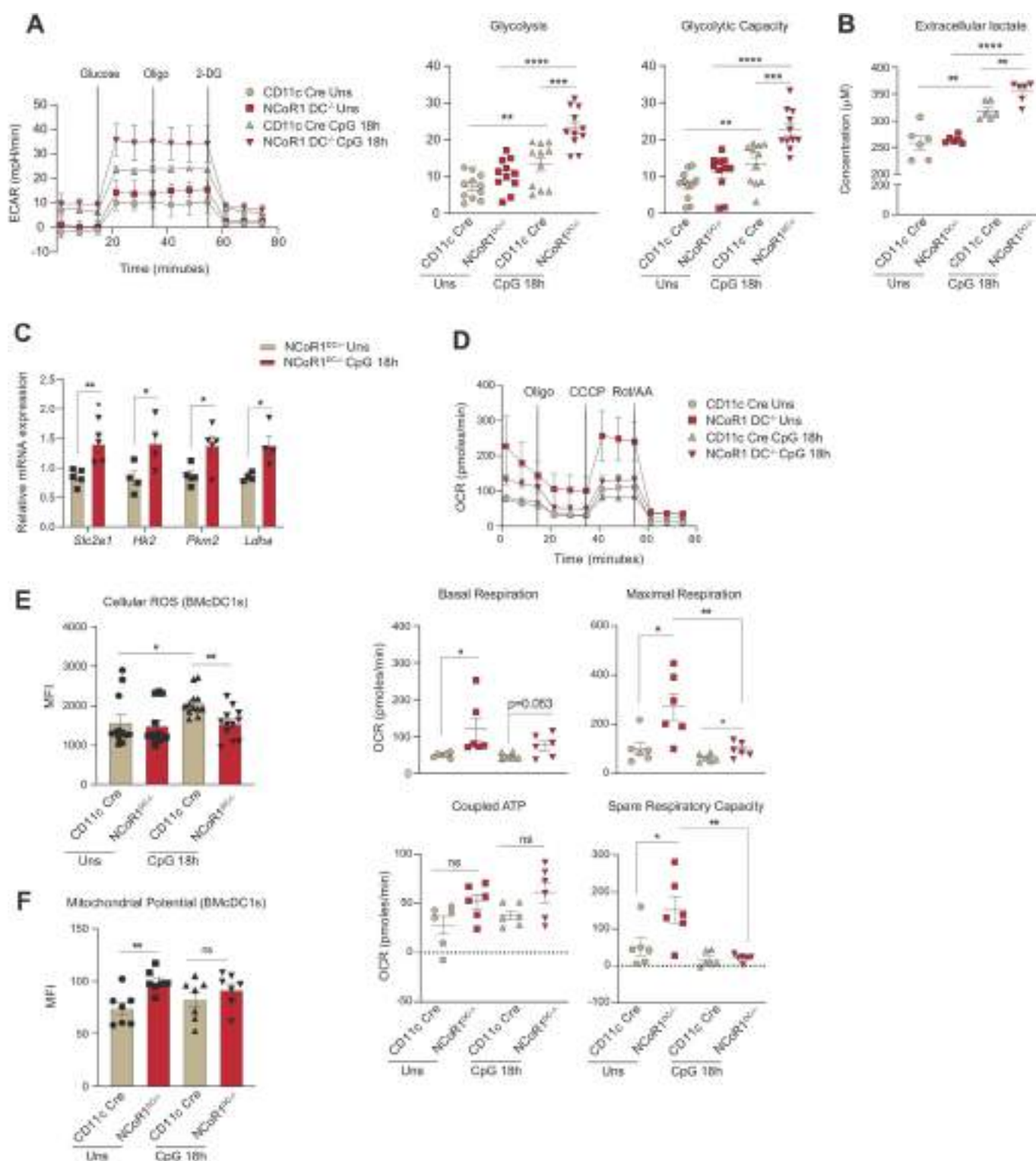
(caption on next page)

2.3. AKT/mTOR induced HIF-1α expression regulates glycolysis and secretion of tolerogenic cytokines

To gain insight into how NCoR1 depletion in cDC1 impacted glycolytic metabolic reprogramming, we assessed the signalling events crucial for DC metabolic responses. The TBK1/IKK/AKT/HK-II axis and the AMPK versus mTOR/HIF-1α pathway is known to regulate early and late

glycolytic induction in DCs, respectively [7,41,42]. We focussed on 6h CpG activated control and NCoR1 KD cDC1 and thus considered the late glycolytic induction signalling cascade. NCoR1 depleted 6h CpG challenged cDC1 depicted enhanced phosphorylated levels of AKT and mTORC1 in western blotting (Fig. 3A). Increased levels of AKT and mTORC1 in concert essentially stabilised the HIF-1α expression (Fig. 3A), responsible for the upregulation of glucose transporters like

Fig. 2. FLT3L differentiated primary BMDCs from NCoR1$^{DC-/-}$ mice showed enhanced glycolysis and OXPHOS as observed in mutu-cDC1 line

A. Representative line graph and scatter plots showing the glyco-stress parameters (glycolysis and glycolytic capacity) in unstimulated and 18h CpG activated control CD11c-Cre and NCoR1 ablated FLT3 differentiated BMDCs on day 9, measured using Seahorse extracellular flux analyzer. (n = 11)

B. Scatter plot depicting the levels of extracellular lactate accumulated in the culture supernatants of control CD11c-Cre and NCoR1$^{DC-/-}$ BMDCs before and after 18h CpG activation, at a dilution of 1:5. (n = 6)

C. Bar graphs showing the relative transcript expression of glucose transporter *Slc2a1,* and glycolytic genes*, Hk2, Pkm2* and *Ldha* in unstimulated and 18h CpG activated CD11c-Cre and NCoR1$^{DC-/-}$ BMDCs. (n = 4–5)

D. Representative line graph and scatter plots showing the mito-stress parameters (basal respiration, maximal respiration, coupled ATP and spare respiratory capacity) in unstimulated and 18h CpG activated control CD11c-Cre and NCoR1$^{DC-/-}$ BMDCs on day 9 as measured using Seahorse extracellular flux analyzer. (n = 6)

E. Bar graphs with dots depicting the MFI levels of cellular ROS in unstimulated and 18h CpG activated CD11c-Cre control and NCoR1$^{DC-/-}$ BMcDC1s on day 9 as measured in F4/80$^-$CD11c$^+$CD24$^+$ gated cells using flow cytometry. (n = 12)

F. Bar graphs with dots showing the MFI levels of mitochondrial potential upon TMRM staining in CD11c-Cre control and NCoR1$^{DC-/-}$ BMcDC1s on day 9 before and after 18h CpG stimulation as measured in F4/80$^-$CD11c$^+$CD24$^+$ gated cells using flow cytometry. (n = 7)

*p ≤ 0.05, **p ≤ 0.01, ***p ≤0.001 and ****p ≤0.0001. p-value has been calculated using two tailed unpaired student's t-test. Data shown in figure is combined from 4 independent experiments [A] and from 3 independent experiments [D]. Error bars represent SEM.

Slc2a1 and glycolytic enzymes like PFK, PKM2, LDHa, etc. [43–45]. The relative mRNA expression of the *Hif-1α* gene was also significantly upregulated (Fig. 3B). The above findings imply that in CpG challenged NCoR1-deficient DCs, a signal transduction circuit including AKT-mTORC1-HIF-1α axis coordinated increased glycolysis. From RNAseq data, we found that DEGs of the HIF-1α pathway genes were significantly upregulated upon CpG stimulation in NCoR1 KD cells (Fig. 3C). Mechanistically, ChIPseq data revealed direct NCoR1 binding peaks at the distal regions of the *Hif-1α* gene body, exhibiting direct regulation of *Hif-1α* expression by NCoR1 (Fig. 3D). Further, to confirm how mTORC1 and HIF-1α modulates glycolytic function, extracellular acidification rate (ECAR) was measured after treatments with mTOR inhibitor rapamycin and the HIF-1α inhibitor KC7F2. We performed cell viability assay at the concentrations of rapamycin and KC7F2 used for experiments and more than 90% viability was observed (Fig. S3A). We observed that control and NCoR1 KD DCs responded differentially upon inhibitor treatments. For confirmation of the potent dysregulation of the HIF-1α molecule upon KC7F2 treatment, we also performed RT-qPCR and looked into the transcript level expression of *Hif-1α* in both control and NCoR1 KD DCs upon stimulation with CpG for 6 h (Fig. S3B). Glycolysis and glycolytic capacity levels were significantly impaired in CpG stimulated NCoR1 depleted cells with respect to controls. Moreover, KC7F2 inhibition depicted robust perturbation of ECAR levels in comparison to rapamycin, which suggested a strong dependence of NCoR1 KD cells on HIF-1α signalling axis for enhanced glycolytic function (Fig. 3E). Further, to know how rapamycin and KC7F2 treatments impacted the balance between tolerance and inflammation, we determined the levels of tolerogenic cytokines like IL-10 and IL-27 along with inflammatory ones like IL-6 and IL-12p40/70 by flow cytometry. We found a significant reduction in the percent positive cells as well as in MFI shifts for tolerogenic cytokines upon KC7F2 treatment in NCoR1 KD condition (Fig. 3F and Fig. S3C). No noticeable changes were observed in the expression of inflammatory cytokines, whereas control cells depicted a significant reduction in MFI levels of IL-12p40/70 upon KC7F2 treatment (Fig. S3D). Overall, the results confirmed an essential role of HIF-1α in regulating glycolysis and its importance in inducing immune-tolerance in NCoR1 KD DCs.

2.4. Reduced pyruvate and glutamine oxidation facilitates immune tolerance

Pyruvate oxidation, glutaminolysis and FAO replenish the TCA cycle and generate reducing powers to be used in the ETC for OXPHOS [46]. To decipher how active OXPHOS levels were maintained in NCoR1 depleted cells under CpG activation, we did a comprehensive characterization of the aforementioned pathways and its impact on tolerance. As noted earlier, the enhanced ECAR facilitated lactic acid and alanine production and hinted towards the non-incorporation of pyruvate into the mitochondrial tricarboxylic acid (TCA) cycle. Reduced pyruvate dehydrogenase (PDH) expression at the protein level in NCoR1 KD cDC1

confirmed the same (Fig. 4A). Furthermore, pyruvate and glutamine oxidation measured after using mitochondrial pyruvate carrier (MPC-1) inhibitor UK-5099 along with BPTES, the glutaminase1 (GLS1) inhibitor and etomoxir that inhibits carnitine palmitoyltransferase 1 (CPT1a), we found a significant reduction in percent dependencies of NCoR1 depleted cells on these pathways (Fig. 4B and Fig. S3E). Further, the DEGs of the TCA cycle pertaining to pyruvate oxidation like *Pdhb* showed reduced expression (Fig. 4C). In addition**,** transcript levels of the sequential enzymes of TCA cycle from citrate to isocitrate (*Aco2*), isocitrate to α-ketoglutarate (*Idh2/3a/3b/3g*), α-ketoglutarate to succinate (*Ogdh/Ogdhl*) and succinate to fumarate (*Sdha/b*) were also found to be decreased (Fig. 4C). The above data gave us an insight into the broken TCA cycle being operated in the NCoR1 KD cells. Functionally, to know the balance between tolerance and inflammation, flow cytometry was used to determine the secretory levels of tolerogenic and inflammatory cytokines upon treatment with UK-5099, BPTES and glutamine analogue DON. No significant changes in the cell viability were observed upon treatment with these inhibitors (Fig. S3F). In addition, further reduction in pyruvate and glutamine oxidation significantly increased IL-10 levels both in control and NCoR1 depleted DCs (Fig. 4D and Fig. S3G). On the other hand, decreased IL-12p40/70 percent positive cells were obtained for both control and NCoR1 KD cells upon UK-5099 treatment (Fig. S3H). BPTES and DON impacted the MFI shifts of IL-6 and IL-12p40/70 insignificantly (Fig. S3H). Taken together, the aforesaid findings suggested that lowered levels of pyruvate and glutamine oxidation play crucial roles in maintaining immune tolerance in NCoR1 depleted DCs. Interestingly, potent disruption of glutaminolysis and pyruvate oxidation render control DCs towards tolerance.

2.5. Active OXPHOS driven by FAO regulates immune tolerance in NCoR1 KD DCs

The above results indicate that the active state of OXPHOS in NCoR1 depleted DCs is driven by pathways other than pyruvate and glutamine oxidation. We speculated β-oxidation of fatty acids might facilitate the same. We found that at 6h CpG activation, oxygen consumption mediated FAO using etomoxir resulted in a significantly higher FAO index in NCoR1 KD DCs (Fig. 4E and Fig. S3I). The relative mRNA expression of the rate-limiting FAO gene *Cpt1a* was also found to be significantly elevated (Fig. 4F). In accordance with the FAO index, DEGs pertaining to β-oxidation pathways showed enhanced expression of genes like *Pex7, Acoxl, Acadl, Phyh, Acsl1, Adipor1, Por, and Acaa1a* in RNAseq data of CpG stimulated NCoR1 KD DCs (Fig. 4G). Since unstimulated NCoR1 depleted DCs showed higher OXPHOS compared to stimulated DCs, we could speculate that the pattern of gene expression with regard to β-oxidation behaved similarly (Fig. 4G). Functionally, modulation of immune response cytokines upon inhibition of β-oxidation pathway using etomoxir were also analyzed. Etomoxir did not hamper the cell viability levels (Fig. S3J). Etomoxir treatment showed significant reduction in the secretory levels of tolerogenic cytokines IL-10 and IL-27
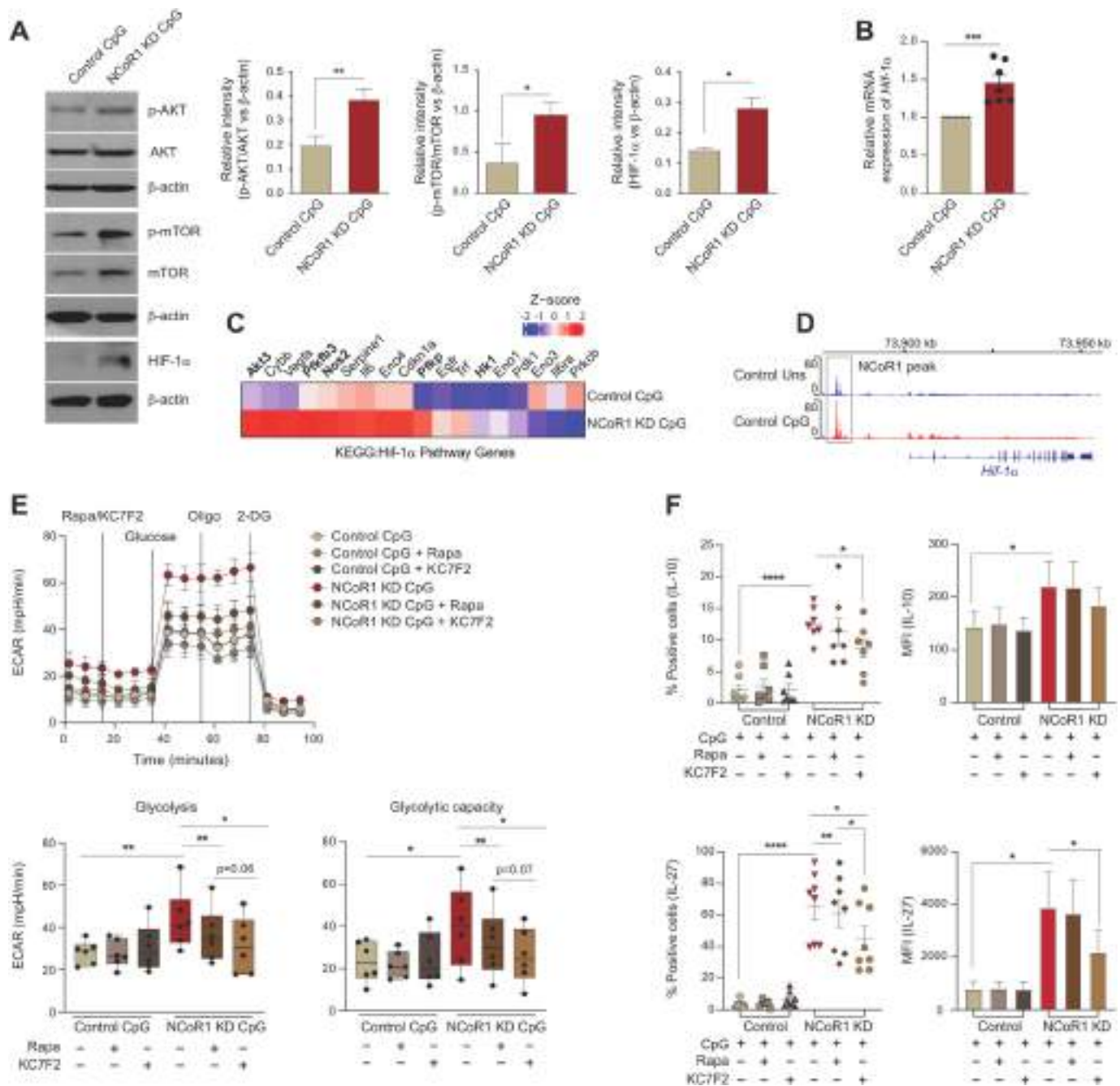
Fig. 3. AKT-mTOR–HIF–1α axis in regulating glycolysis and tolerogenic cytokine production in NCoR1 depleted DCs

A. Representative western blots showing the phosphorylated and total protein levels of AKT, mTOR and HIF-1α in control and NCoR1 depleted DCs after 6h CpG stimulation. Ratios of phosphorylated to total protein levels were further normalized to the housekeeping control β-actin. Corresponding bar plots depicted the densitometry analysis of the western blots. (n = 3–4)

B. Bar graph with dots showing the relative mRNA expression of *Hif-1α* in 6h CpG activated control and NCoR1 depleted tolerogenic DCs. (n = 7)

C. Heatmap showing the differentially expressed genes of HIF-1α pathway observed in the RNAseq data of control and NCoR1 KD 6h CpG stimulated DCs. (n = 3)

D. IGV snapshot depicting the NCoR1 binding at the distal genomic regions of *Hif-1α* gene loci in unstimulated and 6h CpG activated control DCs.

E. Line graph and box and whisker plots with dots depicting the levels of ECAR along with glycolysis and glycolytic capacity respectively upon pre-injection with either rapamycin (20nM) or KC7F2 (10μM) in control and NCoR1 KD DCs after 6h CpG activation, as measured using Seahorse extracellular flux analyzer. (n = 6)

F. Scatter plots (percent positive cells) and bar graphs (MFI) showing the cytokine levels of IL-10 and IL-27 upon treatment with rapamycin (20nM) and KC7F2 (10μM) in CpG activated control and NCoR1 depleted tolerogenic DCs. (n = 7–8)

*p ≤ 0.05, **p ≤ 0.01, ***p ≤0.001 and ****p ≤0.0001. p-value has been calculated using two tailed paired student's t-test. Error bars represent SEM.

(Fig. 4H and Fig. S3K), while inflammatory cytokines IL-12p40/70 and IL-6 remain unchanged in NCoR1 depleted condition (Fig. S3L). Next, we asked how fatty acid oxidation is being facilitated in NCoR1 KD DCs? It is known that β-oxidation in cells is aided by *de novo* fatty acid synthesis (FAS) via citrate, intracellular fatty acid reserves and exogenous fatty acid imports via CD36 [47–49]. Moreover, *de novo* FAS via citrate is characteristic of immunogenic DCs [7]. Although, NCoR1 depleted DCs produced more of citric acid (Oxaloacetic acid generated from anaplerotic reaction of aspartic acid and acetyl Co-A from β-oxidation), but its sequential conversion to produce free FAs and its re-entry into
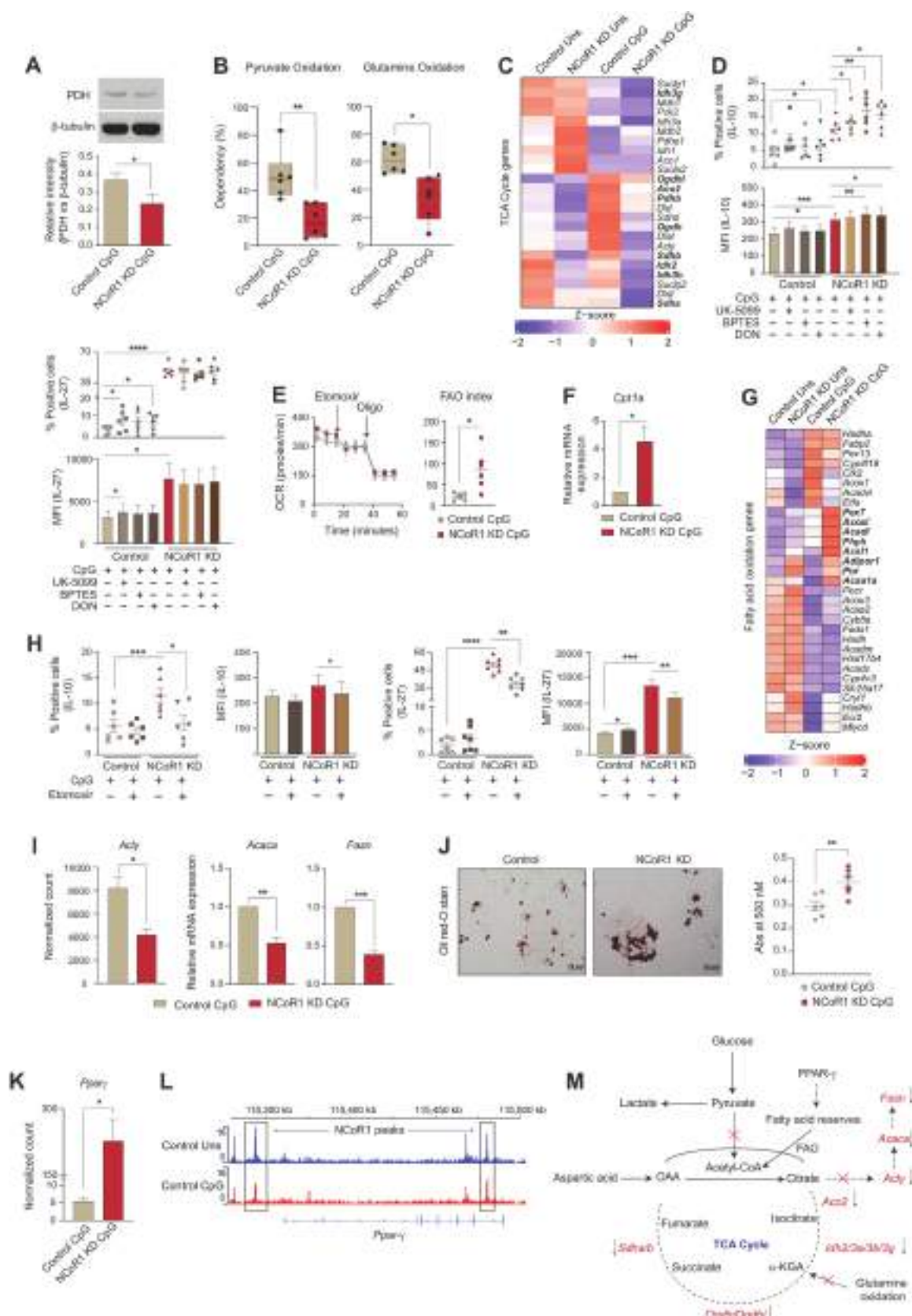
(caption on next page)

Fig. 4. Mitochondrial fuel/flux (Pyruvate oxidation, Glutamine oxidation and FAO) characteristics regulates tolerogenicity in NCoR1 depleted DCs

A. Representative Western blot showing the protein level expression of pyruvate dehydrogenase (PDH) in control and NCoR1 depleted tolerogenic DCs after 6h CpG activation. The protein level was normalized to the housekeeping control β-tubulin. Corresponding bar graph depicted the densitometric analysis of the Western blot bands. (n = 4)

B. Plots demonstrating the percent dependencies of 6h CpG activated control and NCoR1 depleted DCs on pyruvate [(first injection- UK-5099-2μM and second a combination of etomoxir (4μM)+BPTES (3μM) together] and glutamine oxidation [first injection - BPTES (3μM) and second a combination of UK-5099 (2μM) + etomoxir (4μM) together], measured from an extracellular flux analyzer. (n = 6)

C. Heatmap showing the differentially expressed genes of TCA cycle observed in the RNAseq of unstimulated and 6h CpG activated control and NCoR1 depleted tolerogenic DCs. (n = 2)

D. Scatter plots (percent positive cells) and bar graphs (MFI) demonstrating the cytokine levels of IL-10 and IL-27 upon treatment with UK-5099 (5μM), BPTES (5μM) and DON (5μM) in control and NCoR1 depleted tolerogenic DCs after 6h CpG stimulation. (n = 6)

E. Line graph and scatter plot showing the FAO index in control and NCoR1 KD DCs after 6h CPG activation upon treatment with etomoxir (50μM) and Oligomycin (2μM), as measured using Seahorse Extracellular flux analyzer. (n = 6)

F. Bar graph depicting the relative mRNA expression of *Cpt1a* in 6h CpG activated control and NCoR1 depleted tolerogenic DCs quantified using RT-qPCR. (n = 3)

G. Heatmap showing the differentially expressed genes of FAO pathway in control and NCoR1 depleted DCs before and after 6h CpG activation using RNAseq data. (n = 2)

H. Scatter plots (percent positive cells) and bar graphs (MFI) showing the cytokine levels of IL-10 and IL-27 upon treatment with etomoxir (50μM) in 6h CpG activated control and NCoR1 depleted DCs. (n = 6–7)

I. Bar plots showing the normalized counts for *Acly* from RNAseq data and relative mRNA expression of *Acaca* and *Fasn* using RT-qPCR in 6h CpG stimulated control and NCoR1 KD DCs. (n = 3 for *Acly* and n = 5 for *Acaca* and *Fasn*)

J. Representative microscopic images showing the Oil red-O stained neutral lipids in the control and NCoR1 KD DCs after 6h CpG activation. Corresponding dot plot depicted the quantification of the oil-red-O stain using absorbance at 500nm. (n = 6)

K. Bar plot showing the normalized counts for *Ppar-γ* in the RNAseq data of 6h CpG activated control and NCoR1 depleted tolerogenic DCs. (n = 3)

L. IGV snapshot showing the direct binding of NCoR1 at *Ppar-γ* gene loci in cDC1 before and after 6h CpG activation.

M. Schematic illustration showing the non-incorporation of pyruvate into the TCA cycle, accumulation of citrate, reduced expression of TCA cycle genes and decreased glutamine oxidation in 6h CpG activated NCoR1 KD DCs.

*p ≤ 0.05, **p ≤ 0.01, ***p ≤0.001 and ****p ≤0.0001. p-value has been calculated using two tailed paired student's t-test. Data shown in figure is combined from 3 independent experiments [B]. Error bars represent SEM. . (For interpretation of the references to colour in this figure legend, the reader is referred to the Web version of this article.)

---

mitochondria through CPT1a to undergo oxidation was hampered due to decreased expression of *Acly, Acaca* and *Fasn* (Fig. 4I and Fig. S3M). Moreover, reduced *Cd36* normalized expression further opposed the notion of extracellular FA import (Fig. S3N). However, oil-red-O staining exhibited more neutral lipid deposits in NCoR1 depleted cells, suggesting the role of intracellular fatty acid reserves in mediating β-oxidation [28] (Fig. 4J). At the same time, lipid storage and fatty acid biosynthesis require NADPH to supply reducing equivalents. As we showed above that the PPP is downregulated in NCoR1 depleted DCs, we also looked into the ME1 and IDH1 related pathways. Since, G6PD decrease results in NADP production, which induces compensatory increases in IDH1 and ME1 [50,51]. Pyruvate shuttle into malate for converting into oxaloacetate might be one of the crucial routes for TCA cycle replenishment and NADP$^+$ production or decarboxylation of malate into pyruvate for effective NADPH production for fatty acid synthesis. For this, we looked into the metabolite levels of Malic acid in our cellular metabolite analysis data of Mass Spec and found its levels to be profoundly higher in the NCoR1 depleted DC line (Fig. S3O), suggesting that active enzyme activity of Me1 appears to be involved in fatty acid biosynthesis or lipid storage in NCoR1 depleted DCs. Further, *Idh1* transcript levels didn't show any significant changes upon stimulation (Fig. S3P).

Now, the obvious question was how FAO is being regulated? Several reports have suggested that there is a direct role of PPARs in regulating mitochondrial β-oxidation [52,53]. From the RNAseq data we found an enhanced *Ppar-γ* expression in NCoR1 DCs (Fig. 4K). At the same time ChIPseq depicted direct binding of NCoR1 at *Ppar-γ* in *cis*-regulatory regions suggesting its direct control by NCoR1 (Fig. 4L). Possibly a feed-forward loop is generated through mTORC1 and PPAR-γ to facilitate FAO in CpG activated NCoR1 KD DCs [54]. Though this requires further work for its confirmation. Overall, the metabolic state of NCoR1 KD DCs demonstrated accumulation of citrate, lowered expression of TCA cycle genes and enhanced FAO index along with reduced pyruvate and glutamine oxidation (Fig. 4M). Thus, tolerogenic immune responses generated in NCoR1 ablated DCs are majorly contributed by CPT1a mediated β-oxidation along with HIF-1α driven glycolysis.

2.6. Dual inhibition of HIF-1α and FAO tweaked immune-tolerance to inflammation in NCoR1 depleted tolerogenic DCs

Individual inhibitions of HIF-1α-induced glycolysis and CPT1a-mediated FAO inhibited the levels of tolerogenic cytokines. It showed the importance of HIF-1α and CPT1a mediated metabolic changes in the modulation of tolerogenic response genes in NCoR1 KD DCs. Furthermore, to acquire potent inhibition of tolerance, we performed dual inhibition studies. Combined KC7F2 and etomoxir usage had no major effects on cell viability levels (Fig. S4A). We profiled the major tolerogenic cytokines IL-10 and IL-27 by flow cytometry and found their levels to be significantly impaired in NCoR1 depleted conditions when treated with the combined inhibitors (Fig. 5A and Fig. S4B). On the other hand, the levels of inflammatory cytokines were impaired significantly in control cells, suggesting that optimal glycolysis levels are important for induction of immunogenic response (Fig. S4C). At the same time, an increase in glycolysis above a threshold perturbs the immunogenic balance towards tolerance. NCoR1 depleted cells showed more dependency in terms of IL-10 and IL-27 secretion upon combined inhibition than individual perturbation with inhibitors (Fig. S4D). Furthermore, to get a global insight into the tolerogenic versus inflammatory responses, we performed RNAseq to investigate the DEGs, segregating with and without combined inhibition of HIF-1α and CPT1a. The principal component analysis of the 4 samples (1; Control cells activated with CpG, 2; Control cells activated with CpG and treated with KC7F2 + etomoxir, 3; NCoR1 KD cells activated with CpG, and 4; NCoR1 KD cells activated with CpG and treated with KC7F2 + etomoxir) depicted separate clusters, which indicated distinct transcriptome profiles (Fig. S4E). Then, we looked into the genes and their regulators pertaining to glycolysis and FAO. NCoR1 KD DCs at CpG 6h depicted enhanced expression of glycolytic rate-limiting genes like *Hk2, Pfkfb3, Ldha* and *Hk3* (Fig. 5B), and important regulators like Stat3, which is known for transcriptional up-regulation of HIF-1α and underlying glycolytic genes [55,56]. Stat3 expression is significantly upregulated in NCoR1 perturbed cells than control [57]. Furthermore, FAO genes like *Acsl5, Acox3* and *Hpgds* also showed significant enrichment (Fig. 5B). Upon combined inhibition, the expression levels of glycolytic and FAO
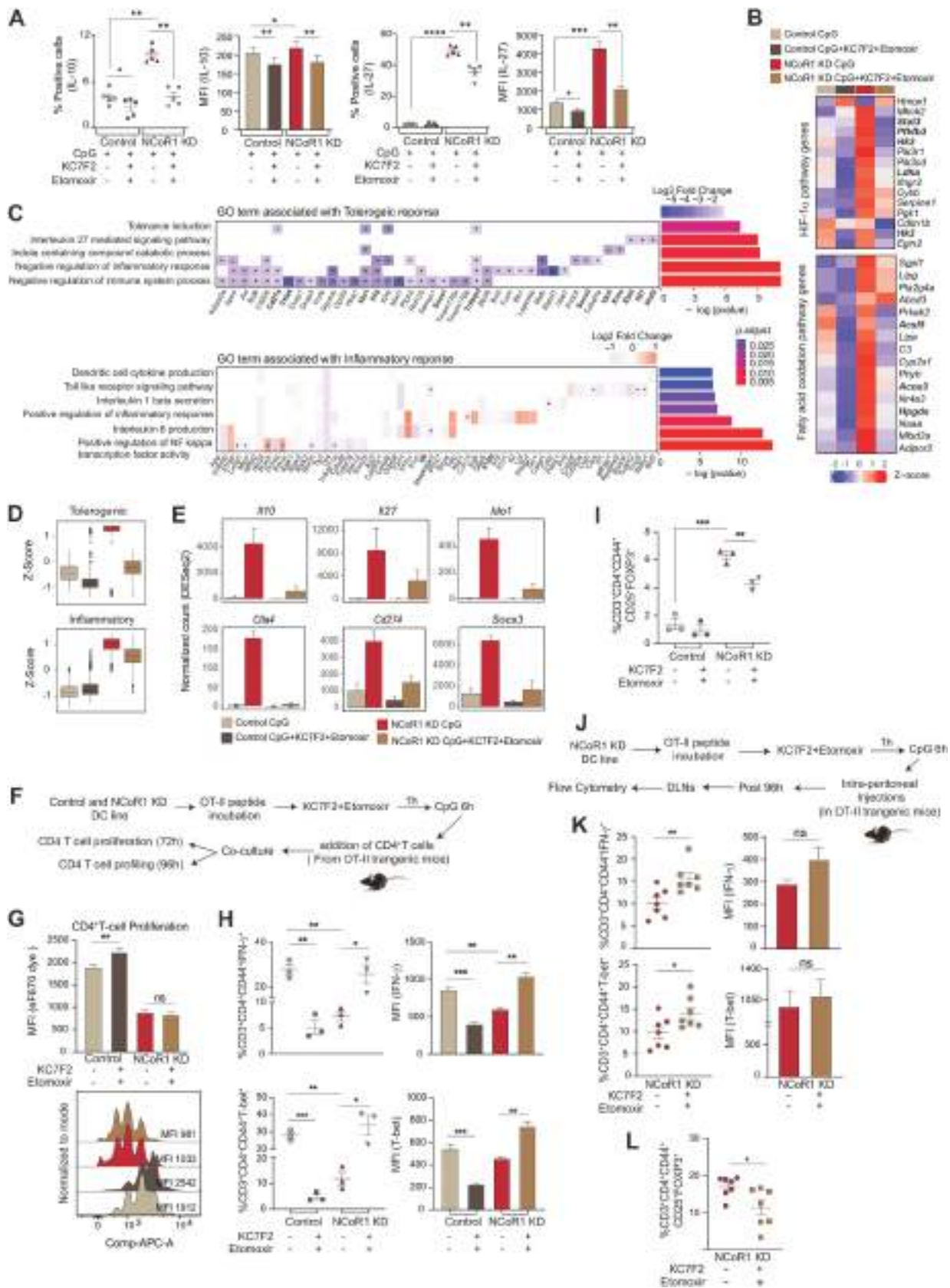
Fig. 5. Global transcriptomic changes and T cell polarization upon combined inhibition of HIF-1α and CPT1a

A. Scatter plots (percent positive cells) and bar graphs (MFI) showing the cytokine levels of IL-10 and IL-27 upon combined treatment with etomoxir (50μM) + KC7F2 (10μM) in 6h CpG activated control and NCoR1 depleted tolerogenic DCs. (n = 5)

B. Heatmap showing the differentially expressed genes of glycolytic and FAO pathway and their regulators in the RNAseq data before and after treatment with combined inhibitors KC7F2 and etomoxir in 6h CpG stimulated control and NCoR1 KD DCs. (n = 3)

C. Heatmap with bar plots showing the enriched GO terms associated with genes differentially regulated in 6h CpG activated NCoR1 KD before and after combined inhibition with HIF-1α and CPT1a. The asterisk in the heatmap denotes the significantly up or down regulated genes (p-adjusted <0.05 from DESeq2 results in CpG activated NCoR1 KD + Inhibitor treated as compared to only NCoR1 KD conditions. (n = 3)

D. Box plots depicting the distribution of gene expression (z-score) belonging to tolerogenic and inflammatory pathways with and without combined inhibition of HIF-1α and CPT1a in 6 h CpG activated control and NCoR1 KD DCs. (n = 3)

E. Bar graphs showing the normalized counts (DESeq2) of *Il10, Il27, Ido1, Ctla4, Cd274* and *Socs3* in 6h CpG stimulated control and NCoR1 KD DCs before and after combined inhibition of HIF-1α and CPT1a. (n = 3)

F. Schematic outline showing the control and NCoR1 KD DCsT cell co-culture experiment with the naive CD4$^+$T cells isolated from OT-II transgenic mice *ex vivo* in the presence and absence of combined inhibitors KC7F2 and etomoxir.

G. Bar graph and histogram plot showing MFI levels and shifts respectively of eF670 labelled CD4$^+$ T cells upon co-culturing with 6h CpG activated control and NCoR1 KD DCs before and after treatment with combined inhibitors of HIF-1α and CPT1a. Changes in the cell proliferation levels were measured for CD3$^+$CD4$^+$CD44$^+$ gated effector T cells by flow cytometry after 72 h of co-culture. (n = 6)

H. Scatter plots (percent positive cells) and bar graphs (MFI) showing the IFN-γ$^+$ and T-bet$^+$ cells gated on CD3$^+$CD4$^+$CD44$^+$ effector T cells upon co-culturing with control and NCoR1 KD DCs, with and without combined inhibition of HIF-1α and CPT1a. Percent positive cells and MFI levels were analyzed by flow cytometry after 96 h of co-culture. (n = 3)

I. Scatter plot showing the percent CD25$^+$ and FOXP3$^+$ double positive cells (Tregs) gated on CD3$^+$CD4$^+$CD44$^+$ effector T cells upon co-culturing with control and NCoR1 KD DCs, with and without combined inhibition of HIF-1α and CPT1a. (n = 3)

J. Schematic showing the outline of an *in vivo* experiment for polarization of naive T cells upon adoptive transfer of NCoR1 KD DCs intraperitoneally in OT-II transgenic mice with and without combined inhibition of HIF-1α and CPT1a. Nearest draining lymph nodes (DLNs) were harvested after 96 h to profile the Th1 and Tregs.

K. Scatter plots (percent positive cells) and bar graphs (MFI) showing the IFN-γ$^+$ and T-bet$^+$ cells, gated on CD3$^+$CD4$^+$CD44$^+$ effector T cells in DLNs after 96 h, representing the Th1 subtype in OT-II mice upon adoptive transfer of NCoR1 KD DCs with and without combined inhibition of HIF-1α and CPT1a. (n = 7)

L. Scatter plot showing the percent CD25$^+$ and FOXP3$^+$ double positive cells (Tregs), gated on CD3$^+$CD4$^+$CD44$^+$ effector T cells in DLNs after 96 h, representing the Treg subtype in the OT-II mice upon adoptive transfer of NCoR1 KD DCs, with and without combined inhibition of HIF-1α and CPT1a. (n = 7).

*p ≤ 0.05, **p ≤ 0.01, ***p ≤0.001 and ****p ≤0.0001. p-value has been calculated using two tailed paired [A, G, H and I] and unpaired [K and L] student's t-test. Error bars represent SEM.

genes were drastically reduced depicting the impact of combined effects of KC7F2 and etomoxir (Fig. 5B). To check the impact of inhibitor treatment on inflammatory and tolerogenic genes, we first identified unique or common genes differentially expressed upon inhibitor treatment at 6h CpG activated control and NCoR1 KD DCs. We found 381 genes to be significantly upregulated upon NCoR1 depletion in DCs compared to control, that in turn were found to be downregulated after combined inhibitor treatment (Fig. S4F). On the other hand, 1142 genes significantly upregulated in CpG activated NCoR1 KD DCs compared to control cells did not show any change upon treatment with inhibitors (Fig. S4F). Next, we performed gene ontology for biological process enrichment analysis of the above two gene sets using cluster Profiler. We plotted significantly enriched GO terms associated with inflammatory and tolerogenic response and the log2 fold change of genes in NCoR1 KD + inhibitor treated condition. Characteristic pathways such as tolerance induction, IL-27 mediated signalling pathway, Indole containing compound catabolic process, negative regulation of inflammatory response, and their associated genes like *Cd274, Ido1, Il10, Socs1, Tnfaip3, Socs3, Ido2, Kmo, Ebi3, Il27, Stat3* involved in tolerogenic function were significantly downregulated upon combined inhibitor treatment (Fig. 5C). On the other hand, inflammatory response genes (*Il6* and *Il12b*) or pathways such as dendritic cell cytokine production, TLR signalling pathway, positive regulation of inflammatory response, etc. did not show any significant change upon inhibitor treatment (Fig. 5C). Following this, we also plotted the distribution of z-scores of all the tolerogenic and inflammatory genes across different conditions. The median expression of the genes enriched for the tolerogenic pathway showed higher levels in NCoR1 KD, which significantly reduced after inhibitor treatment (Fig. 5D). On the other hand, the genes enriched for inflammatory pathways showed no significant difference after inhibitor treatment (Fig. 5D). We also investigated the normalized expression of a few candidate genes such as *Il10, Il27, Il12, Il6, Ido1, Ctla4, Cd274,* and *Socs3*. Upon inhibitor treatment, the tolerogenic genes that showed enhanced expression in CpG activated NCoR1 KD DCs depicted substantial impairment in expression, however, no significant changes were observed in the inflammatory genes (Fig. 5E and Fig. S4G).

Furthermore, specific target genes of HIF-1α were also analyzed from the Harmonizome database that has a curated list from chromatin enrichment analysis (CHEA). We found that out of a total of 341 target genes, 40 genes were differentially expressed after inhibitor treatment in control DCs and 17 genes were differentially expressed after inhibitor treatment in NCoR1 KD DCs. Three different clusters were obtained for these differentially expressed target genes (Fig. S4H). Cluster 1 showed upregulation of DEGs upon inhibitor treatment, possibly the negative regulators whereas cluster 2 mainly depicted *Hif-1α* targeted metabolic genes. These were significantly upregulated in the NCoR1 KD condition and showed diminished or reduced expression upon inhibitor treatment. Cluster 3 didn't show any major change. Overall, combined inhibition of HIF-1α and CPT1a displayed potent dysregulation of glycolytic and FAO pathways that significantly impacted the levels of tolerogenic genes with either little or no significant changes in inflammatory ones. Functionally, to delve into the T cell response induced by these DCs upon combined inhibitor treatment, we performed DC-T cell co-culture experiments using CD4$^+$ T helper cells from OT-II transgenic mice. Control and NCoR1 KD cDC1 were pulsed with OT-II peptide (ISQAV-HAAHAEINEAGR) overnight followed by 1 h of pre-treatment with inhibitor (combined KC7F2 + etomoxir) before 6h of CpG activation and incubation with FACS sorted CD3$^+$CD4$^+$ OT-II T cells (Fig. 5F). The sorted CD4$^+$ T cells showed more than 90% purity (Fig. S4I). The proliferation of CD4$^+$ T cells was determined using the eF670 dye after an incubation of 72 h. Combined inhibitor treatment suppressed the CD4$^+$ T cell proliferation in control cells whereas no change was observed in the proliferative capacity in the NCoR1 KD conditions (Fig. 5G). Following proliferation, the profiling of these co-cultured CD4$^+$ T cells into Th1 and Treg subtypes was performed. Control and NCoR1 KD cells behaved conversely with combined inhibition. In the control DC with inhibitor treatment conditions, we observed a significantly decreased percentages of IFN-γ$^+$ and T-bet$^+$ populations (Th1 phenotype) as compared to untreated cells (Fig. 5H). On the contrary, in NCoR1 depleted and combined inhibitor treated conditions the frequency of Th1 populations were significantly upregulated, when compared to untreated NCoR1 KD DCs (Fig. 5H). These results complemented the

cytokine and transcriptomic data obtained with the combined inhibition. Further, to affirm the observed inflammatory phenotype in NCoR1 KD DCs, CD25+FOXP3+ (Tregs) populations were also identified. Control cells displayed non-significant changes in this population whereas, NCoR1 KD condition showed significant lower percentages of Tregs (Fig. 5I), which provided functional evidence of depleted tolerogenic cytokines with an intact inflammatory response upon dual inhibitor treatment. A similar experiment was performed using FLT3L differentiated primary NCoR1$^{DC-/-}$ BMDCs. On day 9 of differentiation, cells were treated with OT-II peptide overnight, followed by 1h of combined KC7F2+etomoxir treatment and CpG stimulation for 18h. The profiling data showed similar results as the cDC1 line (Fig. S4J). To further negate experimental artefacts obtained during *ex vivo* experiments, we performed an *in vivo* study, where NCoR1 perturbed DCs (5×10^6) with and without dual perturbation of HIF-1α and CPT-1a were injected intraperitoneally into OT-II transgenic mice. Ova incubation, inhibitor treatment, and CpG stimulation were done *in vitro* for these cells as explained before (Fig. 5J). On day 5, draining lymph nodes from animals were harvested and Th1 and Treg populations were determined by flow cytometry. The *in vivo* results were complementary to the *ex vivo* ones, which further substantiated the observed phenotype (Fig. 5K-L and Fig. S4K-M). Overall, T cell polarization studies confirmed the functional aspect of the impaired inflammatory and tolerogenic responses obtained in control and NCoR1 depleted DCs respectively.

2.7. Combined KC7F2+etomoxir treatment facilitates Mtb (H37Rv) clearance in NCoR1 depleted DCs ex vivo and in vivo

Studies have reported on the complex immune regulatory networks perturbed by *Mtb* infection to increase its survival. *Mtb* infection upregulates mTOR activity and upon treatment with rapamycin, IL-12 production and Th1 response goes high to clear the pathogen [58]. The former results exhibited active perturbation of HIF-1α and CPT1a in NCoR1 depleted DCs promoted a Th1 response via reduction of IL-10 to IL-12 cytokine balance. To further elucidate the physiological relevance of the immunostimulatory capacity of NCoR1 KD DCs with combined inhibition, we infected NCoR1$^{DC-/-}$ BMDCs with mCherry tagged *Mtb* (H37Rv strain) and harvested the cells at 2 h and 18 h post infection (Fig. 6A). Combined inhibition significantly reduced the bacterial load both at percent positive and MFI levels from the F4/80−CD11c+CD24+ NCoR1$^{DC-/-}$ BMcDC1s at 2 h and 18 h post-infection (Fig. 6B). Further, to validate our results *in vivo*, we infected NCoR1$^{DC-/-}$ KO mice with 1 × 10^6 CFUs of GFP expressing *Mtb* (H37Rv strain) intranasally. Mice in the control group were infected with only *Mtb* whereas, the drug treated group received treatment of KC7F2+etomoxir at day 3, day 8, day 12, and day 16 intraperitoneally after *Mtb* infection. Animals were sacrificed on day 21 to determine the bacterial burden in lung DCs and Th1 response in the Spleen (Fig. 6C). The lung CD11c+CD103+ DCs (cDC1 counterpart in lungs) showed significantly reduced *Mtb* burden upon combined inhibition (Fig. 6D and Figs. S5A–B) however, the overall bacterial burden in the lungs was found to be increased (Fig. S5C). A plausible explanation for the same can be drawn from hypoxia mediated studies for *Mtb* survival in lungs [59]. On the other hand, increased Th1 response (IFN-γ+ and T-bet+ effector T cells) were observed in splenic cells with no significant changes in the FOXP3+ cells (Fig. 6E and Figs. SD–E). Since, *Mtb* infection modulates the host immune response towards tolerance for survival, our results on the combined KC7F2+etomoxir treated NCoR1$^{DC-/-}$ BMcDC1s and lung CD103+ DCs demonstrated increased Th1 responses and pathogen clearance.

2.8. Human tolerogenic moDCs showed reduced NCOR1 expression and increased Th1 phenotype upon combined KC7F2+etomoxir treatment

To establish a relationship between NCOR1 and tolerance, we sought to investigate the correlation of NCOR1 expression with tolerogenic genes in primary human moDCs differentiated with GM-CSF and IL-4.

From a publicly available dataset [60], we observed a negative correlation of *NCOR1* with *IL10* (p = 0.079) and *SOCS3* (p = 0.038) in mature moDCs (Fig. 7A). This suggested an inverse relationship between NCOR1 and tolerance. Human conventional DCs treated individually or in combination with Dexamethasone (Dex), VD3, and rapamycin show characteristic tolerogenic features [61]. Therefore to further confirm this assertation, we also checked the normalized expression of *NCOR1* (n = 4) between mature and other tolerogenic groups [60] and observed a significantly decreased expression in the Dex treated group compared to untreated mature moDCs (Fig. 7B). Next, to validate this observation, we derived CD14+ monocytes from PBMCs of healthy individuals (n = 5) followed by its differentiation into moDCs using GM-CSF and IL-4. The differentiated moDCs were divided into two groups, 1) Dex induced tolerance, and 2) mature control moDC group. To induce tolerance and activation in these moDCs, mature moDCs were treated with Dex for 5 days followed by 24 h of PolyIC (pIC) stimulation (Fig. 7C). Since human moDCs lack TLR9 expression, potent activation was attained using pIC [62]. The relative mRNA expression of *NCOR1* was found to be significantly downregulated with an upregulation of tolerogenic gene *IL-10* and downregulation of inflammatory gene *IL-12* in the Dex-treated tolerogenic group (Fig. 7D). Further, glycolytic genes like *HK2* and *LDHA* also showed enhanced expression (Fig. 7D). Next to confirm the NCOR1 expression at protein level, we performed confocal microscopy. The Dex-treated tolerogenic group showed significantly reduced NCOR1 protein levels as compared to the untreated mature moDCs (Fig. 7E). The above results suggested a strong inverse relationship of NCOR1 with tolerance in human moDCs. A previous study on human moDCs has shown that tolerogenic cells are dependent on glycolysis, glycolytic capacity, and FAO [17,18]. Therefore, we hypothesised that combined treatment of KC7F2+etomoxir could restore the inflammatory phenotype of the tolerogenic moDCs. To validate the effect of combined inhibition, we co-cultured the Dex-treated tolerogenic moDCs with primary CD4+ T cells. We checked the proliferation and polarization of these T cells co-cultured with and without inhibitor treated moDCs (Fig. 7F). The CD4+ T cells conjugated with the eF670 proliferation dye showed reduced proliferation as evident from decreased P2 population and increased MFI shifts for the Dex-treated tolerogenic group. However, with the combined inhibition of KC7F2+etomoxir, the proliferative capacity of the CD4+ T cells were rescued (Fig. 7G). Furthermore, Th1 response cytokine IFN-γ and transcription factor T-bet gated on CD3+CD4+ T cells showed reduced expression in the tolerogenic group that was found to be restored upon combined treatment (Fig. 7H). Overall, our findings suggested a direct role of NCoR1 in regulation of immune tolerance in human moDCs which could be reversed in terms of proliferation and Th1 response upon combined inhibition of glycolysis and FAO using KC7F2 and etomoxir, respectively.

3. Discussion

DC activation profiles converge into an abundance of descending signals that strategize various molecular cues at the transcriptional and translational level to elicit an antigen-specific immunological responses [63]. Alteration in cellular metabolism forms an important aspect of immune response in DCs. DCs when activated, they orchestrate metabolic reprogramming processes and shift towards a glycolytic profile with altered TCA cycle activity, and lower OXPHOS [4]. Several types of research have focused on the pathways that initiate DC metabolism, however limited studies have shown how it is being negatively regulated. The interplay between anabolic and catabolic processes is pivotal for a fine-balance of immunogenicity and tolerogenicity in DCs. It has been observed that anabolic metabolism in general is associated with the induction of immunogenic responses in DCs, whereas the catabolic pathways and active mitochondrial respiration are important for regulating tolerogenic function [11,13]. Hence, our study primarily focused on the catabolic routes of metabolism to understand the molecular mechanisms underlying tolerance in NCoR1-depleted DCs. We have
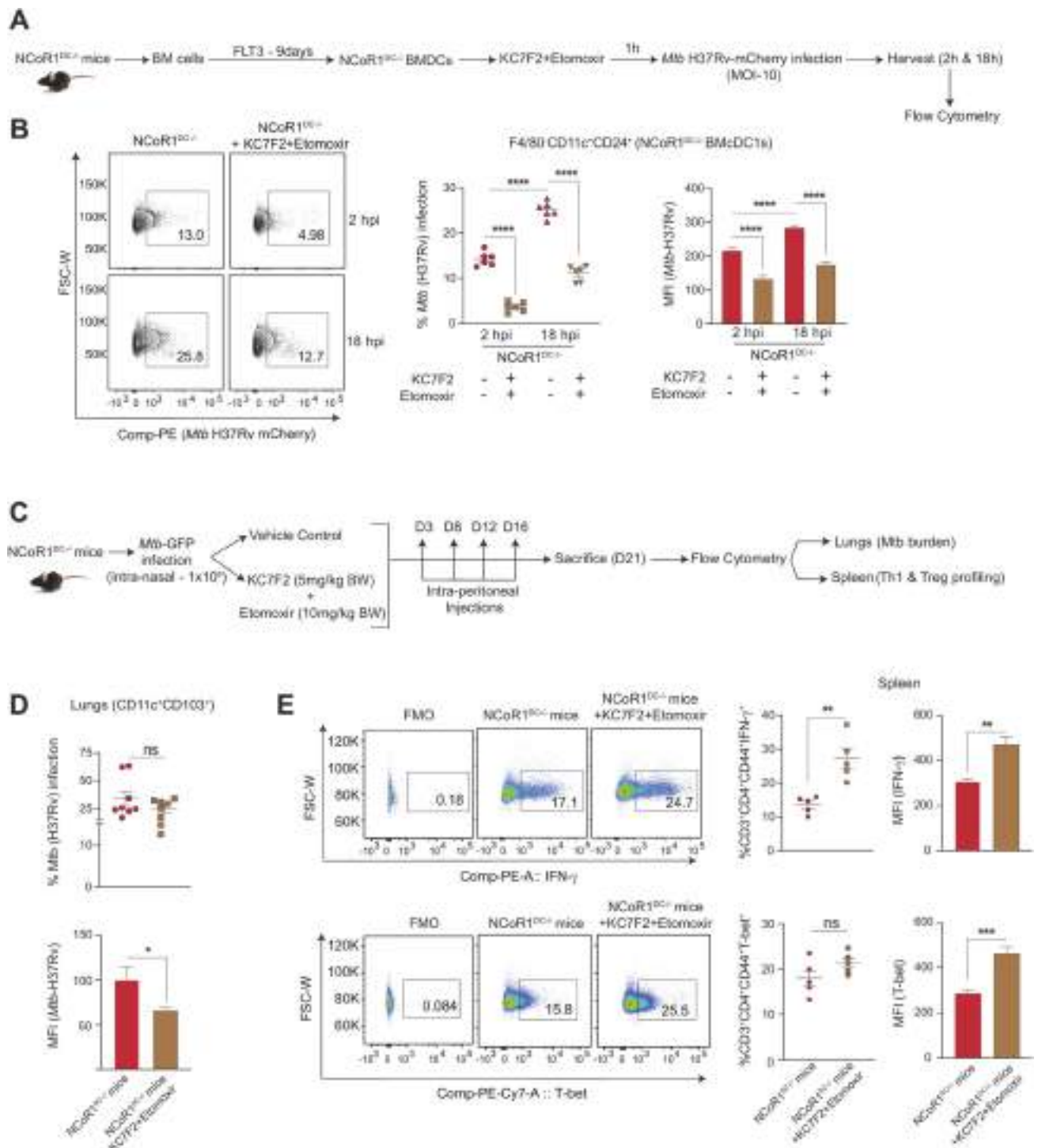
Fig. 6. *Mtb* disease burden upon dual inhibition of HIF-1α and CPT1a in NCoR1[DC−/−] mice *ex vivo* and *in vivo*

A. Schematic showing the mCherry-*Mtb* (H37Rv) infection in primary NCoR1[DC−/−] BMcDC1s gated on F4/80−CD11c+CD24+ cells with and without combined treatment with KC7F2 and etomoxir. The cells were harvested after 2h and 18h post infection (hpi) and analyzed by flow cytometry.

B. Representative FACS contour plot depicting gating of *Mtb* infected cells, along with scatter plot and bar graph showing the cumulative percent infection and change in MFI levels with and without combined treatment with KC7F2 and etomoxir at 2h and 18h post infection in NCoR1[DC−/−] BMcDC1s. (n = 6)

C. Schematic outline showing the GFP-*Mtb* (H37Rv) infection *in vivo* in NCoR1[DC−/−] mice with (inhibitors were injected intraperitoneally at day 3, day 8, day 12 and day 16 post infection) and without combined inhibition with KC7F2 and etomoxir. Mice were sacrificed on day 21 to check bacterial burden in CD103+ lung DCs (cDC1 counterpart in lungs) and Th cell phenotype in spleen.

D. Scatter plot and bar graph showing the cumulative percent infection and change in *Mtb* burden (MFI) in lung DCs (gated on CD11c+CD103+ cells) in NCoR1 DC−/− mice at day 21 with and without combined treatment with KC7F2 and etomoxir. (n = 8)

E. Representative FACS dot plots depicting the gating of IFN-γ+ and T-bet+ cells gated on CD3+CD4+CD44+ effector T cells in the Spleen of treated and untreated mice. Scatter plots and bar graphs showed the cumulative percent infection and change in MFI levels at day 21 with and without combined treatment with KC7F2 and etomoxir in NCoR1[DC−/−] mice. (n = 5)

*p ≤ 0.05, **p ≤ 0.01, ***p ≤0.001 and ****p ≤0.0001. p-value has been calculated using two tailed unpaired student's t-test. Error bars represent SEM.
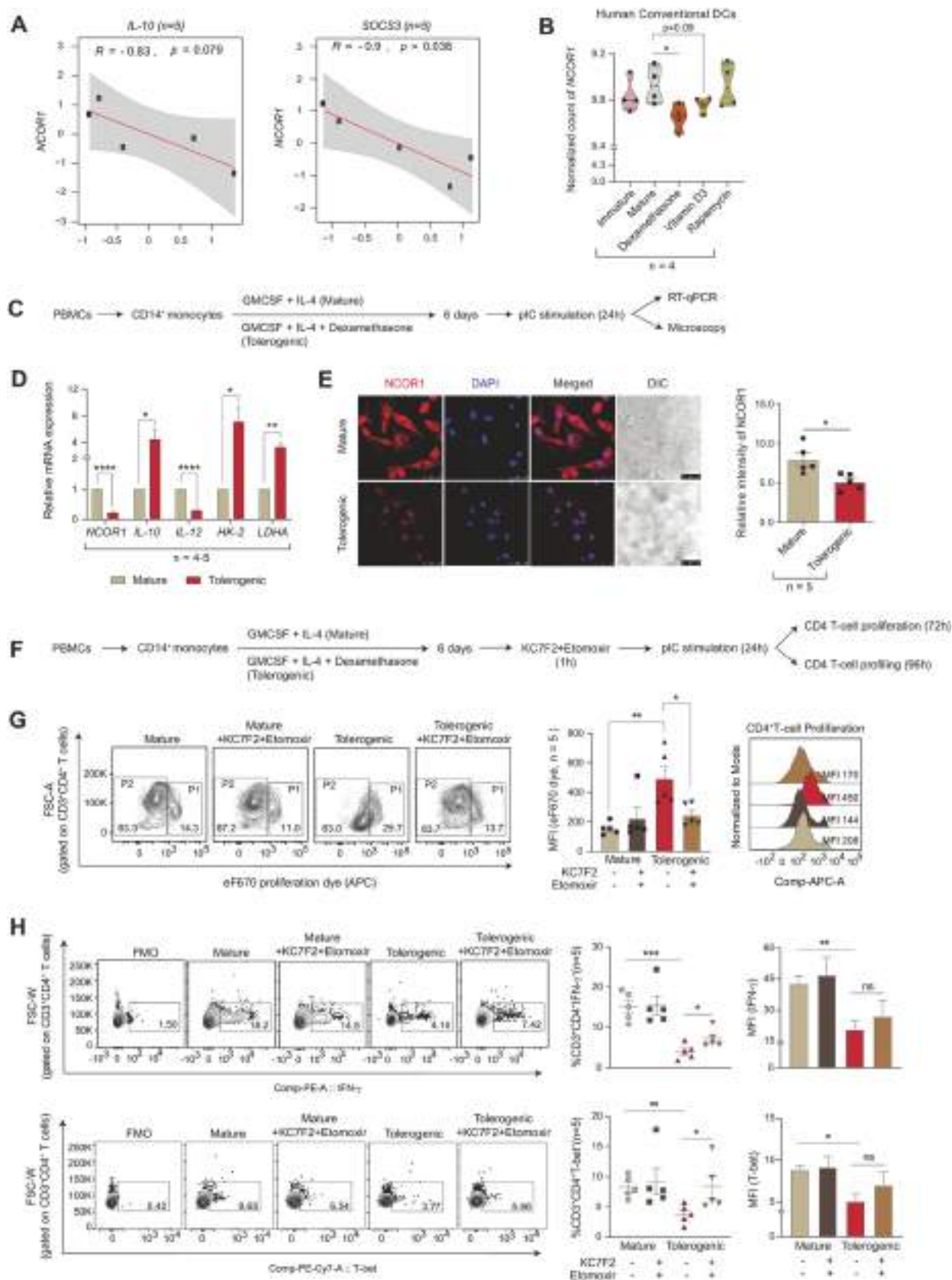
(caption on next page)

Fig. 7. NCOR1 expression and T cell polarization in human PBMCs derived moDCs

A. Scatter plot showing the correlation between *NCOR1* and tolerogenic genes *IL-10* and *SOCS3* from a publicly available RNAseq dataset. (n = 5)

B. Violin plot showing the normalized counts of *NCOR1* in human conventional DCs in immature, mature, and in different tolerogenic setup (Dex, VD3 and rapamycin treated groups), from publicly available RNAseq datasets. (n = 4)

C. Schematic showing the experimental outline used for differentiation of mature and tolerogenic (Dex-treated) moDCs to check the mRNA (RT-qPCR) and protein level expression of NCOR1.

D. Bar plots depicting the relative mRNA expression of *NCOR1, IL-10, IL-12, HK-2* and *LDHA* in mature and tolerogenic moDCs after 24h pIC stimulation. (n = 4–5)

E. Representative microscopic images showing the NCOR1 protein levels (red) in mature and tolerogenic moDCs after 24h pIC stimulation. Corresponding bar graph depicted the quantification of the NCOR1 intensities in the microscopic images. (n = 5)

F. Schematic showing the CD4 T cell proliferation and T cell subtype profiling after 24h pIC stimulation in the co-culture of CD4$^+$ T cells with mature and tolerogenic moDCs with and without KC7F2 and etomoxir treatment.

G. Representative FACS contour plots showing the gating of P1 and P2 populations of eF670 stained CD3$^+$CD4$^+$ T cells upon co-culture with mature and tolerogenic moDCs with and without combined treatment with KC7F2 and etomoxir after 72h after 24h pIC stimulation. Corresponding bar graph depicted the cumulative MFI shifts calculated from independent biological replicates and histogram showed the representative MFI shifts observed. (n = 5)

H. Representative FACS contour plot showing the gating of IFN-γ$^+$ and T-bet$^+$ populations gated on CD3$^+$CD4$^+$T cells upon co-culturing with moDCs for 96 h. Scatter plots and bar graphs depicted the cumulative percent positive and MFI shifts of IFN-γ$^+$ and T-bet$^+$ cells in mature and tolerogenic moDCs conditions with and without combined treatment with KC7F2 and etomoxir at 24h pIC stimulation.(n = 5)

*p ≤ 0.05, **p ≤ 0.01, ***p ≤0.001 and ****p ≤0.0001. p-value has been calculated using two tailed unpaired student's t-test. Error bars represent SEM. . (For interpretation of the references to colour in this figure legend, the reader is referred to the Web version of this article.)

recently identified that NCoR1 depletion induces strong immune tolerance in DCs [31]. Since the NCoR1 co-repressor complex regulates the functionality of mitochondrial metabolism in fat and muscle cells, we hypothesised a potential link of NCoR1 in regulating a fine-balance of immunogenic and tolerogenic responses in DCs through energy metabolism [24,26]. Murine and human DCs have been demonstrated to drive T cell polarization through distinct metabolic changes. Metabolic adaptations to OXPHOS and FAO help DCs meet their metabolic needs in the steady-state and TLR ligation with specific cytokine milieu maintains the cells in an immature and tolerogenic condition [2]. NCoR1 depleted tolerogenic DCs depicted enhanced glycolysis, glycolytic capacity, extracellular lactate and direct binding at the genomic regions of *pfkp* and *pfkfb3*. The role of glycolysis in regulating DC inflammation is well acknowledged. It does, however, play a crucial role in immunological tolerance also. Tolerogenic DCs have been known to show increased glycolysis [64]. Increased glycolysis results in greater lactate buildup and extracellular media acidification. In co-culture experiments with naive CD4$^+$ T cells, DCs with substantial lactate accumulation limit proliferation and polarize towards Tregs. This occurs as a result of T cells intaking lactate and thereby reducing their glycolysis and proliferation. VD3, a synthetic anti-inflammatory inducer, also depicts similar profiles [18,65]. Sustained activation in murine and human tolerogenic DCs regulate glucose metabolism and increased glycolysis by PI3K/AKT/mTOR axis by stabilising HIF-1α expression [66,67]. This signalling axis similarly favoured the enhanced glycolytic rate in our NCoR1 ablated tolerogenic DC model. Several other groups have also reported the functioning of the former signalling axis greatly in DCs [17,68–70]. HIF-1α perturbation led to decreased glycolysis and reduced secretion of tolerogenic cytokines in NCoR1 KD cells remarkably. Dependency on HIF-1α proved to be vital and more dominant than mTOR. Moreover, NCoR1 binding peaks at the *Hif-1α* genomic region are reasoned enough for direct regulation of glycolytic genes through NCoR1 [71].

On the other hand, mitochondrial respiration in control and NCoR1 depleted tolerogenic DCs depicted a similar pattern as reported earlier [2]. We also showed that mitochondrial SOX and cellular ROS levels were significantly downregulated in NCoR1 depleted DCs both in the DC line and in cDC1 BMDCs upon CpG stimulation (Figs. 1K and 2E), despite the fact that NCoR1 depleted cells depicted enhanced glycolysis and OXPHOS. This can be because the immunogenic DCs are remarkable in producing ROS to elicit inflammatory responses, whereas, tolerogenic ones show subdued ROS levels, which may be the case for NCoR1-depleted ones [5,6,72]. The next important question was how NCoR1 depleted tolerogenic DCs had higher levels of OXPHOS even after CpG activation than control cells. We focussed on the three important routes generating reducing powers to facilitate TCA cycle and thereby OXPHOS [73,74]. In NCoR1 KD cells, DEGs of the TCA cycle for pyruvate and glutamine oxidation were downregulated, which was

substantiated by the observed decreased dependence. Further suppression of pyruvate oxidation decreased IL-12p40/70 secretion while increasing IL-10. This metabolic node turned out to be a crucial feature for inflammation. Whereas inhibition of glutaminolysis with BPTES and DON, considerably enhanced IL-10 secretion in both control and NCoR1 KD DCs while having no effect on IL-12p40/70 levels, implying a crucial relationship between tolerance and glutaminolysis. Such intricate balance is also depicted in human pDCs under TLR stimulation and glutaminolysis inhibition [75]. The third important node which modulates inflammation versus tolerance is fatty acid oxidation. Increased expression of the rate-limiting β-oxidation gene *Cpt1a* along with DEGs in NCoR1 KD cells resulted in a higher OCR dependent FAO index. This provided evidence for active OXPHOS being operated through β-oxidation under TLR9 specific CpG stimulation. PPAR-γ mediated intracellular fatty acid reserves fuelled the FAO index and NCoR1 binding at the genomic regions of PPAR-γ further validated the whole cyclical aspect being operated to drive active OXPHOS in these cells. Deposition of neutral lipids in NCoR1 KD cells suggests the presence of increased lipid synthesis which requires NADPH. Because NADPH can be generated via the PPP, IDH1, and ME1 related pathways. Increased malic acid with reduced PPP and non-significant *Idh1* probably explains the accumulation of lipids and decreased ROS levels within the NCoR1 depleted DCs [76,77]. Maintenance of tolerance primarily through glycolysis and FAO is well established. But until now no study has depicted combinatorial effects of dual inhibition of HIF-1α and CPT1a on immune-tolerance and T cell responses. Combined inhibition changed the global transcriptomic landscape of tolerogenic response genes for NCoR1 KD cells. While inflammatory response genes were largely unchanged. Co-culture studies further affirmed the intact inflammation by showing increased Th1 response *ex vivo* and *in vivo*. On the contrary, control DCs showed reduced secretion of IL-6 and IL-12p40/70 levels and subdued Th1 response. This depicts an intricate fine balance of metabolic pathways for inflammation and tolerance in control and NCoR1 KD DCs. Physiologically, NCoR1 depleted DCs effectively cleared *Mtb* burden upon treatment with combined inhibitors. Although bacterial burden was decreased in lung DCs, there was an overall increase in *Mtb* survival in lungs, suggesting decreased HIF-1α expression as a prominent feature of *Mtb* survival [59]. Modulation of inflammatory versus tolerogenic behaviour in *Mtb* infected host cells is a pivotal immune response mechanism regulated both by *Mtb* and host factors. Rewiring of host metabolic machinery by *Mtb* for increased survival is also conjugated with the defence mechanism [78]. Further, to develop a correlation between NCoR1 with tolerance in human moDCs, a Dex-treated tolerogenic state was attained. Significant reduction in the expression levels of NCoR1 in mRNA and protein established a strong relationship between them. The differential regulation of energy metabolism of tolerogenic human moDCs upon dual impairment appeared to demonstrate

a similar bioenergetic pattern to the murine ones. Increased proliferative capacity and Th1 response corroborated the same.

In conclusion, correlation of NCoR1 with tolerance in human moDCs and can act as a potential biomarker for diseases encompassing inflammatory versus tolerogenic states like in IBDs (inflammatory bowel diseases). Subsequently, HIF-1α and FAO inhibitors at optimal doses can mitigate inflammatory responses in murine DCs, its validation in human setup needs further investigation.

4. Limitations of the study

We have used mutu-cDC1 lines to perform initial experiments, since homogenous primary CD8α$^+$ cells are difficult to isolate, and they undergo activation during the purification process. It is also reported that metabolic experiments performed on sorted and magnetic selected cells alter redox state and cellular metabolome [79]. Hence, we considered total FLT3 differentiated BMDCs for extracellular flux assays. Since, both cDC1 and cDC2 cell types depict upregulation of tolerogenic genes in NCoR1 depleted conditions [31].

Contributions

Conceptualization, K.S., R.P., G.P.M., and S.K.R.; Methodology, K.S., R.P., A.J., G.P.M., S.P1., S.C., S.S., S.P2., A.S., M.S., R.K.N. and S.K.R.; Investigation, K.S., R.P., A.J., G.P.M., S.C., R.K.N and S.K.R.; Writing – Original Draft, K.S., and S.K.R.; Data Curation, G.P.M and S.K.R.; Formal Analysis, G.P.M.; Supervision, S.K.R., Visualization, K.S., R.P., A.J., G.P.M., and S.K.R.; Funding Acquisition, S.K.R.

Declaration of completing interest

The authors declare no competing interests.

Data availability

Data will be made available on request.

Acknowledgements

Appendix A. Supplementary data

Supplementary data to this article can be found online at https://doi.org/10.1016/j.redox.2022.102575.

Materials and Methods

Mice

CD11c specific homozygous NCoR1 KO (Knockout) mice were used for performing the *ex vivo* and *in vivo* experiments. Mice generation and selection of homozygous progenies were carried out as reported

elsewhere [31]. For KO confirmation, genotyping was done from DNA extracted from ear tissue. Briefly, tissue samples were treated with 50mM NaOH and heated at 95°C for 35 min followed by 1 M Tris-Cl (pH-8.0) treatment and centrifuged at 12,000 rpm for 5 min at RT. DNA was processed for PCR using NCoR1 loxP and CD11c Trans gene specific forward and reverse primers. The primer sequences are listed in the key resource table. PCR products were loaded onto a 0.8% agarose gel for confirming the presence or absence of NCoR1 loxP and CD11c Trans gene bands.

OT-II (gifted by Prof. Hans Acha-Orbea) and FLT3 (gifted by Ton Rolink) transgenic mice were transported from Switzerland. CD11c specific NCoR1 KO, CD11c Cre, OT-II, FLT3, and C57BL/6 mice were bred and maintained at the ILS animal facility.

Dendritic Cell (DC) Culture

The CD8α+ murine tumour cDC1 DC line was gifted by Prof. Hans Acha-Orbea. The DC line showed characteristic phenotypic and functional resemblance to type-I splenic CD8α conventional DCs [80]. The cell line was cultured in IMDM-glutamax media supplemented with 10% FBS, PenStrep, Sodium bicarbonate, HEPES buffer, and β-mercaptoethanol, and further maintained in a humidified incubator at 37 °C with 5% CO$_2$. For *invitro* experiments, potent activation was attained when challenged with TLR9 specific CpG-B at a concentration of 1 μg/ml for 6 h.

Generation of Stable NCoR1 KD CD8α$^+$ DC line

Stable control and NCoR1 KD DC lines were generated using pre-cloned shRNA constructs under the pLKO.1 lentiviral vector backbone (Sigma). Three different shRNAs targeting complementary determining sequence (CDS) and 3′UTR regions were selected for transduction. The mean KD efficiency with shRNA 2 was highest (~80%) and hence chosen for experiments. Transfection of HEK (293T), generation of viral particles, and transduction in the DC line was followed as reported earlier [31]. Stable cells were selected using Puromycin. The KD efficiency was quantified using a RT-qPCR primer specific to the mouse *Ncor1* gene. The primer sequences are listed in the key resource table.

RNA isolation and RT-qPCR

The extraction of RNA was done using Trizol reagent (RNA isoplus). Briefly, cells at specific densities (DC line - 1 × 10^6 and BMDCs - 3 × 10^6 cells/well) in a 6 well plate were treated with 500μl of Trizol reagent and kept at −80 °C until processing. During processing 100μl of chloroform was added and vortexed vigorously for 30 s. The Trizol-chloroform mixture was centrifuged at 11,000 g for 10 min at 4°C. After centrifugation, the aqueous phase of the mixture was taken, and an equivalent amount of isopropanol was mixed and incubated for 5 min. After incubation, the mixture was again centrifuged at 11,000 g for 10 min at 4 °C. Following this 300μl of ethanol was added and centrifuged at a maximum speed in a table top centrifuge at 4°C. The supernatant thus obtained was discarded and the pellet was kept for air drying. Finally, resuspension was done in nuclease-free water (NFW) and the amount was quantified using nanodrop (Thermo). Then 1μg of total RNA was used to prepare cDNA using high-capacity cDNA Reverse Transcriptase kit (Applied Biosystems). Quantitative PCR was performed using Power SYBR Green (Applied Biosystems) and PCR amplification was monitored in real-time using Quant studio 6 Instrument (Applied biosystems). Primer pairs used are listed in the key resource table.

Generation of Bone Marrow-Derived DCs (BMDCs) for ex vivo Studies

Male or female mice of age 6–8 weeks were sacrificed by CO$_2$ inhalation, and tibias and femurs were surgically removed under aseptic and sterile conditions. The bones were cut at an angle of 45° at the ends

and marrow was flushed out in RPMI-1640 media with the help of a 5 ml syringe. Single-cell suspension was prepared, and clumps were removed with the help of a 70μm cell strainer. The cells were centrifuged at 400g for 5 min at 4°C. The pellet was suspended with a 1x RBC lysis buffer (Tonbo) for 5 min on ice. The bone marrow cells were washed as previously and counted for seeding. The cells were plated in a 6 well having 6×10^6 cells/well with FLT3 sera (from FLT3 transgenic mice). The cells were cultured at 37°C in an incubator containing 5% CO_2 and left untouched for 9 days. Loosely adherent differentiated cells were collected, counted, and re-plated for experiments.

Inhibitor treatment and Flow Cytometry (FACS)

DC line and BMDCs were processed with 1 h pre-incubation with inhibitor treatments with rapamycin (20nM), KC7F2 (10μM), UK-5099 (5μM), BPTES (5μM), DON (5μM), and etomoxir (50μM) followed by CpG stimulation (6 h in DC line and 18 h in BMDCs) and BFA treatment for 4 h. Combined inhibitor studies with KC7F2 and etomoxir were performed in a similar manner. Thereafter cells were harvested and processed with flow cytometry. Surface and intracellular (IC) staining were done sequentially for experiments. In the DC line and BMDCs, control and NCoR1 perturbed cells were processed for surface staining for 30 min at 4°C in 1x FACS buffer (3% FCS in 1x PBS, 5 mM EDTA) followed by intracellular staining upon fixation and permeabilization with 2% PFA and 1x Perm buffer respectively. The IC staining cocktail was prepared in a Perm buffer and incubated with cells for 45 min at room temperature in the dark. During the estimation of Mitochondrial SOX (5μM), cellular ROS (according to manufacturer's recommendations) and mitochondrial potential with TMRM (20nM), cells were incubated with corresponding dyes in the culture medium for 20 min at 37°C in a 5% CO_2 incubator and proceeded for flow cytometry after washing with 1x FACS buffer. The acquisition was done using an LSRII fortessa flow cytometer (BD Biosciences). The acquired data were analysed using FlowJo-X software (Treestar). Antibodies and dyes used for flow cytometry experiments are listed in the key resource table.

DC - T cell co-culture experiments

For the *ex vivo* DC-T cell co-culture experiment, mutuDC line and FLT3 differentiated BMDCs (10,000 cells/condition) were pulsed with OVA peptide (323–339)/OT-II at 200nM concentration overnight. Thereafter cells were washed and combined inhibitor treatment with KC7F2 (10μM) and etomoxir (50μM) for 1 h and CpG stimulation for 6h in the DC line and 18h for BMDCs were done. Sorted CD3$^+$CD4$^+$ T cells were added to the DCs at a ratio of 1:10. Following this, T cell proliferation was determined using amine-based dye (eFlour670-APC-1μM) after 72h. Whereas, T cell differentiation into Th1 (T-bet$^+$ and IFN-γ$^+$) and Tregs (CD25$^+$ and FoxP3$^+$) were determined by flow cytometry upon restimulation with PMA (10 ng/ml), Ionomycin (500 ng/ml) and Brefeldin A (2.5 μg/ml) together for 5h after 96h. Effector T cells were identified using CD44 as a marker. For the *in vivo* experiment, NCoR1 KD DCs were OVA pulsed, treated with dual inhibitors and CpG stimulated *invitro*. These cells (5×10^6 cells/mice) were injected intraperitoneally (I.P) into OT-II transgenic mice and nearest draining lymph nodes were collected after 4 days for determining the Th1 vs Treg subtype. Cells thus obtained from draining lymph nodes were stimulated for 5h with PMA/Iono/BFA before proceeding for flow cytometry. Antibodies used for flow cytometry experiments are listed in the key resource table.

Mitochondrial DNA copy number estimation

In 12 well plates, control and NCoR1 KD DCs were grown, and roughly 0.5×10^6 cells were collected per condition. Cells were centrifuged and resuspended in 300μl of Tissue and cell lysis solution (Lucigen) containing proteinase K and mixed thoroughly. Next, samples were incubated at 65°C for 15 min and vortexed every 5 min. After

which samples were cooled to 37°C and RNase A was added. Next, they were placed on ice for 3–5 min and proceeded with DNA precipitation. During this step 150μl of Protein Precipitation Reagent (PPR-Lucigen) was added to the 300μl of lysed samples and vortexed vigorously for 10 s. Thereafter, samples were centrifuged at 4°C for 10mins at 10,000g, supernatant was collected and pellets were discarded. 500μl of isopropanol was added, mixed and centrifuged to collect the DNA pellet. Final resuspension was done in 30μl of TE buffer and quantified. The DNA thus obtained, were processed for RT-qPCR with *Nd-1* and *Hk-II* primer pairs along with Power SYBR green. Ct of *Hk-II* - Ct of *Nd-1* gave the dCT value. Mitochondrial DNA copies were calculated as $2*2^{\hat{}}(dCT)$.

Extracellular Nitrite assay

Control and NCoR1 KD DCs were cultured in 6 well plates and culture supernatants of 2.5×10^6 cells were harvested per condition. In a 5% phosphoric acid solution, 100μl of culture supernatant was combined with an equivalent volume of 0.1% naphthylethylenediamine (NEDA) and 1% sulphanalic acid. Absorbance was measured at 550 nm. Known concentrations of sodium nitrite were used for preparation of standard.

Intracellular ATP extraction and determination

Intracellular ATP was extracted using boiling distilled water. Control and NCoR1 KD DCs (0.5×10^6 cells) were seeded in 12 well plates and harvested with and without CpG stimulation. Samples were centrifuged and boiling water was put for 15min and vortexed every 5min. Following which they were incubated in 4°C for 15min and centrifuged again to collect the supernatant for ATP determination. ATP determination was carried out using a specific solution containing recommended proportions of dH$_2$O, reaction buffer, dTT, d-luciferin and luciferase enzyme using an ATP measurement kit (Invitrogen, A22066). The standard curve of ATP was obtained by serial dilutions of 10μM ATP solution. For determining glycolytic ATP, cells were treated with 2-DG (10mM) pre-treatment for 1h. Total intracellular ATP - ATP of 2-DG treated cells gave an approximation of the glycolytic ATP. Luminescence was captured in a multimode reader (PerkinElmer).

Metabolite sample preparation for GC-MS analysis

Control and NCoR1 KD DCs were cultured in 10 cm plates and approximately 10×10^6 cells were harvested per condition. For metabolite extraction, cells were washed twice with 0.9% sodium chloride (NaCl) solution in minimum possible time and chilled methanol (800μl, stored at −20 °C) was added for quenching the metabolic reactions followed by Milli-Q water (800μl) in each well. 10μl of internal standard (2mg/ml Ribitol) was further supplemented in each sample. Following which cells were scraped and collected in 15 ml centrifuge tubes. To each tube, chloroform was added (1.6ml) and vortexed at 4°C for 30min. Cells were centrifuged at 10,000g for 10min at room temperature and the aqueous phase (methanolic) samples were collected and stored at −20 °C until further processing. For GC-MS, 300μl of aqueous samples were taken and dried using speed vac. MS data acquisition of these extracted molecules were carried out using LC-MS as it is or in derivatized form using Methoxamine hydrochloride (MeOX-HCl) (2%) followed by N-methyl-N-(trimethylsilyl)trifluoroacetamide (MSTFA) before running in GC-MS.

Extracellular lactate assay and pH measurement

Extracellular lactate was determined from 30,000 cells/condition from culture supernatants (1:10 dilution) in DC line and 0.1×10^6 (1:5 dilution) cells in BMDCs both for control and NCoR1 depleted DCs. According to manufacturer's recommended protocol (J5021-Promega), supernatant was diluted in 1x PBS before mixing to an equivalent

volume of reaction solution (reductase, reductase substrate, luciferin detection solution, NAD, and lactate dehydrogenase). The standard curve was obtained by serial dilutions of 400μM of lactate solution. Luminescence was captured in a multimode reader (PerkinElmer). Change in pH was also determined from culture media to validate the observed lactate measurements.

Extracellular flux (Seahorse) assay

Control and NCoR1 KD DC line (30,000 cells/well) and BMDCs (0.1 $\times 10^6$ cells/well) were seeded in culture miniplates for the assay. Mito-stress test was performed using serial injections of Oligomycin (2μM), carbonyl cyanide-4-(trifluoromethoxy) phenylhydrazone (CCCP-2μM) and Rotenone+Antimycin A (0.5μM each). The WAVE software was used to calculate respiratory characteristics such as baseline oxygen consumption rate (OCR), Coupled ATP, maximal respiratory capacity, and spare respiratory capacity. Serial doses of Glucose (10mM), Oligomycin (2μM), and 2-DG (50mM) were used in the Glyco-stress test. A pre-injection ECAR experiment was performed to determine the dependency of stimulated control and NCoR1 KD cells on mTOR and HIF-1α using rapamycin (20nM) and KC7F2 (10μM) respectively. ECAR values were determined similar to a mito-stress test using the WAVE software report generator. To establish pyruvate and glutamine dependency, the Mito fuel flex test was used. During pyruvate oxidation measurement, the first injection consisted of UK-5099 (2μM) and the second a combination of etomoxir (4μM) + BPTES (3μM). In a similar way, glutamine oxidation was measured with sequential injections of BPTES (3μM) followed by UK-5099 (2μM) + etomoxir (4μM) together. All the chemicals were prepared according to the manufacturer's protocol (Seahorse bioscience, Agilent technologies). Fatty acid oxidation index was calculated from control and NCoR1 KD CpG samples by sequential injections of etomoxir (50μM) and Oligomycin (2μM).

Oil red - O staining and quantification

Neutral lipid accumulation in control and NCoR1 depleted DCs were visualized by Oil Red O staining. Cells were cultivated on microscope coverslips, placed in 12 well cell culture plates, followed by stimulation with CpG for 6h. After the incubation period, cells were washed with 1x PBS followed by treatment with 1ml of formalin (10%) in 1x PBS for 5min at RT. After that, formalin was discarded, fresh formalin was added and incubated for at least 1h. Before staining, cells were washed thrice with Milli-Q water for the complete removal of formalin and washed once with 60% isopropanol. Then coverslips were dried completely. Staining was performed with 1ml of oil red O staining solution for 10 min followed by intense washing with Milli-Q water. Following which, cells were visualized using ZEISS Apotome microscope. Further the dye was eluted with isopropanol (100%) for 10min and quantified absorbance was noted at 500 nm.

Western blotting

Control and NCoR1 KD whole cell lysates were prepared using RIPA buffer (0.5 M EDTA, 1 M Tris-Cl pH7.5, 1 M NaCl, 200 mM, Roche protease inhibitor) at 6h CpG stimulation. HIF-1α specific cell lysates were treated with 100μM cobalt chloride for 24h before harvesting. After harvesting, samples were processed for sonication in a bioruptor (Diagenode) and protein estimation was done using BCA reagent (Pierce BCA Protein Assay Kit) and absorbance was measured at 562nM. SDS–PAGE was used to separate the cell lysates, which were then transferred to nitrocellulose membranes. Thereafter, membranes were probed with primary antibodies (p-AKT, T-AKT, p-mTOR, T-mTOR, HIF-1α, PDH and G6PD). Next, HRP conjugated secondary antibodies were added to obtain signals by adding ECL solution onto an x-ray film. We probed the membrane with phospho-antibodies first, stripped and re-probed the same membrane with corresponding total antibodies for

western blotting of phospho and its respective total protein. Then we normalized the phosphorylated form with their respective loading controls before performing densitometric analysis. For its comparable total protein, a similar procedure was used. Finally the ratio of normalized values were plotted as relative intensity. Antibodies used for western blotting are listed in the key resource table.

Mtb culture

Middlebrook 7H9 broth (BD Difco, Becton Dickinson) supplemented with 10% ADC (Becton Dickinson), 0.4% Glycerol, and 0.05% Tween-80 was used to grow *Mycobacterium* sp. GFP and mCherry tagged *M. tuberculosis* were used for flow cytometry.

Mtb infection model ex vivo and in vivo

For *ex vivo* experiments, FLT3 differentiated CD11c specific NCoR1 KO BMDCs were either processed for combined inhibition with KC7F2 (10μM) and etomoxir (50μM) for 1h or left untreated. Infection was carried out using mCherry tagged *Mtb* (H37Rv) at a MOI 10 for 2h and 18h. Following which cells were harvested and flow cytometry was performed to check bacterial burden in F4/80$^-$CD11c$^+$CD24$^+$ cells.

For the *in vivo* experiment, 1×10^6 *Mtb*-GFP (H37Rv) in logarithmic phase (OD$_{600}$ = 0.5–0.6) in 20μl 1x PBS were given intranasally into mice anaesthetized with Ketamine-Xylazine. On day 3, 8, 12, and 16 one set of NCoR1 KO mice were injected with KC7F2 (5mg/kg/BW) and etomoxir (10mg/kg/BW) intraperitoneally. After 21 days, *Mtb* burden was determined in lungs by using flow cytometry in the CD11c$^+$CD103$^+$ DCs. Splenic cells were processed for RBC lysis and stained with surface and IC antibodies to determine the CD4$^+$ effectors, Th1 and Treg population (gated on effector cells) upon PMA (10ng/ml), Ionomycin (500ng/ml) and Brefeldin A (2.5μg/ml) treatment for 5h. Antibodies used for flow cytometry are listed in the key resource table.

RNAseq library preparation

DC line samples (Control CpG 6h, Control CpG 6h+KC7F2+etomoxir, NCoR1 KD CpG 6h and NCoR1 KD CpG 6h+KC7F2+etomoxir) were processed for RNA extraction and library preparation. RNA extraction was performed using a kit from Macherey-Nagel. Briefly, samples were lysed with 350 μl of LBP buffer, following which genomic DNA was removed using a nucleospin gDNA removal column. The flow-through was mixed with 100μl of the binding solution, centrifuged at 11,000×*g* for 15s, and washed using wash buffer 1 and 2 before eluting RNA in 20μl of RNAse-free water. For library preparation, magnetic beads and an mRNA isolation kit were used to isolate mRNA from 1μg of total RNA (Poly-A mRNA isolation module, NEB). NEB's mRNA library preparation kit Ultra II was later used to prepare RNAseq libraries according to the manufacturer's instructions. Qubit 2.0 (Invitrogen) was used to determine library concentrations, and Bio-analyzer was used to examine fragment sizes (Agilent).

Nucleic acid sequencing protocol

cDNA samples were denatured using 0.2N NaOH at RT for 5min. Further, 10mM Tris-Cl pH-8.5 was used to neutralize the effect of NaOH. 4nM cDNA libraries were diluted with HT1 buffer for a final loading concentration of 1.6 pM. Following that, the libraries were sequenced on the Illumina NextSeq 550 platform at in-house ILS Sequencing facility.

RNAseq analysis

Paired end raw reads were first checked for quality control using FASTQC and then aligned to mouse reference genome (mm10) using hisat2 [81]. Gene count was then extracted using *feature Counts* function from RSubRead R package [82]. Principal component analysis and

differential gene expression analysis were performed using the DESeq2 package [83].GO term enrichment analysis were performed using cluster Profiler, GO (biological processes) terms downloaded from MSigDb [84].

ChIPseq for NCoR1-NGS library preparation and analysis

NCoR1 ChIPseq data in control Uns and at 6h CpG stimulation has been utilized from our previous study [31] to denote NCoR1 binding peaks at the genomic regions of *Pfkfb3, Pfkp, Hif-1α* and *Ppar-γ*.

Immunofluorescence

NCOR1 expression in mature and tolerogenic human moDCs was determined by immunofluorescence staining. Briefly, human moDCs with and without Dex treatment were cultured on glass coverslips in a 12-well cell culture plate followed by stimulation with pIC for 24h. After the incubation period, cells were fixed in 4% paraformaldehyde for 30min at RT, permeabilized, and blocked for 20min in 0.1% Triton X-100 and 2% goat serum. Following this, fixed cells were washed and incubated overnight with an anti-NCOR1 primary antibody (1:100; CST). After the primary antibody incubation, cells were incubated with a fluorescence-conjugated secondary antibody F(ab') 2-Goat anti-Rabbit IgG (H+L) Cross-Adsorbed Secondary Antibody, Alexa Fluor 594) for 120min and mounted with ProLong™ Gold antifade mountant with DAPI (Invitrogen). Finally the cells were observed under a confocal microscope (Leica). Antibodies used are listed in the resource table.

PBMCs isolation, moDC differentiation and primary CD4 T-Co-culture

Blood samples were drawn from 5 healthy individuals for PBMCs isolation. PBMCs were isolated using density gradient centrifugation (2000 rpm, brakes-0 for 20 min) utilizing lymphoprep. Cells were washed with 1x PBS and magnetic based negative selection of CD14$^+$ monocytes (Stem cell technologies) were done. To differentiate them into moDCs, cells were treated with hu-GMCSF (50ng/ml) and hu-IL-4 (20ng/ml) for a period of 6 days. On the other hand, for acquiring tolerogenic moDCs, they were additionally supplemented with Dex at 1μM concentration. Additional supplementation was done on day 3. On day 6, the inhibitor group received 1h pre-treatment of KC7F2 (10μM) and etomoxir (50μM). Following which, all sample groups were stimulated with pIC at 10μg/ml concentration for 24h. After activation, cells were washed thoroughly and incubated with sorted CD4$^+$T cells from 5 other healthy individuals (mixed) at a ratio of 1:10. Proliferation group received eF670 dye stained CD4$^+$T cells whereas, profiling group received cells as it is. After 72h and 96h post incubation, T cells were analyzed for proliferation and Th1 profiling respectively. Reagents and antibodies used are listed in the key resource table.

Ethics statement

In accordance with the necessary ethical approval, human primary PBMCs were extracted from 5ml of venous blood from 10 adult healthy control donors at the Institute of Life Sciences in Bhubaneswar, Odisha, India, for the *ex vivo* experiment. Table S1 contains the details of the donors in an anonymous form. The entire process complied fully with the Declaration of Helsinki 2013, which sets forth the moral standards for medical research involving human subjects. The participants provided written informed consent prior to the collection of PBMCs for *ex vivo* studies, and all subject data was anonymized.

Statistical analysis

Data are presented as mean values ± SEM, except where stated categorically. Statistical comparisons are drawn using a two-tailed Student's *t*-test. Differences were considered significant if $P \leq 0.05$.

References

[1] L.A.J. O'Neill, E.J. Pearce, Immunometabolism governs dendritic cell and macrophage function, J. Exp. Med. 213 (2016) 15–23, https://doi.org/10.1084/jem.20151570.

[2] S.K. Wculek, S.C. Khouili, E. Priego, I. Heras-Murillo, D. Sancho, Metabolic control of dendritic cell functions: digesting information, Front. Immunol. 10 (2019) 775, https://doi.org/10.3389/fimmu.2019.00775.

[3] E.J. Pearce, B. Everts, Dendritic cell metabolism, Nat. Rev. Immunol. 15 (2015) 18–29, https://doi.org/10.1038/nri3771.

[4] B. Kelly, L.A. O'Neill, Metabolic reprogramming in macrophages and dendritic cells in innate immunity, Cell Res. 25 (2015) 771–784, https://doi.org/10.1038/cr.2015.68.

[5] L.A.J. O'Neill, R.J. Kishton, J. Rathmell, A guide to immunometabolism for immunologists, Nat. Rev. Immunol. 16 (2016) 553–565, https://doi.org/10.1038/nri.2016.70.

[6] D.G. Ryan, L.A.J. O'Neill, Krebs cycle rewired for macrophage and dendritic cell effector functions, FEBS Lett. 591 (2017) 2992–3006, https://doi.org/10.1002/1873-3468.12744.

[7] B. Everts, E. Amiel, S.C.-C. Huang, A.M. Smith, C.-H. Chang, W.Y. Lam, V. Redmann, T.C. Freitas, J. Blagih, G.J.W. van der Windt, M.N. Artyomov, R. G. Jones, E.L. Pearce, E.J. Pearce, TLR-driven early glycolytic reprogramming via the kinases TBK1-IKKε supports the anabolic demands of dendritic cell activation, Nat. Immunol. 15 (2014) 323–332, https://doi.org/10.1038/ni.2833.

[8] J. Jantsch, D. Chakravortty, N. Turza, A.T. Prechtel, B. Buchholz, R.G. Gerlach, M. Volke, J. Gläsner, C. Warnecke, M.S. Wiesener, K.-U. Eckardt, A. Steinkasserer, M. Hensel, C. Willam, Hypoxia and hypoxia-inducible factor-1 alpha modulate lipopolysaccharide-induced dendritic cell activation and function, J. Immunol. Baltim. Md 1950 180 (2008) 4697–4705, https://doi.org/10.4049/jimmunol.180.7.4697.

[9] L. Perrin-Cocon, A. Aublin-Gex, O. Diaz, C. Ramière, F. Peri, P. André, V. Lotteau, Toll-like receptor 4-induced glycolytic burst in human monocyte-derived dendritic cells results from p38-dependent stabilization of HIF-1α and increased hexokinase II expression, J. Immunol. Baltim. Md 1950 201 (2018) 1510–1521, https://doi.org/10.4049/jimmunol.1701522.

[10] H. Guak, S. Al Habyan, E.H. Ma, H. Aldossary, M. Al-Masri, S.Y. Won, T. Ying, E. D. Fixman, R.G. Jones, L.M. McCaffrey, C.M. Krawczyk, Glycolytic metabolism is essential for CCR7 oligomerization and dendritic cell migration, Nat. Commun. 9 (2018) 2463, https://doi.org/10.1038/s41467-018-04804-6.

[11] L. de Lima Thomaz, G. Peron, J. Oliveira, L.C. da Rosa, R. Thomé, L. Verinaud, The impact of metabolic reprogramming on dendritic cell function, Int. Immunopharm. 63 (2018) 84–93, https://doi.org/10.1016/j.intimp.2018.07.031.

[12] T. Köhler, B. Reizis, R.S. Johnson, H. Weighardt, I. Förster, Influence of hypoxia-inducible factor 1α on dendritic cell differentiation and migration, Eur. J. Immunol. 42 (2012) 1226–1236, https://doi.org/10.1002/eji.201142053.

[13] W.J. Sim, P.J. Ahl, J.E. Connolly, Metabolism is central to tolerogenic dendritic cell function, Mediat. Inflamm. (2016) 1–10, https://doi.org/10.1155/2016/2636701, 2016.

[14] M.C. Takenaka, F.J. Quintana, Tolerogenic dendritic cells, Semin. Immunopathol. 39 (2017) 113–120, https://doi.org/10.1007/s00281-016-0587-8.

[15] M.P. Domogalla, P.V. Rostan, V.K. Raker, K. Steinbrink, Tolerance through education: how tolerogenic dendritic cells shape immunity, Front. Immunol. 8 (2017) 1764, https://doi.org/10.3389/fimmu.2017.01764.

[16] C.P. Rodrigues, A.C.F. Ferreira, M.P. Pinho, C.J. de Moraes, P.C. Bergami-Santos, J. A.M. Barbuto, Tolerogenic Ido(+) dendritic cells are induced by PD-1-expressing mast cells, Front. Immunol. 7 (2016) 9, https://doi.org/10.3389/fimmu.2016.00009.

[17] F. Malinarich, K. Duan, R.A. Hamid, A. Bijin, W.X. Lin, M. Poidinger, A.-M. Fairhurst, J.E. Connolly, High mitochondrial respiration and glycolytic capacity represent a metabolic phenotype of human tolerogenic dendritic cells, J. Immunol. 194 (2015) 5174–5186, https://doi.org/10.4049/jimmunol.1303310.

[18] G.B. Ferreira, A.-S. Vanherwegen, G. Eelen, A.C.F. Gutiérrez, L. Van Lommel, K. Marchal, L. Verlinden, A. Verstuyf, T. Nogueira, M. Georgiadou, F. Schuit, D. L. Eizirik, C. Gysemans, P. Carmeliet, L. Overbergh, C. Mathieu, Vitamin D3 induces tolerance in human dendritic cells by activation of intracellular metabolic pathways, Cell Rep. 10 (2015) 711–725, https://doi.org/10.1016/j.celrep.2015.01.013.

[19] L. Piemonti, P. Monti, P. Allavena, M. Sironi, L. Soldini, B.E. Leone, C. Socci, V. Di Carlo, Glucocorticoids affect human dendritic cell differentiation and maturation, J. Immunol. Baltim. Md 1950 162 (1999) 6473–6481.

[20] C.-Q. Xia, R. Peng, F. Beato, M.J. Clare-Salzler, Dexamethasone induces IL-10-producing monocyte-derived dendritic cells with durable immaturity, Scand. J. Immunol. 62 (2005) 45–54, https://doi.org/10.1111/j.1365-3083.2005.01640.x.

[21] M. Bscheider, E.C. Butcher, Vitamin D immunoregulation through dendritic cells, Immunology 148 (2016) 227–236, https://doi.org/10.1111/imm.12610.

[22] L. Adorini, G. Penna, Induction of tolerogenic dendritic cells by vitamin D receptor agonists, Handb. Exp. Pharmacol. (2009) 251–273, https://doi.org/10.1007/978-3-540-71029-5_12.

[23] M. Di Rosa, M. Malaguarnera, F. Nicoletti, L. Malaguarnera, Vitamin D3: a helpful immuno-modulator, Immunology 134 (2011) 123–139, https://doi.org/10.1111/j.1365-2567.2011.03482.x.

[24] A. Mottis, L. Mouchiroud, J. Auwerx, Emerging roles of the corepressors NCoR1 and SMRT in homeostasis, Genes Dev. 27 (2013) 819–835, https://doi.org/10.1101/gad.214023.113.

[25] M.J. Ritter, I. Amano, N. Imai, L. Soares De Oliveira, K.R. Vella, A.N. Hollenberg, Nuclear Receptor CoRepressors, NCOR1 and SMRT, are required for maintaining

systemic metabolic homeostasis, Mol. Metabol. 53 (2021), 101315, https://doi.org/10.1016/j.molmet.2021.101315.

[26] H. Yamamoto, E.G. Williams, L. Mouchiroud, C. Cantó, W. Fan, M. Downes, C. Héligon, G.D. Barish, B. Desvergne, R.M. Evans, K. Schoonjans, J. Auwerx, NCoR1 is a conserved physiological modulator of muscle Mass and oxidative function, Cell 147 (2011) 827–839, https://doi.org/10.1016/j.cell.2011.10.017.

[27] Y.G. Jeon, J.H. Lee, Y. Ji, J.H. Sohn, D. Lee, D.W. Kim, S.G. Yoon, K.C. Shin, J. Park, J.K. Seong, J.-Y. Cho, S.S. Choe, J.B. Kim, RNF20 functions as a transcriptional coactivator for PPARγ by promoting NCoR1 degradation in adipocytes, Diabetes 69 (2020) 20–34, https://doi.org/10.2337/db19-0508.

[28] T.I. Lima, R.R. Valentim, H.N. Araújo, A.G. Oliveira, B.C. Favero, E.S. Menezes, R. Araújo, L.R. Silveira, Role of NCoR1 in mitochondrial function and energy metabolism, Cell Biol. Int. 42 (2018) 734–741, https://doi.org/10.1002/cbin.10973.

[29] T. Saito, A. Kuma, Y. Sugiura, Y. Ichimura, M. Obata, H. Kitamura, S. Okuda, H.-C. Lee, K. Ikeda, Y. Kanegae, I. Saito, J. Auwerx, H. Motohashi, M. Suematsu, T. Soga, T. Yokomizo, S. Waguri, N. Mizushima, M. Komatsu, Autophagy regulates lipid metabolism through selective turnover of NCoR1, Nat. Commun. 10 (2019) 1567, https://doi.org/10.1038/s41467-019-08829-3.

[30] M.A. Geiger, A.T. Guillaumon, F. Paneni, C.M. Matter, S. Stein, Role of the nuclear receptor corepressor 1 (NCOR1) in atherosclerosis and associated immunometabolic diseases, Front. Immunol. 11 (2020), 569358, https://doi.org/10.3389/fimmu.2020.569358.

[31] A. Ahad, M. Stevanin, S. Smita, G.P. Mishra, D. Gupta, S. Waszak, U.A. Sarkar, S. Basak, B. Gupta, H. Acha-Orbea, S.K. Raghav, NCoR1: putting the brakes on the dendritic cell immune tolerance, iScience 19 (2019) 996–1011, https://doi.org/10.1016/j.isci.2019.08.024.

[32] G.P. Mishra, A. Jha, A. Ahad, K. Sen, A. Sen, S. Podder, S. Prusty, V.K. Biswas, B. Gupta, S.K. Raghav, Epigenomics of conventional type-I dendritic cells depicted preferential control of TLR9 versus TLR3 response by NCoR1 through differential IRF3 activation, Cell. Mol. Life Sci. 79 (2022) 429, https://doi.org/10.1007/s00018-022-04424-w.

[33] L.R. Gray, S.C. Tompkins, E.B. Taylor, Regulation of pyruvate metabolism and human disease, Cell. Mol. Life Sci. CMLS. 71 (2014) 2577–2604, https://doi.org/10.1007/s00018-013-1539-2.

[34] Q. Zhuang, H. Cai, Q. Cao, Z. Li, S. Liu, Y. Ming, Tolerogenic dendritic cells: the pearl of immunotherapy in organ transplantation, Front. Immunol. 11 (2020), 552988, https://doi.org/10.3389/fimmu.2020.552988.

[35] G.C. Brown, Nitric oxide and mitochondrial respiration, Biochim. Biophys. Acta 1411 (1999) 351–369, https://doi.org/10.1016/s0005-2728(99)00025-0.

[36] S. Shiva, Mitochondria as metabolizers and targets of nitrite, Nitric Oxide, Biol. Chem. 22 (2010) 64–74, https://doi.org/10.1016/j.niox.2009.09.002.

[37] R. Filograna, M. Mennuni, D. Alsina, N.-G. Larsson, Mitochondrial DNA copy number in human disease: the more the better? FEBS Lett. 595 (2021) 976–1002, https://doi.org/10.1002/1873-3468.14021.

[38] P.M. Quiros, A. Goyal, P. Jha, J. Auwerx, Analysis of mtDNA/nDNA ratio in mice, Curr. Protoc. Mol. Biol. 7 (2017) 47–54, https://doi.org/10.1002/cpmo.21.

[39] S.J. Kim, B. Diamond, Generation and maturation of bone marrow-derived DCs under serum-free conditions, J. Immunol. Methods 323 (2007) 101–108, https://doi.org/10.1016/j.jim.2007.03.005.

[40] K.A. Bode, F. Schmitz, L. Vargas, K. Heeg, A.H. Dalpke, Kinetic of RelA activation controls magnitude of TLR-mediated IL-12p40 induction, J. Immunol. Baltim. Md 1950 182 (2009) 2176–2184, https://doi.org/10.4049/jimmunol.0802560.

[41] S.H. Møller, L. Wang, P.-C. Ho, Metabolic programming in dendritic cells tailors immune responses and homeostasis, Cell, Mol. Immunol. 19 (2022) 370–383, https://doi.org/10.1038/s41423-021-00753-1.

[42] A. Mishra, Metabolic plasticity in dendritic cell responses: implications in allergic asthma, J. Immunol. Res. 2017 (2017), 5134760, https://doi.org/10.1155/2017/5134760.

[43] S.J. Kierans, C.T. Taylor, Regulation of glycolysis by the hypoxia-inducible factor (HIF): implications for cellular physiology, J. Physiol. 599 (2021) 23–37, https://doi.org/10.1113/JP280572.

[44] P.E. Porporato, S. Dhup, R.K. Dadhich, T. Copetti, P. Sonveaux, Anticancer targets in the glycolytic metabolism of tumors: a comprehensive review, Front. Pharmacol. 2 (2011), https://doi.org/10.3389/fphar.2011.00049.

[45] J.J. Lum, T. Bui, M. Gruber, J.D. Gordan, R.J. DeBerardinis, K.L. Covello, M. C. Simon, C.B. Thompson, The transcription factor HIF-1α plays a critical role in the growth factor-dependent regulation of both aerobic and anaerobic glycolysis, Genes Dev. 21 (2007) 1037–1049, https://doi.org/10.1101/gad.1529107.

[46] E.S. Goetzman, E.V. Prochownik, The role for myc in coordinating glycolysis, oxidative phosphorylation, glutaminolysis, and fatty acid metabolism in normal and neoplastic tissues, Front. Endocrinol. 9 (2018) 129, https://doi.org/10.3389/fendo.2018.00129.

[47] R.J.A. Wanders, G. Visser, S. Ferdinandusse, F.M. Vaz, R.H. Houtkooper, Mitochondrial fatty acid oxidation disorders: laboratory diagnosis, pathogenesis, and the complicated route to treatment, J. Lipid Atheroscler. 9 (2020) 313–333, https://doi.org/10.12997/jla.2020.9.3.313.

[48] V. Souza-Mello, Peroxisome proliferator-activated receptors as targets to treat non-alcoholic fatty liver disease, World J. Hepatol. 7 (2015) 1012–1019, https://doi.org/10.4254/wjh.v7.i8.1012.

[49] P. Corrales, A. Vidal-Puig, G. Medina-Gómez, PPARs and metabolic disorders associated with challenged adipose tissue plasticity, Int. J. Mol. Sci. 19 (2018) E2124, https://doi.org/10.3390/ijms19072124.

[50] H.-C. Yang, H. Yu, Y.-C. Liu, T.-L. Chen, A. Stern, S.J. Lo, D.T.-Y. Chiu, IDH-1 deficiency induces growth defects and metabolic alterations in GSPD-1-deficient

Caenorhabditis elegans, J. Mol. Med. Berl. Ger. 97 (2019) 385–396, https://doi.org/10.1007/s00109-018-01740-2.

[51] L. Chen, Z. Zhang, A. Hoshino, H.D. Zheng, M. Morley, Z. Arany, J.D. Rabinowitz, NADPH production by the oxidative pentose phosphate pathway supports folate metabolism, Nat. Metab 1 (2019) 404–415.

[52] S. Lamichane, B. Dahal Lamichane, S.-M. Kwon, Pivotal roles of peroxisome proliferator-activated receptors (PPARs) and their signal cascade for cellular and whole-body energy homeostasis, Int. J. Mol. Sci. 19 (2018) E949, https://doi.org/10.3390/ijms19040949.

[53] F. Zhao, C. Xiao, K.S. Evans, T. Theivanthiran, N. DeVito, A. Holtzhausen, J. Liu, X. Liu, D. Boczkowski, S. Nair, J.W. Locasale, B.A. Hanks, Paracrine wnt5a-β-catenin signaling triggers a metabolic program that drives dendritic cell tolerization, Immunity 48 (2018) 147–160, https://doi.org/10.1016/j.immuni.2017.12.004, e7.

[54] P.-G. Blanchard, W.T. Festuccia, V.P. Houde, P. St-Pierre, S. Brûlé, V. Turcotte, M. Côté, K. Bellmann, A. Marette, Y. Deshaies, Major involvement of mTOR in the PPARγ-induced stimulation of adipose tissue lipid uptake and fat accretion, J. Lipid Res. 53 (2012) 1117–1125, https://doi.org/10.1194/jlr.M021485.

[55] J.E. Jung, H.S. Kim, C.S. Lee, Y.J. Shin, Y.N. Kim, G.H. Kang, T.Y. Kim, Y.S. Juhnn, S.J. Kim, J.W. Park, S.K. Ye, M.H. Chung, STAT3 inhibits the degradation of HIF-1alpha by pVHL-mediated ubiquitination, Exp. Mol. Med. 40 (2008) 479–485, https://doi.org/10.3858/emm.2008.40.5.479.

[56] I. Tošić, D.A. Frank, STAT3 as a mediator of oncogenic cellular metabolism: pathogenic and therapeutic implications, Neoplasia N. Y. N. 23 (2021) 1167–1178, https://doi.org/10.1016/j.neo.2021.10.003.

[57] A. Jha, A. Ahad, G.P. Mishra, K. Sen, S. Smita, A.P. Minz, V.K. Biswas, S.B. Senapati, B. Gupta, H.A. Orbea, S.K. Raghav, NCoR1 and SMRT fine-tune inflammatory versus tolerogenic balance in dendritic cells by differentially regulating STAT3 signaling, Immunology (2021), https://doi.org/10.1101/2021.03.11.434976.

[58] M.P. Etna, M. Severa, V. Licursi, M. Pardini, M. Cruciani, F. Rizzo, E. Giacomini, G. Macchia, O. Palumbo, R. Stallone, M. Carella, M. Livingstone, R. Negri, S. Pellegrini, E.M. Coccia, Genome-wide gene expression analysis of mtb-infected DC highlights the rapamycin-driven modulation of regulatory cytokines via the mTOR/GSK-3β Axis, Front. Immunol. 12 (2021), 649475, https://doi.org/10.3389/fimmu.2021.649475.

[59] S.K. Matta, D. Kumar, Hypoxia and classical activation limits Mycobacterium tuberculosis survival by Akt-dependent glycolytic shift in macrophages, Cell Death Dis. 2 (2016), 16022, https://doi.org/10.1038/cddiscovery.2016.22.

[60] J. Navarro-Barriuso, M.J. Mansilla, M. Naranjo-Gómez, A. Sánchez-Pla, B. Quirant-Sánchez, A. Teniente-Serra, C. Ramo-Tello, E.M. Martínez-Cáceres, Comparative transcriptomic profile of tolerogenic dendritic cells differentiated with vitamin D3, dexamethasone and rapamycin, Sci. Rep. 8 (2018), 14985, https://doi.org/10.1038/s41598-018-33248-7.

[61] S.H. Kim, H.H. Jung, C.K. Lee, Generation, characteristics and clinical trials of ex vivo generated tolerogenic dendritic cells, Yonsei Med. J. 59 (2018) 807–815, https://doi.org/10.3349/ymj.2018.59.7.807.

[62] A. Iwasaki, R. Medzhitov, Toll-like receptor control of the adaptive immune responses, Nat. Immunol. 5 (2004) 987–995, https://doi.org/10.1038/ni1112.

[63] J. Cui, Y. Chen, H.Y. Wang, R.-F. Wang, Mechanisms and pathways of innate immune activation and regulation in health and cancer, Hum. Vaccines Immunother. 10 (2014) 3270–3285, https://doi.org/10.4161/21645515.2014.979640.

[64] E. Marin, L. Bouchet-Delbos, O. Renoult, C. Louvet, V. Nerriere-Daguin, A. J. Managh, A. Even, M. Giraud, T.P. Vu Manh, A. Aguesse, G. Bériou, E. Chiffoleau, B. Alliot-Licht, X. Prieur, M. Croyal, J.A. Hutchinson, N. Obermajer, E.K. Geissler, B. Vanhove, G. Blancho, M. Dalod, R. Josien, C. Pecqueur, M.-C. Cuturi, A. Moreau, Human tolerogenic dendritic cells regulate immune responses through lactate synthesis, Cell Metab. 30 (2019) 1075–1090, https://doi.org/10.1016/j.cmet.2019.11.011, e8.

[65] A.-S. Vanherwegen, G. Eelen, G.B. Ferreira, B. Ghesquière, D.P. Cook, T. Nikolic, B. Roep, P. Carmeliet, S. Telang, C. Mathieu, C. Gysemans, Vitamin D controls the capacity of human dendritic cells to induce functional regulatory T cells by regulation of glucose metabolism, J. Steroid Biochem. Mol. Biol. 187 (2019) 134–145, https://doi.org/10.1016/j.jsbmb.2018.11.011.

[66] B. Everts, E.J. Pearce, Metabolic control of dendritic cell activation and function: recent advances and clinical implications, Front. Immunol. 5 (2014) 203, https://doi.org/10.3389/fimmu.2014.00203.

[67] Q. Zeng, K. Mallilankaraman, H. Schwarz, Increased akt-driven glycolysis is the basis for the higher potency of cd137l-DCs, Front. Immunol. 10 (2019) 868, https://doi.org/10.3389/fimmu.2019.00868.

[68] M. Haidinger, M. Poglitsch, R. Geyeregger, S. Kasturi, M. Zeyda, G.J. Zlabinger, B. Pulendran, W.H. Hörl, M.D. Säemann, T. Weichhart, A versatile role of mammalian target of rapamycin in human dendritic cell function and differentiation, J. Immunol. Baltim. Md 1950 185 (2010) 3919–3931, https://doi.org/10.4049/jimmunol.1000296.

[69] M. Ohtani, T. Hoshii, H. Fujii, S. Koyasu, A. Hirao, S. Matsuda, Cutting edge: mTORC1 in intestinal CD11c+ CD11b+ dendritic cells regulates intestinal homeostasis by promoting IL-10 production, J. Immunol. Baltim. Md 1950 188 (2012) 4736–4740, https://doi.org/10.4049/jimmunol.1200069.

[70] C.W. Tham, T.M.J. Gold, C. Garcia-Batres, K. Tai, A.R. Elford, M.E. Himmel, A.J. Elia, P.S. Ohashi, Hypoxia-inducible factor 1 alpha limits dendritic cell stimulation of CD8 T cell immunity, PLoS One 15 (2020), e0244366, https://doi.org/10.1371/journal.pone.0244366.

[71] A.F. McGettrick, L.A.J. O'Neill, The role of HIF in immunity and inflammation, Cell Metabol. 32 (2020) 524–536, https://doi.org/10.1016/j.cmet.2020.08.002.

[72] A. Pantel, A. Teixeira, E. Haddad, E.G. Wood, R.M. Steinman, M.P. Longhi, Direct type I IFN but not MDA5/TLR3 activation of dendritic cells is required for maturation and metabolic shift to glycolysis after poly IC stimulation, PLoS Biol. 12 (2014), e1001759, https://doi.org/10.1371/journal.pbio.1001759.

[73] I. Martínez-Reyes, N.S. Chandel, Mitochondrial TCA cycle metabolites control physiology and disease, Nat. Commun. 11 (2020) 102, https://doi.org/10.1038/s41467-019-13668-3.

[74] D. Nolfi-Donegan, A. Braganza, S. Shiva, Mitochondrial electron transport chain: oxidative phosphorylation, oxidant production, and methods of measurement, Redox Biol. 37 (2020), 101674, https://doi.org/10.1016/j.redox.2020.101674.

[75] F. Basit, T. Mathan, D. Sancho, I.J.M. de Vries, Human dendritic cell subsets undergo distinct metabolic reprogramming for immune response, Front. Immunol. 9 (2018) 2489, https://doi.org/10.3389/fimmu.2018.02489.

[76] Y.-X. Lu, H.-Q. Ju, Z.-X. Liu, D.-L. Chen, Y. Wang, Q. Zhao, Q.-N. Wu, Z.-L. Zeng, H.-B. Qiu, P.-S. Hu, Z.-Q. Wang, D.-S. Zhang, F. Wang, R.-H. Xu, ME1 regulates NADPH homeostasis to promote gastric cancer growth and metastasis, Cancer Res. 78 (2018) 1972–1985, https://doi.org/10.1158/0008-5472.CAN-17-3155.

[77] C. Liu, J. Cao, S. Lin, Y. Zhao, M. Zhu, Z. Tao, X. Hu, Malic enzyme 1 indicates worse prognosis in breast cancer and promotes metastasis by manipulating reactive oxygen species, OncoTargets Ther. 13 (2020) 8735–8747, https://doi.org/10.2147/OTT.S256970.

[78] C.H. Liu, H. Liu, B. Ge, Innate immunity in tuberculosis: host defense vs pathogen evasion, Cell. Mol. Immunol. 14 (2017) 963–975, https://doi.org/10.1038/cmi.2017.88.

[79] E.M. Llufrio, L. Wang, F.J. Naser, G.J. Patti, Sorting cells alters their redox state and cellular metabolome, Redox Biol. 16 (2018) 381–387, https://doi.org/10.1016/j.redox.2018.03.004.

[80] S.A. Fuertes Marraco, F. Grosjean, A. Duval, M. Rosa, C. Lavanchy, D. Ashok, S. Haller, L.A. Otten, Q.-G. Steiner, P. Descombes, C.A. Luber, F. Meissner, M. Mann, L. Szeles, W. Reith, H. Acha-Orbea, Novel murine dendritic cell lines: a powerful auxiliary tool for dendritic cell research, Front. Immunol. 3 (2012) 331, https://doi.org/10.3389/fimmu.2012.00331.

[81] D. Kim, J.M. Paggi, C. Park, C. Bennett, S.L. Salzberg, Graph-based genome alignment and genotyping with HISAT2 and HISAT-genotype, Nat. Biotechnol. 37 (2019) 907–915, https://doi.org/10.1038/s41587-019-0201-4.

[82] Y. Liao, G.K. Smyth, W. Shi, The R package Rsubread is easier, faster, cheaper and better for alignment and quantification of RNA sequencing reads, Nucleic Acids Res. 47 (2019) e47, https://doi.org/10.1093/nar/gkz114.

[83] M.I. Love, W. Huber, S. Anders, Moderated estimation of fold change and dispersion for RNA-seq data with DESeq2, Genome Biol. 15 (2014) 550, https://doi.org/10.1186/s13059-014-0550-8.

[84] A. Liberzon, C. Birger, H. Thorvaldsdóttir, M. Ghandi, J.P. Mesirov, P. Tamayo, The Molecular Signatures Database (MSigDB) hallmark gene set collection, Cell Syst 1 (2015) 417–425, https://doi.org/10.1016/j.cels.2015.12.004.